MODELS FOR GRAIN MICROSTRUCTURE EVOLUTION
AND GRAIN STATISTICS

BY

JAEKWANG KIM

DISSERTATION

Submitted in partial fulfillment of the requirements
for the degree of Doctor of Philosophy in Theoretical and Applied Mechanics
in the Graduate College of the
University of Illinois Urbana-Champaign, 2023

Urbana, Illinois

Doctoral Committee:

   Assistant Professor Nikhil C. Admal, Chair and Director of Research
   Professor Harley T. Johnson
   Professor Sascha Hilgenfeldt
   Assistant Professor Marie A. Charpagne

Abstract

One of the important aims of grain boundary modeling is to predict the evolution of a large collection of grains under various thermo-mechanical loads to establish the relation between process parameters and the resulting microstructure. In this thesis, we focus on a microstructure phenomenon called grain growth, of which a defining characteristic is the motion of grain boundaries driven by surface tension to decrease the interfacial energy. Pronounced at high temperature, grain growth is responsible for creating final microstructure, and therefore influences macroscopic properties of polycrystalline material. While various scales of models have been developed for grain growth, models that describe a single microstructure are often computationally intensive, resulting in significantly limited size for tractable systems. However, since the dimensions of microstructure space of possible grain configuration are enormously large, a solution to the process-structure relationship problem is necessarily statistical. This motivates us to develop efficient models that describe the microstructure evolution of an ensemble of polycrystals.

In this thesis, we approach grain growth at two scales. First, we focus on developing an efficient mesocale model and associated computational algorithm for its implementation to efficiently track *full-field* microstructure during grain growth. In particular, we improve the Kobayashi–Warren–Carter (KWC) model, a memory efficient dual-phase field grain boundary model. While the grain boundary energy of original KWC model is restricted to Read–Shockley-type, we generalize it to incorporate arbitrary misorientation-dependent grain boundary energies. The generalized KWC model inherits the memory efficiency of the original KWC model. Furthermore, we develop a new computational method that adapts the thresholding method of Merriman–Bence–Osher scheme for the dual-phase field model. The algorithm implements the curvature motion of grain boundaries represented by the generalized KWC model with a computational cost of $\mathcal{O}(N \log N)$, where N is the number of grid points. We use these tools to study the grain microstructure evolution in a two-dimensional face-centered cubic copper polycrystal to characterize grain growth under crystal symmetry-invariant grain boundary energies.

In the second part of the thesis, we investigate grain growth from a statistical level and develop an ultrafast computational infrastructure in predicting microstructure. Restricting our attentions to two-dimensional

isotropic grain growth, we conceive a new stochastic framework that evolves the joint distribution of two coarse grain descriptors, areas and the number of sides (topology) of grains. Under the assumption of spatial homogeneity, we track grain statistics of the entire system using the descriptors of a collection of representative grains, or *rep grains*. The von Neumann–Mullins law, which states the rate of change of grain area as an exclusive function of topology, is used to deterministically evolve the areas of rep grains. However, since grains change their topology as they evolve by interacting with neighbors, we construct a topology transformation model (TTM) that predicts the probability of topology transformation of a grain in terms of its current state and the states of its neighbors. The construction of the TTM relies on a data-driven approach using a fully connected deep neural network. Topology transformations recorded in phase field simulations are used as training data. Combined with the von Neumann–Mullins law, the resulting neural network model is used in a Monte Carlo simulation to evolve grain microstructures in a statistical sense. The stochastic framework is validated against the asymptotic and transient grain statistics predicted by large-scale phase field simulations.

To my family

Acknowledgments

I would like to begin by expressing my greatest appreciation to Prof. Nikhil Chandra Admal for persistently providing invaluable advising during the entire years of my Ph.D. study. This research would have not been possible without the time spent working with Prof. Admal and the long journey has undoubtedly expanded my boundaries of critical thinking and academic research. I also appreciate my committee members, Professor Harley Johnson, Sascha Hilgenfeldt, and Marie Charpagne, who offered guidance and effort to improve this thesis.

The progress and achievements of my research were possible on the grounds from the pioneering works of Dr. Matt Jacobs as well as Prof. Admal. I would like to thank the present and past graduate UIUC colleagues for sharing their invaluable insight and knowledge: Himanshu Joshi, Junyan He, Tusher Ahmed, Mitisha Surana, Dr. Hyungjoo Seo, Dr. Seung Whan Chung and my old friend Dr. Wonsung Lee. Lastly, the cheering supports of wife, Hyejin Go, and my daughter, Goeun Kim, have sustained and encouraged me to complete this work in the last stretch.

Table of contents

Chapter 1

Thesis introduction

Many metals and ceramics are classified as polycrystalline materials, which are aggregates of single crystal grains stacked together along grain boundaries. Each grain has a characteristic crystallographic orientation, size, and shape. The orientation distribution is commonly referred to as texture. The statistics of such grain characteristics constitute the *grain microstructure* of a polycrystal, which significantly influences its bulk properties. An example of a microstructure-property relationship is the Hall–Petch effect [1, 2], which predicts an increase of yield strength of a polycrystalline material as the average grain size decreases.

Macroscopic properties of polycrystalline materials can be remarkably enhanced by transforming their microstructures [3–12]. For instance, Fig. 1.1 illustrates changes in microstructure and bulk properties during annealing of a cold-worked material, a material plastically deformed at a temperature below its recrystallization temperature. When a material is cold worked, a small portion of the mechanical energy is stored in the form of internal elastic energy due to dislocations, which are line defects in the arrangement of atoms. During heat treatment, the material undergoes restoration processes that lower the materials' internal energy. Restoration occurs in three stages: recovery, recrystallization, and grain growth. During recovery, defects annihilate and dislocations agglomerate to form cell walls/subgrains, while the grain boundaries remain unchanged. As the annealing temperature is further increased to approximately one-third the melting temperature, recrystallization ensues, wherein new defect-free grains nucleate from existing subgrains and grow to replace the microstructures entirely. As a result, strength and hardness decrease considerably. The microstructure evolution past recrystallization is called grain growth, wherein the average grain size, and therefore, ductility increases.

Grain boundary engineering is a material design paradigm, which aims to improve the properties of polycrystalline materials by controlling the grain microstructure using thermo-mechanical processes [13]. The design paradigm is guided by the process-microstructure–property (PSP) relationship, shown schematically in Fig. 1.2. Mapping the PSP relationship remains one of the most fundamental problems in materials science. The challenge stems from the enormity of the microstructure space (relative to the process and property spaces), which includes all possible grain configurations [14], resulting in many-to-one mappings from the microstructure space. As a result, a PSP relation is best described using a statistical description of the microstructure in terms of distributions of certain coarse-grain descriptors, such as grain size, orientations, etc. Therefore, to map a PSP relation, it is necessary to analyze a large collection of grains, which adequately represents the chosen microstructure distributions.

Motivated by grain boundary engineering, the goal of this thesis is to develop computationally efficient
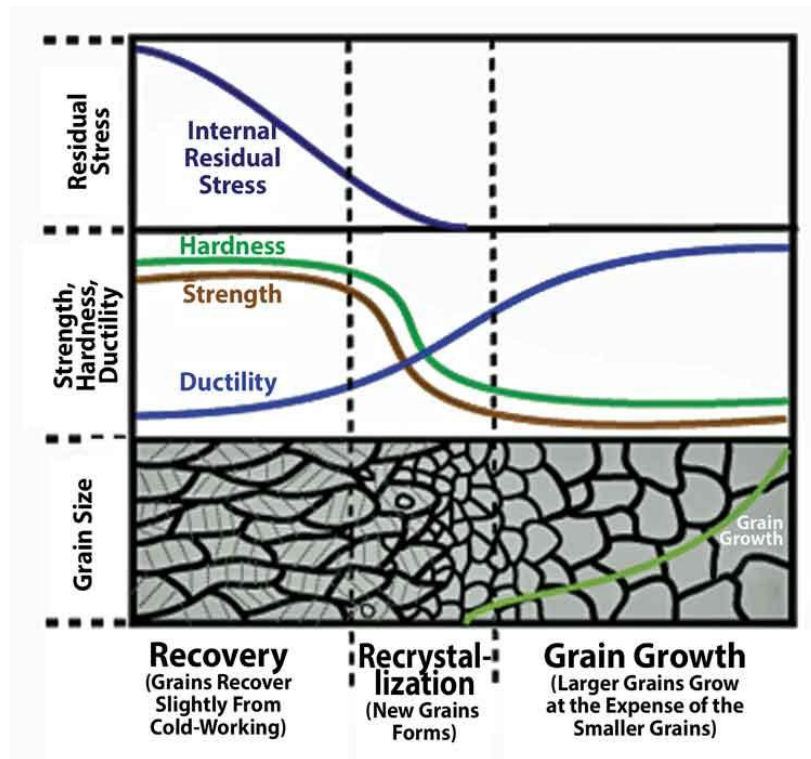
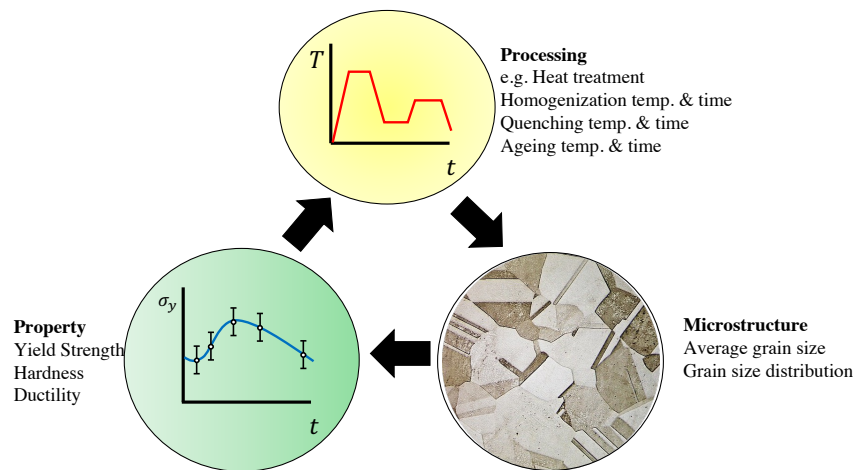Figure 1.1: Changes in bulk properties due to changes in microstructure during annealing of a cold-worked metal. (image credit: `https://www.thefabricator.com`)

Figure 1.2: A schematic of the process–structure–property relationship.

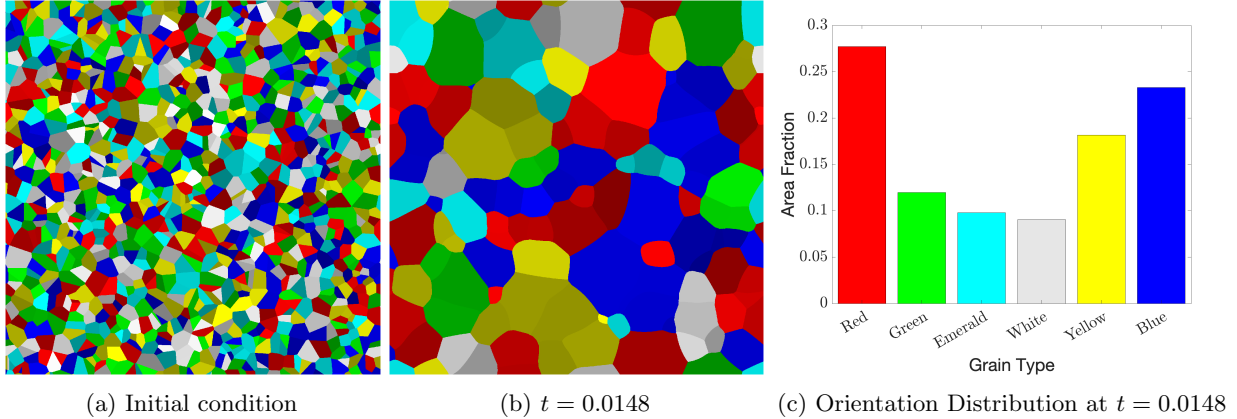| (a) Initial condition | (b) $t = 0.0148$ | (c) Orientation Distribution at $t = 0.0148$ |

Figure 1.3: Grain growth simulation under anisotropic energies using the Gaussian kernel method [15]. The grain boundaries between red and blue grains are twin $\Sigma3$ boundaries. The area fraction of the later stage (b), is dominant by red and blue grains, implying development of a texture (c) from the uniform initial orientation distribution (a).

models for grain microstructure evolution. Although we focus on grain growth, the tools developed here can be used to study recovery and recrystallization stages as well.

A defining characteristic of various grain microstructure models is the motion of grain boundaries driven by surface tension to decrease the interfacial energy. Locally, this effect causes grain boundaries to move towards their centers of curvature as described by the Mullins' model [16] of a grain boundary with isotropic energy and mobility:

$$v = -m\gamma\kappa, \tag{1.1}$$

where v is the velocity of grain boundary and κ is the mean curvature of the grain boundary. Also, m and γ are the grain boundary mobility and energy respectively. The assumption of isotropy in the Mullins model is overly simplistic as the evolution of grain boundaries is treated analogous to that of soap bubbles. Grain boundary evolution, however, is far more complex due to the anisotropy in grain boundary energy and mobility. [1] Here, the anisotropy refers to the dependence on the five macroscopic degrees of freedom (dofs) of a grain boundary — three dofs account for the misorientation between the adjoining grains, and two dofs describe the inclination of the boundary.

The dominant role of anisotropy in grain boundary energy on the evolution is conveyed in Fig. 1.3, which shows the emergence of texture from an initially texture-free microstructure. In particular, twin grains (red and blue grains) dominate in the final microstructure due to the lower energy of twin boundaries. The goal of the first part of this thesis is to develop a computationally efficient framework for simulating fully anisotropy grain boundary evolution in large polycrystals.

The second part of the thesis aims to develop a reduced-order model for microstructure evolution. Unlike the models in the first part, wherein grains are fully resolved, the reduced-order model describes the evolution of distribution of grain descriptors. The motivation stems from our goal of mapping the structure-property relation, which describes macroscopic properties in terms of averaged microstructural features, is enormously large [14].

From the above perspective, this thesis studies grain growth at two scales. The first part of the thesis

---

[1]In addition to this, a coupling grain boundary motion to shear deformation [17, 18] further complicates the analysis of grain boundary evolution. Such shear-coupled grain boundary migration is outside the scope of this thesis.

focuses on developing an efficient mesoscale model and a new computational algorithm to efficiently track *full-field* microstructure evolution during grain growth. Specifically, in Chapter 2 we develop a grain boundary model using atomistically informed grain boundary energies as inputs. The model is a generalization of the dual-phase field KWC model [19–21]. In Chapter 3, we develop an ultrafast algorithm to simulate our grain boundary model. The results of Chapter 2 and Chapter 3 are published in *Computational Materials Science* [22].

The second part of the thesis is introduced in Chapter 4, wherein we develop a lightweight stochastics framework for *grain statistics* during grain growth. The purpose of our framework is to efficiently track the time evolution of statistics of important grain descriptors in a large ensemble of grains. To this end, we construct a coarse-grained framework which relies on a reduced order model for grain topology transformation. The parameters of the grain topology model are inferred from a data-driven approach using the microstructure evolution simulated by the grain boundary model developed in the earlier part. The results of Chapter 4 are also published in the journal *Computational Materials Science* [23]. We summarize this thesis in Chapter 5.

Chapter 2

A crystal symmetry-invariant KWC grain boundary model

The goal of this chapter is to construct an efficient model for curvature motion of grain boundaries in the presence of misorientation-dependent grain boundary energy. To start this chapter, we first begin by reviewing backgrounds on grain boundary energy and models of grain boundary motion in the literature. As implementations of different models often require different numerical techniques, we will also examine available simulation techniques for each grain boundary evolution model as necessary.

2.1 Grain boundary energy

A grain boundary is characterized by five macroscopic degrees of freedom; three degrees represent a rotation associated with the misorientation between the two grains, and the remaining two degrees correspond to the inclination of the grain boundary. More precisely, the grain boundary character space is given by the topological space $\mathcal{T} = SO(3) \times SO(3)/SO(2)$, where $SO(n)$ is the special orthogonal group in n dimensions. Grain boundaries are equipped with a surface energy density, which is defined as a function on $\mathcal{T}$. An energy density that is constant is referred to as an *isotropic*, and *anisotropic* otherwise. Fig. 2.1 shows a plot of grain boundary energy density as a function of misorientation angle for a [110] symmetric-tilt grain boundary in face-centered cubic (fcc) copper, calculated from molecular dynamics simulations [24, 25]. Since the symmetry of an fcc lattice ensures that the energy of a [110] symmetric-tilt grain boundary is symmetric about the 180° misorientation angle, Fig. 2.1 shows a plot of energy vs misorientation angles up to 180°. In addition, as demonstrated in in Fig. 2.1, γ exhibits local minima at certain misorientations, marked as $\Sigma 3$ and $\Sigma 11$ due to an enhanced lattice matching between the two adjoining grains[26–28]. Recent efforts [26, 27, 29–32] by materials scientists in characterizing the grain boundary character space and parametrizing grain boundary energy using data from atomistic simulations and experiments, bring us closer to developing an atomistically-informed mesoscale model for grain boundaries.

In the presence of an anisotropic energy density the resulting grain boundary motion, according to the motion by curvature (1.1), has been shown to have a considerable effect on grain statistics [33], leading to changes in the macroscopic properties of materials. Therefore, in order to explore the structure–property relationship under anisotropic grain boundary energy, we need to develop ultrafast algorithms to simulate grain boundary evolution in polycrystals in the presence of atomistically-informed anisotropic grain boundary
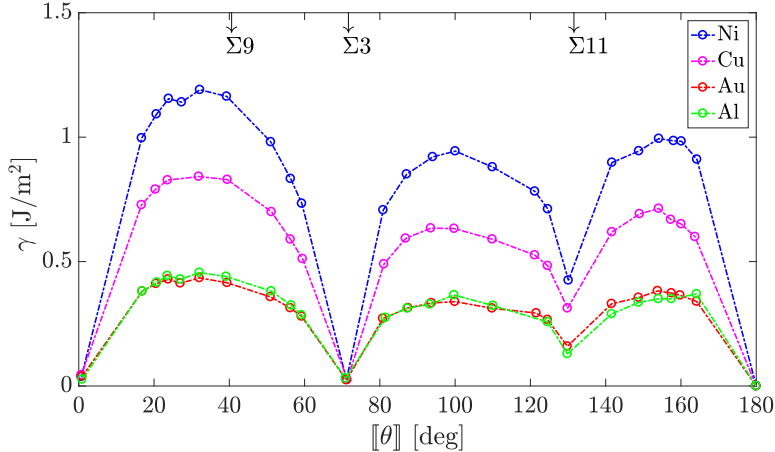
Figure 2.1: A plot of grain boundary energy density as a function of misorientation angle of a [110] symmetric-tilt grain boundary in fcc copper, computed using molecular dynamics [24, 25]. Misorientations corresponding to low energy Σ boundaries are marked on the upper axis.

energies.

2.2   Models of grain boundary motion in the literature

Existing models for grain growth are often classified into three classes: probabilistic, sharp-interface, and diffuse-interface models. An exemplary of a probabilistic model is the Monte-Carlo Potts model [34–38]. In this approach, a polycrystal is described using points in a lattice, which are allocated to different crystallographic orientation angles representing grains. A grain boundary is implicitly identified between adjacent lattice points that belong to different grains. Then, the microstructure is stochastically evolved through random jumps of boundaries in energetically favorable directions. The primary advantage of the Mote-Carlo Potts model lies in the simplicity of its implementation. However, the heuristic rules to move grain boundaries do not have a full thermodynamic basis.

In sharp-interface models [16, 39, 40], grain boundaries are modeled as moving interfaces that explicitly follow the motion by curvature given in (1.1). Several computational techniques can be used to implement (1.1), which rely on tracking the evolving grain boundaries either implicitly or explicitly. Front tracking methods [41–44] discretize grain boundaries in two dimensions using line segments along with their connectivity and move each point according to the local curvature. Unfortunately, such a description fails at critical events including disappearance of shrinking grains and topology changes of grains triggered by converging triple junctions [45]. Consequently, front tracking methods additionally require complicated rules to redefine the connectivity of line segments during critical events.

The above limitations can be effectively addressed in the level set method [46, 47] which employs an implicit representation of interfaces. In this method, each grain is described by a function on the domain that is positive within, and negative outside the grain. Under this setting, the positions of interface surrounding grains are implicitly identified by the zero-valued iso-surface. The implicit representation of surfaces enables to track topology changes of grains without auxiliary rules. Unfortunately, however, the level set method does not extend to handle surfaces with self-intersection and junctions, which often occur during the microstructure

evolutions in polycrystals. More recently, a thresholding method originated from the Merriman–Bence–Osher (MBO) scheme [48] and its generalization (referred to as the Gaussian kernel method [15]) has been shown to simulate grain kinetics very efficiently in terms of computational costs. The level set and the thresholding methods can be memory intensive as they use as many functions as the number of grains in order to describe a polycrystal. For instance, a description of a 3D polycrystal consisting of 10,000 grains on a size of $256\times256\times256$ grid would require ≈ 1 TB of memory. To address memory issue, an additional numerical technique is developed to employ a level set function that co-represent spatially separated multiple grains [49, 50]. While sharp-interface models can easily extend to misorientation dependent grain boundary energy densities and mobilities, incorporating inclination-dependence is not trivial. Recent works by Ref. [51–53] aim to overcome such challenges.

Finally, in diffuse-interface models [54], a polycrystal is defined using functions called phase fields, which are constant in the interior of the grains. The regions where the gradients of phase variables are non-zero are identified as diffused grain boundaries. The motion of grain boundaries are indirectly tracked by the evolution of different phases governed by the principle of maximum dissipation of a free energy functional, resulting in a diffuse interface analog of (1.1). Numerical implementations of a diffuse interface model often rely on classical numerical solvers for partial differential equations such as finite element and finite difference. In general, diffuse-interface models are computationally more expensive than their sharp-interface counterparts, because a numerical grid must be refined enough to resolve the extremely sharp width of interfaces.

The *multi phase field* (MPF) model [55–57], and the Kobayashi–Warren–Carter (KWC) model [19–21] are two examples of diffuse-interface models for grain boundaries. The primary benefit of MPF approach is in the simplicity of its construction to incorporate misorientation dependent grain boundary energies and mobilities. Moreover, recent advances in MPF models [58–60] explore the full anisotropy of grain boundary energy which consists of both misorientation and inclination dependence.[1] Similar to the sharp-interface counterparts (i.e., the level set and the MBO methods), a crude use of the MPF approach would require as many phase field variables as the number grains in the system. However, since only a few order parameter would be on non-zero at any point in domain, this would result in a considerable waste of computational memory. To circumvent the memory issues, recent MPF implementations [61, 62] are equipped with a *grain remapping* algorithm that allow a number of grains which do not share common boundaries to share the same order parameters. When two distant grains grow close to each other, the remapping technique strategically reassigns the order parameters.

On the other hands, the KWC model depicts an arbitrary polycrystal in two-dimension using only two order parameters - one for structural order η ranging from 0 (disordered phase) to 1 (crystalline state), and the other for crystal orientation field θ. The strength of the dual-phase approach is an efficient use of computational memory compared to the multi phase field approach that uses as many order parameter as the number of grains. Unfortunately, the elegance of the KWC model is compromised by the strong restriction it imposes on the grain boundary energy. In particular, the energy functional of the KWC model limits the dependence of grain boundary energy to so-called Read–Shockley-type [63], which is a logarithmic energy as a function of misorientation angle. Such form of energy function is only valid for small angle misorientation grain boundaries, and thus cannot respect the effect of the crystal symmetry demonstrated in Fig. 2.1. In addition, the KWC model form has a singular diffusive nature leading to extremely stiff governing equations that are computationally challenging to solve.

---

[1]Grain boundary energy as a function of inclination is typically non-convex. For grain boundary models that incorporate inclination dependence to be well-posed, they must include curvature-dependent energy densities. This results in a higher-order model which adds to the computationally intensive nature of the MPF model.
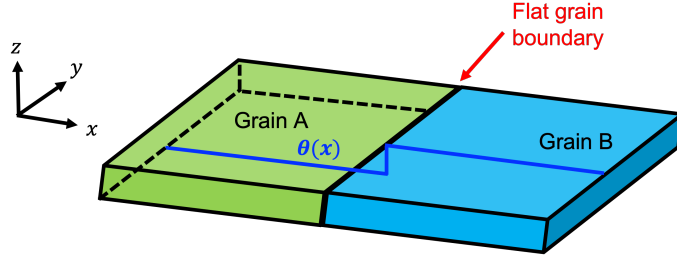
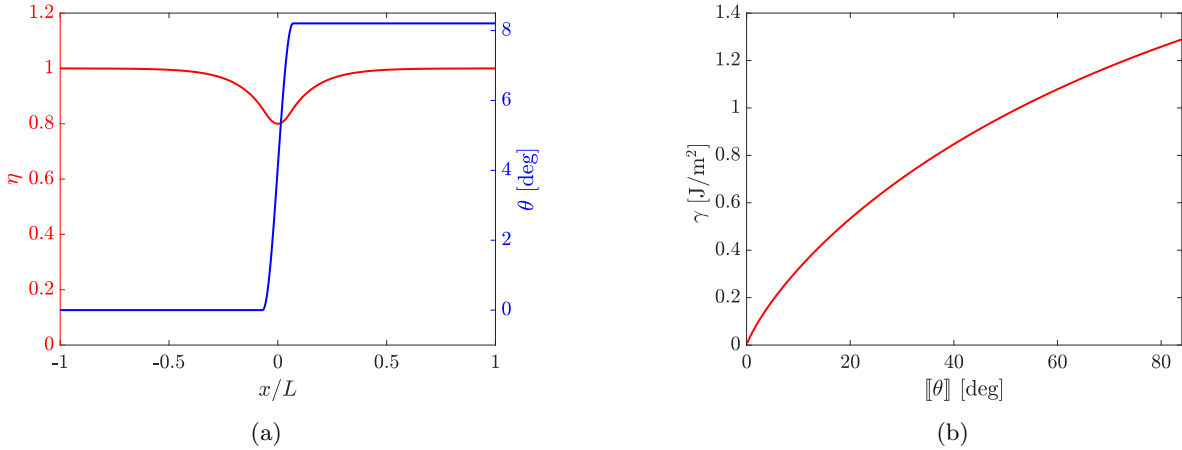Figure 2.2: A schematic of a bicrystal represented by the orientation parameter θ in the KWC model.

(a)

(b)

Figure 2.3: Results on the one-dimensional steady state solution of the original KWC model describing a flat grain boundary. a) A steady state analytical solution of the KWC model for a given misorientation. b) Variation of the grain boundary energy as a function of misorientation in the KWC model.

In this chapter, recognizing the elegance of the phase field model of Kobayashi, Warren and Carter, we will show that the KWC model can be generalized to incorporate arbitrary misorientation-dependent grain boundary energies. The generalized KWC model will inherit the memory efficiency of the original KWC model. In addition to this, we also develop an efficient computational algorithm to evolve grain microstructure described by the new KWC model in the following Chapter 3.

2.3   The Kobayashi–Warren–Carter (KWC) model

In this section, we summarize the important features of the Kobayashi–Warren–Carter (KWC) model [19–21] before formulating its alternate form. The KWC model is a *dual-phase* field model to study grain evolution in two-dimensional polycrystalline materials.[2] The two order parameters of the KWC model are η and θ. The former parameter η ranges from 0, which signifies disorder, to 1 that describes crystalline order. On the other hand, the phase field of θ represents the local orientation of grains.

---

[2]The KWC model can be also generalized for thee dimensions, wherein the order parameter θ is replaced by a rotation tensor. We refer the reader to Ref. [64] for three-dimensional version of the KWC model.

The KWC free energy functional $\mathcal{W}$ of a 2D polycrystal is given by

$$\mathcal{W}[\eta, \theta] = \int_\Omega \left[\frac{f(\eta)}{\epsilon} + \frac{\epsilon}{2}|\nabla\eta|^2 + g(\eta)|\nabla\theta| + \frac{\epsilon}{2}|\nabla\theta|^2 \right] dV, \tag{2.1}$$

where

$$f = \frac{(1-\eta)^2}{2} \tag{2.2}$$

is a single-well potential with minimum at $\eta = 1$, and

$$g = -\ln(1-\eta) \tag{2.3}$$

is an increasing function. The choice of the logarithmic function for $g(\eta)$ (2.3) is supported by the work of Alicandro *et al.* [65], which showed that the KWC functional converges to a surface energy function if $g(1) = \infty$, in the sense of Γ-convergence. [3] The dimensionless scaling parameter ϵ in (2.1) determines the characteristic thickness of the diffused grain boundary region [66]. Note that the functional in (2.1) is defined for all functions η and θ in the Hilbert space $H^1(\Omega)$.[4]

Assuming a gradient descent (with respect to the L^2-norm) of $\mathcal{W}$, the two order parameters are evolved by the following equation,

$$\epsilon b_\eta \dot\eta = \epsilon\Delta\eta - \frac{f'(\eta)}{\epsilon} - g'(\eta)|\nabla\theta|, \tag{2.4a}$$

$$\epsilon b_\theta \dot\theta = \nabla \cdot \left[\epsilon\nabla\theta + g(\eta)\frac{\nabla\theta}{|\nabla\theta|} \right], \tag{2.4b}$$

where b_η and b_θ are the inverse mobilities corresponding to respective order parameters. [5] In Ref. [66], it is shown that the evolution equations (2.4) converge to the kinetics of Mullins model (1.1) in its sharp-interface limit $\epsilon \to 0$, which implies the shrinking of the finite boundary thickness (width of diffused interface).

Below, we brief the role of each term appearing in the KWC functional (2.1) using the one-dimensional steady state solution of (2.4) under Dirichlet boundary conditions

$$\eta(x = \pm\infty) = 1,$$
$$\theta(x = -\infty) = \theta^0 = 0,$$
$$\theta(x = +\infty) = \theta^1.$$

The setting corresponds to the case of a 1D flat bicrystal shown in Fig. 2.2, where the grain boundary is located at the origin $x/L = 0$. The steady-state solution of each parameter demonstrated in Fig. 2.3a describes that the orientation θ is constant in the interior of the grains and has a non-zero gradient in a finite thickness around the grain boundary. The value of $\eta < 1$ in the neighborhood of the grain boundary $x/L \approx 0$ indicates a loss of crystalline order due to the presence of the grain boundary.

The minimum energy state in the 1D bicrystal is obtained by the equilibrium of two opposing mechanisms; while the single well potential f drives $\eta(\boldsymbol{x})$ towards 1, the coupled term $g(\eta)|\nabla\theta|$ tends to decrease η in a neighborhood of the grain boundary. Moreover, the coupled term has a tendency to localize the jump in θ,

---

[3]For more information, we refer the reader to Theorem 4.1 in Ref. [65]

[4]The Hilbert space $H^1(\Omega)$ denotes the set of all functions on Ω whose first derivatives are square integrable.

[5]The KWC model was originally developed to simultaneously model grain rotation *and* grain boundary motion. The model can be specialized to demonstrate *only* curvature grain boundary motion by enforcing zero mobility for θ in the grain interior. This can be achieved by a constant b^ϕ, and a ϕ-dependent b^θ [67].

while $|\nabla\theta|^2$ works towards diffusing it. The consequence is the shape of a regularized step function for θ. Note that in the absence of the $|\nabla\theta^2|$ term, the steady state solution for θ is a pure step function, resulting in a dual-phase model with a blend of sharp- and diffuse-interface characteristics, i.e. while θ is sharp, η is diffused. However, $|\nabla\theta|^2$ in the KWC model has a dual role of not only regularizing θ but also rendering non-zero mobility to the grain boundaries. In other words, in the absence of $|\nabla\theta|^2$ term grain boundaries cease to move [66].

The bicrystal grain boundary energy γ as a function of misorientation angle $[\![\theta]\!] = |\theta^1 - \theta^0|$ predicted by the KWC model can be evaluated by integrating the form (2.1). The results for a range of misorientation angles are plotted in Fig. 2.3b. As stated earlier, $\gamma([\![\theta]\!])$ obtained from the KWC model is of the Read–Shockley-type, as opposed to the grain boundary energies obtained from molecular dynamic simulations shown in Fig. 2.1. Despite the strength of the KWC model in describing polycrystals with only two order parameters, such rigid energy form poses a critical restriction to the KWC model, compared to the versatility of the multiphase field model for accommodating arbitrary grain boundary energy functions. Such limitation is one of the main motivations for this chapter to seek a new formulation of the KWC model to incorporate arbitrary misorientation-dependent grain boundary energies.

2.4 A crystal symmetry-invariant KWC model

In this section, now we seek a new KWC model that can incorporate arbitrary misorientation-dependent grain boundary energies.

We begin with eliminating the $|\nabla\theta|^2$ term in the KWC functional, as the term poses the strongest restriction on grain boundary energy. As previously illustrated in Section 2.3, in the absence of the $|\nabla\theta|^2$ term, the steady state solution for θ take a form of a step function with the discontinuity occurring at the grain boundary. In one-dimension, since a discontinuous θ is not in $H^1(\Omega)$, the minimizer of $\mathcal{W}$, with $|\nabla\theta|^2$ absent, is not attained. This lead us to redefine the domain of the modified KWC functional such that θ belongs to the space of *piecewise constant functions* instead of $H^1(\Omega)$. Under this setting, we now simplify the free energy functional as

$$\mathcal{W}[\eta, \theta] = \int_\Omega \left[\frac{(1-\eta)^2}{2\epsilon} + \frac{\epsilon}{2}|\nabla\eta|^2 \right] dV - \int_\mathcal{S} \ln\left(1 - \bar{\eta}\right) [\![\theta]\!] \, dS, \tag{2.5}$$

where $\bar{\eta} : \mathcal{S} \to \mathbb{R}$ is the restriction of η to the θ-jump set $\mathcal{S}$ represents the union of all grain boundaries. Now, let us re-examine the steady-state solution of the new energy functional (2.5) at a one-dimensional bicrystal. The detailed analytic approach for the solution is provided in A, where the resulting grain boundary energy as a function of $[\![\theta]\!]$ is now derived as

$$\gamma([\![\theta]\!]) = \frac{[\![\theta]\!]}{2} \left(1 - 2\ln\left[\frac{[\![\theta]\!]}{2} \right] \right). \tag{2.6}$$

From (2.6), it is clear that the grain boundary energy is still of a Read–Shockley-type.

However, from the above observation, we suggest the following generalization of the KWC functional

$$\mathcal{W}^\mathrm{G}[\eta, \theta] = \int_\Omega \left[\frac{(1-\eta)^2}{2\epsilon} + \frac{\epsilon}{2}|\nabla\eta|^2 \right] dV + \int_\mathcal{S} g(\bar{\eta})\mathcal{J}\left([\![\theta]\!]\right) dS, \tag{2.7}$$

which is defined for all $\eta \in H^1(\Omega)$, and piecewise constant functions θ. $\mathcal{J}$ which replaces $[\![\theta]\!]$ in (2.5) is an
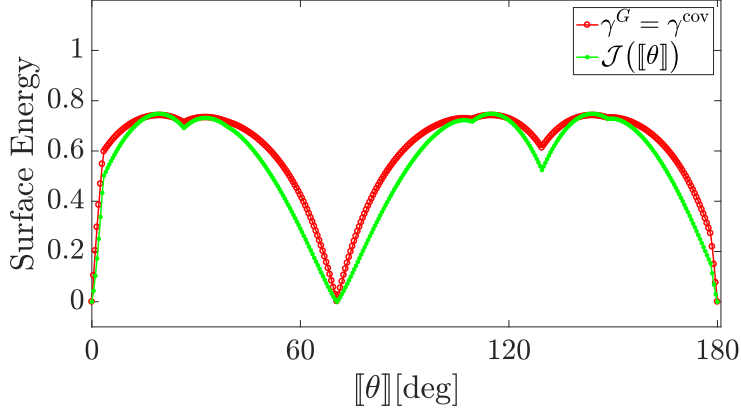
Figure 2.4: A plot (in green) of the core energy $\mathcal{J}(\llbracket \theta \rrbracket)$ calculated to match γ^G (2.8) to γ^{cov} (B.9) (in red) for [110] symmetric-tilt grain boundaries in fcc copper. Note that γ^G is identical to γ^{cov} by construction.

undetermined even function of $\llbracket \theta \rrbracket$. Under this new formulation, the grain boundary energy function (2.6) modifies as

$$
\begin{aligned}
\gamma^{\mathrm{G}}(\llbracket \theta \rrbracket) &= (1 - \overline{\eta})^2 - \ln(1 - \overline{\eta})\mathcal{J}(\llbracket \theta \rrbracket) \\
&= \frac{\mathcal{J}(\llbracket \theta \rrbracket)}{2}\left(1 - 2\ln\left[\frac{\mathcal{J}(\llbracket \theta \rrbracket)}{2}\right]\right),
\end{aligned}
\tag{2.8}
$$

where $\overline{\eta}$ is the value of the stead-state solution on the grain boundary, given implicitly in terms of $\mathcal{J}(\llbracket \theta \rrbracket)$ as [6]

$$
2(1 - \overline{\eta})^2 = \mathcal{J}(\llbracket \theta \rrbracket).
\tag{2.9}
$$

Motivated from the related terminology in the dislocation theory, we name $\mathcal{J}(\llbracket \theta \rrbracket)$ as the *core energy*.

Then, the flexibility of the grain boundary energy function in the new KWC model is enabled by the form (2.8), with an appropriately designed core energy function $\mathcal{J}$ that faithfully represents the grain boundary energy and symmetry of the bicrystal. In other words, the crystal symmetry of the new KWC model is inherited from the core energy function. For demonstration, consider the energy γ^{cov} of a [110] symmetric tilt grain boundary in face-centered cubic (fcc) copper, illustrated as red points in Fig. 2.4. Here, γ^{cov} is computed using the *lattice-matching method* developed in Ref. [26, 27]. To define the grain boundary energy, the method uses the measure of the agreements (the covariance) of two lattices adjoining the grain boundary. [7] Using a simple iterative method (e.g.,the Newton's method) we can solve for for $\mathcal{J}$ in (2.8) such that the grain boundary energy γ^{G} of the new KWC is identical to γ^{cov}. The green points in Fig. 2.4 shows a plot of the solution $\mathcal{J}$, that highlights the common positions of the local minimizers of $\mathcal{J}$ and γ^{cov}.

While the alternate KWC functional (2.7) enables us to incorporate arbitrary misorientation-dependent grain boundary energies, the absence of $|\nabla\theta|^2$ term in the free energy (2.7) yields immobile grain boundaries as suggested in Section 2.3 [8]. In the following chapter, we address this drawback by developing a thresholding method to move grain boundaries using the piecewise-constant θ.

---

[6]The analog of (2.9) in the original KWC model is shown in (A.7), of which the derivation is also provided in Appendix A.
[7]For completeness of the thesis we provide the details on lattice-matching method in Appendix B along with the list of the parameters to arrive at the data plotted in Fig. 2.4.
[8]The gradient descent of $\mathcal{W}^{\mathrm{G}}$ drives a pure rotational evolution of θ, while the position of the grain boundaries remains fixed.

Chapter 3

A thresholding method for gain boundary motion in the new KWC model

The goal of this chapter is to introduce a new approach to evolve a polycrystal governed by the generalized KWC model $\mathcal{W}^{\mathrm{G}}$ (2.7). The key idea of our algorithm is to alternate between evolving η and θ using two separate numerical methods; each method is suitably designed for each sub-problem, the evolution equation for each order parameter.

First, for a given piecewise-constant θ, the order parameter η can be solved in the following minimization problem

$$\eta^* = \underset{\substack{\eta \in H^1(\Omega) \\ \partial\eta/\partial n|_{\partial\Omega}=0}}{\arg\min} \quad \mathcal{W}^{\mathrm{G}}[\eta, \theta]. \tag{3.1}$$

In numerical approaches for (3.1), we note that the Newton's method is not viable. This is because $g(\eta) \to \infty$ as $\eta \to 1$, leading to the non-smooth functional W^{G} with respect to η. Therefore, we employ a primal-dual method developed by Jacobs *et al.* [68]. The method has a $\mathcal{O}(\frac{1}{e}N \log N)$ complexity, where e is the error in the numerical solution to (3.1), and N is the grid size. See C for a more detailed description of the primal-dual method.

Instead, the primary focus of the present chapter is to develop a thresholding rule that algorithmically drives curvature motion of θ for a fixed η^* acquired from (3.1). The alternate use of the primal-dual method and the thresholding rule at every time step constitutes our new approach to evolving the grain boundaries of W^{G}.

3.1 The thresholding rule

A thresholding method is a computational algorithm consisting of a series of simple rules, executed every time step to reinitialize the order parameter, which describes the curvature motion of interfaces.

The original idea of a thresholding method to evolve grain boundaries was first explored in the work of Merriman, Bence and Osher (MBO) [48]. In their method, grains in a polycrystal are described using as many characteristic functions, similar to the order parameters of multiphase field model. Each characteristic
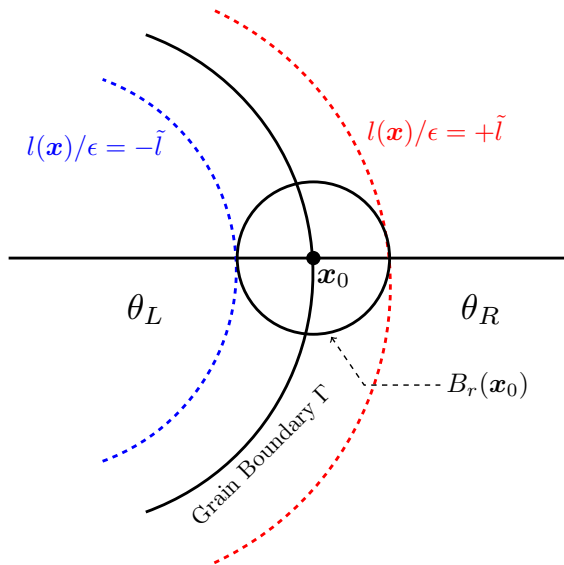
Figure 3.1: Level sets of the distance function $l(\boldsymbol{x})$ in a neighborhood of $\boldsymbol{x}_0$. The grain boundary Γ is depicted as a solid curve, and the dashed curves correspond to the level sets $l(x)/\epsilon = \pm\tilde{l}$.

function is piecewise-constant which takes the value of 1 in the interior of the corresponding grain and 0 otherwise, resulting in a sharp-interface representation of grain boundaries. Then, the curvature motions of interfaces are algorithmically generated using a two-step rule, a convolution of the characteristic functions with a Gaussian kernel followed by a trivial thresholding. The MBO method has recently been generalized to a variational model, referred to as the *Gaussian kernel method* [15].

While the end goal of the KWC model is also to describe motion by curvature, our thresholding method is significantly different from these earlier works [15, 48], as it uses only two order parameters to represent a polycrystal. Consequently, it does not require additional techniques to address the memory intensive nature of a crude implementation of the MBO/Gaussian kernel methods. More essentially, the KWC model is adaptable to further generalizations which include the modeling of grain rotation. Therefore, the goal here is to seek a thresholding algorithm to implement the KWC model.

We first recognize that θ is a piecewise-constant field with a finite range of orientations. Thus, a thresholding rule should reassign $\theta(\boldsymbol{x})$, for each point $\boldsymbol{x} \in \Omega$, to one of the possible orientations. We will design a thresholding rule from the observation that *the asymmetry of η in the neighborhood of a grain boundary characterizes its curvature.* In the following, we explicitly identify this asymmetry before describing our thresholding rule.

To begin with, recall that the steady-state solution for η for a flat interface (i.e., zero curvature), derived in (A.8) and shown in Fig. 2.3a, is symmetric about the grain boundary. Now, we derive an approximate form for η in the presence of a non-zero curvature, and relate the η-asymmetry to the grain boundary curvature. Let Γ be a grain boundary with a non-zero curvature that separates two grains with orientations θ_L and θ_R as shown in Fig. 3.1. Assuming that Γ has a small curvature such that $\epsilon\kappa \ll 1$, for a $\boldsymbol{x}_0 \in \Gamma$ away from a triple junction, the solution η^* to (2.4a) is approximated using the signed distance function from Γ to $\boldsymbol{x}$

$$\eta^*(\boldsymbol{x}) \approx u\left(\frac{l(\boldsymbol{x})}{\epsilon}\right), \tag{3.2}$$

13

in a small neighborhood of $\boldsymbol{x}_0$. In other words, we assume that η only depends on the radial coordinate.

Away from the grain boundary where $|\nabla\theta| = 0$, the solution to the minimization problem in (3.1) satisfies the equation

$$\epsilon\Delta\eta^* - \frac{(\eta^* - 1)}{\epsilon} = 0. \tag{3.3}$$

To simplify (3.3) we employ a local coordinate system $\boldsymbol{x} = (\tilde{l}, s)$,where $\tilde{l} = l(\boldsymbol{x})/\epsilon$ is the scaled radial coordinate, and s is the distance measured along Γ between $\boldsymbol{x}_0$ and the perpendicular projection of $\boldsymbol{x}$ on Γ. In this coordinate system, the Laplacian is written as $\Delta\eta(\boldsymbol{x}) = u''/\epsilon^2 + \kappa u'/\epsilon$, where $\kappa(\tilde{l})$ is the curvature of the coordinate line $\{\boldsymbol{x} \in B_r(\boldsymbol{x}_0) : l(\boldsymbol{x}) = \tilde{l}\epsilon\}$. This allows us to reduce the equation (3.3) to an ordinary differential equation

$$u''(\tilde{l}) + \epsilon\kappa u'(\tilde{l}) - u(\tilde{l}) + 1 = 0. \tag{3.4}$$

Assuming $\kappa(\tilde{l}) = \kappa(0)$, a general solution to (3.4) is obtained in the following closed-form:

$$u(\tilde{l}) = 1 + C_1 \exp\left[-\tilde{l}\left(\frac{\epsilon\kappa + \sqrt{4 + \epsilon^2\kappa^2}}{2}\right)\right] + C_2 \exp\left[-\tilde{l}\left(\frac{\epsilon\kappa - \sqrt{4 + \epsilon^2\kappa^2}}{2}\right)\right], \tag{3.5}$$

where the constants C_1 and C_2 need to be determined using the boundary conditions $u(\pm\infty) = 1$.[1]

Assuming both ϵ and $\epsilon\kappa$ are small, the solution can be further approximated, resulting in [2]

$$u(\tilde{l}) = \begin{cases} 1 + (u(0) - 1)e^{-(1+0.5\epsilon\kappa)\tilde{l}} & \text{if } \tilde{l} > 0, \\ 1 + (u(0) - 1)e^{(1-0.5\epsilon\kappa)\tilde{l}} & \text{otherwise.} \end{cases} \tag{3.6}$$

The form (3.6) explicitly shows the asymmetry of u around $\tilde{l} = 0$. For instance, in the presence of a positive curvature, the rate at which u converges to 1 when $\tilde{l} \to +\infty$ is faster than $\tilde{l} \to -\infty$.

The asymmetry of u provides the ground of our thresholding scheme which reassigns the values of θ in the neighborhood of the grain boundaries resulting in a motion by curvature. To develop such rule, we recognize a unique $l = l_0$, which is the solution of the following integral equation

$$\int_{-\infty}^{l_0} (1 - u(l/\epsilon))^2 \, dl = \int_{l_0}^{+\infty} (1 - u(l/\epsilon))^2 \, dl. \tag{3.7}$$

In Fig. 3.2, we provide a graphical interpretation of the above integral equation, which is to identify the location of l_0 such that the two separated areas underneath the $(1 - u)^2$-curve become the same (marked with the yellow and green regions respectively). Clearly, the solution to (3.7) is not $l_0 = 0$ because of the asymmetry of u, induced from a non-zero curvature. A straightforward but tedious calculation shows that

$$l_0 = -\frac{\epsilon^2}{4}\kappa + \mathcal{O}(\epsilon^3). \tag{3.8}$$

See D for details to arrive at (3.8) from (3.7). If we reinitialize the orientations of all $\boldsymbol{x}$ with $l(\boldsymbol{x}) < l_0$ to θ_{L}, and to θ_{R} when $l(\boldsymbol{x}) > l_0$, such thresholding rule drives the curvature motion of the grain boundary by $dt = \mathsf{t}\epsilon^2/4$, where $\mathsf{t} = 1$ is a unit conversion factor. Alternating between the η-update using the primal-dual method, and the θ-update using the thresholding rule, results in a grain boundary motion by curvature with

---

[1]The boundary conditions are interpreted in the limit $\epsilon \to 0$, which results in the boundary conditions $l/\epsilon = \pm\infty$ for the scaled radial coordinate .

[2]Here, we use the approximation $\sqrt{4 + \epsilon^2\kappa^2} \approx 2 + \mathcal{O}(\epsilon^2\kappa^2)$.
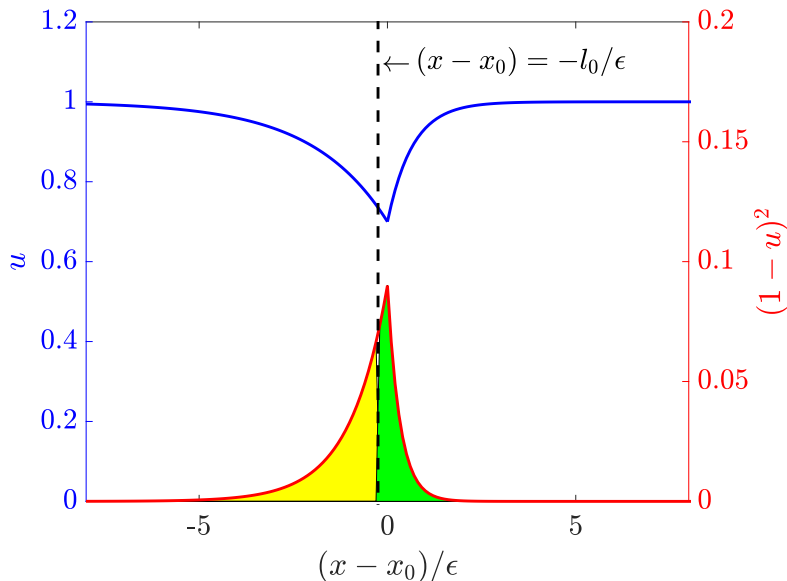
Figure 3.2: A plot of $\eta^*(=u)$ in a small neighborhood of x_0 (see Fig. 3.1) is shown in blue, while $(1-\eta^*)^2$ is shown in red. The asymmetry of u around x_0 due to curvature κ is characterized by the position x at which the two areas shown in yellow and green regions are equal. The position x is given in terms of l_0, $(x-x_0)=l_0/\epsilon$, which is the solution of (3.7).

mobility equal to the inverse of the grain boundary energy.[3] Although this causes a strong restriction on the grain boundary mobility, we postulate that this can be potentailly overcome by modifying the thresholding rule (3.7), and this will be addressed in a future work. Clearly, the efficiency of the thresholding rule described above rests on the effective computation of l_0 in (3.7). In the next section, we introduce the *fast marching method* to not only compute l_0 in an $\mathcal{O}(N \log N)$ algorithm, but also generalize the above strategy to an arbitrary polycrystal.

3.2 Thresholding dynamics via the fast marching method

The fast marching method (FMM), first introduced by Tsitsiklis [71], is an algorithm to evolve a surface with a spatially varying normal velocity. A general description of FMM is provided in Appendix E with a stand-alone example. Here, we focus on how we utilize the fast marching method to implement the thresholding algorithm described in Section 3.1.

We begin with a demonstration of our implementation of the thresholding scheme for a bicrystal consisting of a circular grain, followed by its generalization to a polycrystal. First, recall that the boundary conditions $u(\pm\infty) = 1$ used to arrive at (3.6) and (3.7) apply only in the limit $\epsilon \to 0$ as noted in footnote 1. In practice, we truncate with a finite limit $l_{\mathrm{b}} > 0$, and modify (3.7) as

$$\text{Find } l_0 \text{ such that } \int_{-l_{\mathrm{b}}}^{l_0} (1 - u(l/\epsilon))^2 \, dl = \int_{l_0}^{l_{\mathrm{b}}} (1 - u(l/\epsilon))^2 \, dl. \tag{3.9}$$

---

[3]In this case, the *reduced mobility* [69, 70], which is defined as the product of grain boundary energy and mobility, is equal to 1 for all grain boundaries.
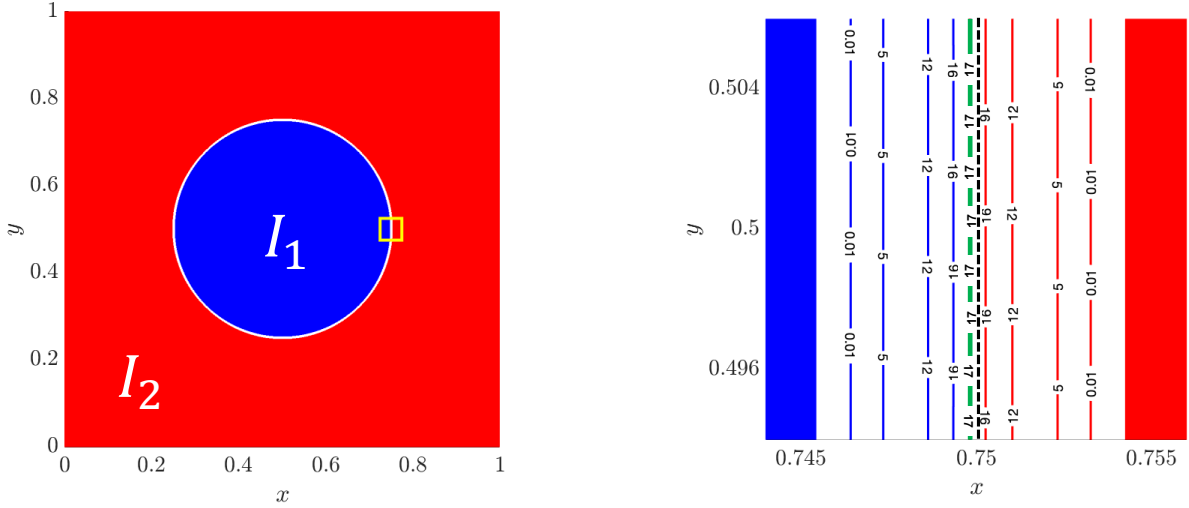
(a) Two interior regions of a bicrystal with a circular grain boundary

(b) The two initial surfaces ∂I_1 and ∂I_2 evolved using the FMM.

Figure 3.3: Shrinking of a circular grain simulated using the thresholding method. a) Two interior regions (red and blue) I_1 and I_2 are grown towards the grain boundary with a speed $1/(1-\eta^*)^2$ using the fast marching method. b) A closeup of a rectangular region around the grain boundary, depicted in (a), shows the contour lines of the fast marching method, which describe the time it takes for ∂I_1 or ∂I_2 to arrive at a grid point. Therefore, the original grain boundary, shown as a dashed black line in (b), moves to a new position (solid green line) where the two grain interiors meet.

In Appendix D, we show that the error in l_0 due to the introduction of l_b exponentially decreases as $\epsilon \to 0$.

In order to use FMM in computations of l_0, we interpret the integrand $(1-u(l/\epsilon))^2$ in (3.9) as an inverse of the normal velocity of a surface $\mathcal{S}_l := \{\boldsymbol{x} : l(\boldsymbol{x}) = l\}$ evolving towards the grain boundary. In this perspective, the integrals in (3.9) are a measure of the time it takes for two initial surfaces $\mathcal{S}_{-l_b}$ and $\mathcal{S}_{l_b}$ on either side of the grain boundary, to meet at $l = l_0$. In other words, l_0 is where the two evolving interface arrive at the same time. Now, we will use the fast marching method to co-evolve the surfaces $\mathcal{S}_{-l_b}$ and $\mathcal{S}_{l_b}$, and implement the thresholding rule (described in Section 3.1) by reassigning the orientation of any point $\boldsymbol{x}$ in the region $\{\boldsymbol{x} \in \Omega : |l(\boldsymbol{x})| < l_b\}$ to θ_L if it first encounters the evolving surface $\mathcal{S}_{-l_b}$, and to θ_R otherwise.

In practice, however, we do not know the signed distance function $l(\boldsymbol{x})$ to identify the surfaces $\mathcal{S}_{-l_b}$ and $\mathcal{S}_{l_b}$. Instead, we first identify the grain interiors I_p defined as

$$I_p = \{\boldsymbol{x} \in \Omega : \theta(\boldsymbol{x}) = \theta_p, \ \eta(\boldsymbol{x}) > 1 - \xi\}, \tag{3.10}$$

where $\xi > 0$ is some fixed small value. We will examine errors resulting from the introduction of ξ in the following as well. Fig. 3.3a shows the grain interiors I_1 and I_2 in a bicrystal, and Fig. 3.3b is a closeup of a rectangular region, marked in yellow, around the grain boundary. The original grain boundary is marked as a black dashed line in Fig. 3.3b. By construction, the two surfaces ∂I_1 and ∂I_2 are equidistant, up to $\mathcal{O}(\epsilon)$, from the grain boundary, and serve as substitutes for $\mathcal{S}_{-l_b}$ and $\mathcal{S}_{l_b}$. The grain interiors are grown in the outward direction with a velocity $(1-u(l/\epsilon))^{-2}$ using the fast marching method, and the surface where they meet is the new grain boundary, shown as a green dashed line in Fig. 3.3b.

Next, we generalize the above strategy to an arbitrary polycrystal consisting of $\mathcal{N}$ grains. Each grain
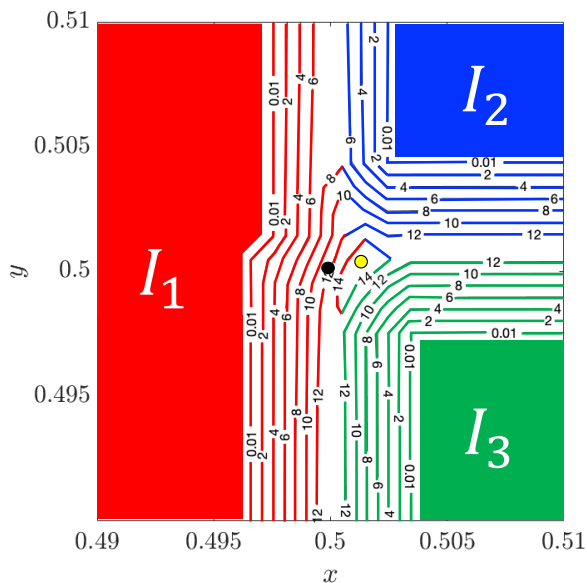
16

Figure 3.4: Movement of a triple junction according to the thresholding algorithm. The triple junction initially at $(x, y) = (0.5, 0.5)$ (black filled circle) moves to a new position (yellow filled circle) where the three grain interiors, evolved using the fast marching method, meet at the same time.

is described using a piecewise constant function $\theta(\mathbf{x})$ with values in $\{\theta_1, \ldots, \theta_N\}$. Once the corresponding η^*-solution is obtained using the primal dual algorithm, we identify the N grain interiors using (3.10), and define I as their union. Then, we grow the grain interiors in their outward unit normal directions until every point (in the almost everywhere sense) in the domain is reassigned to one of values in $\{\theta_1, \ldots, \theta_N\}$. We implement this by first collecting all the boundaries of the interior regions in $\partial I = \partial I_1 \cup \cdots \cup \partial I_n$, and *simultaneously* evolving them in the outward normal direction with a speed of $1/(1 - \eta^*(x))^2$ using the fast marching method. Note that the fast marching method is used to evolve *all* grain interiors in union as opposed to evolving them individually. As the grain interiors grow, a point $\boldsymbol{x} \in \Omega - I$ is reinitialized to an orientation θ_q if it encounters $\partial I_q \subset \partial I$. At the end of the fast marching method, all points in $\Omega - I$ have been reinitialized resulting in an updated polycrystal, and this completes the one time step. Fig. 3.4 shows the implementation of the thresholding rule in a tricrystal. In particular, Fig. 3.4 demonstrates the movement of a triple junction according to our algorithm. The new position of the triple junction is where the three growing grain interiors meet at the same time.

Two types of boundary condition are available in the our scheme. First, the Dirichlet boundary conditions on θ can be imposed by including all $\boldsymbol{x} \in \partial\Omega$ in the grain interiors. On the other hand, periodic boundary conditions are achieved by periodically reinitializing θ for $\boldsymbol{x} \in \partial\Omega$ during the fast marching step.

The primal-dual and the fast marching methods are carried out on a regular grid of resolution with a discretized finite length, say δx. From (3.8), we know that the grid should be refined enough to resolve a grain boundary movement of $\epsilon^2 \kappa$ in each time step, i.e.

$$\delta x \ll \epsilon^2 \kappa, \tag{3.11}$$

which is a common grid restriction of other thresholding methods [15, 48]. If this condition is not satisfied,

---

Algorithm 1 Thresholding algorithm for the new KWC model

1: Input: a) A polycrystal with $\mathcal{N}$ grains with orientations $\theta_1, \ldots, \theta_{\mathcal{N}}$
     b) grain boundary core energies $\mathcal{J}(\llbracket \theta \rrbracket)$; c) parameters: ϵ, ξ, total time T, and tolerance e.
2: Construct the core energy function $\mathcal{J}(\llbracket \theta \rrbracket)$ from grain boundary energy data
3: Initialize $t = 0$, and the orientation field $\theta(\boldsymbol{x}, 0)$
4: **while** $(t \leq T)$ **do**
5:      Compute the discrete jump fields $\llbracket \theta \rrbracket(\boldsymbol{x}, t)$ and $\bar{\mathcal{J}} := \mathcal{J}(\llbracket \theta \rrbracket(\boldsymbol{x}, t))$ on Ω
6:      Regularize the jump field: $\mathcal{J}^\star = G * \bar{\mathcal{J}}$, where $G(\boldsymbol{x}) = (1/2\pi\epsilon^2)e^{-\frac{|\boldsymbol{x}|^2}{2\epsilon^4}}$
       ** *Solve for* $\eta(\boldsymbol{x}, t)$ *using the primal-dual algorithm* **
7:      Initialize η and the dual field ψ: $\eta_0(\boldsymbol{x}) = 0$, $\psi_0(\boldsymbol{x}) = 0$, and $n = 0$
8:      **while** $\|\eta_{n+1} - \eta_n\|_\infty \leq \mathsf{e}$ **do**
9:          $n = n + 1$
10:         Calculate η_n using ψ_{n-1} (C.6)
11:         Calculate ψ_n using η_n (C.7)
12:      **end while**
13:      $\eta(\boldsymbol{x}, t) = \eta_{n+1}$
       ** *Threshold/update the orientation field* **
14:      Identify interiors of grains: $I_p = \{\boldsymbol{x} \in \Omega \theta(\boldsymbol{x}, t) = \theta_p, \bar{\mathcal{J}}(\boldsymbol{x}) < \xi\}$, and set $I = \cup_{p=1}^n I_p$
15:      Evolve I with speed $1/(1 - \eta(\boldsymbol{x}, t))^2$ using the fast marching method
       and update/threshold the orientations at each point $\boldsymbol{x} \in \Omega - I$
16:      $t = t + 0.25\epsilon^2$ (3.8)
17: **end while**
18: Output: Time evolution of the polycrystal

	Grid Size	
ξ	1024×1024	2048×2048
0.15	9.77 %	2.32 %
0.10	7.74 %	1.24 %
0.05	3.39 %	0.71 %
0.02	2.58 %	0.07 %

Table 3.1: The effect of parameter ξ on deviations from the expected motion by curvature. We note that for a 2048×2048 grid, $\xi = 0.05$ is small enough to achieve an error less than 1%.

grain boundaries would stagnate. Since grain boundary evolution results in an overall decrease in curvature, (3.11) may cease to hold as the simulation progresses. Therefore, we adaptively increase ϵ when a grain boundary stagnates, and as a consequence, we obtain a time adaptive algorithm since $dt \propto \epsilon^2$. On the contrary an extremely small ϵ will increase the computational cost of the thresholding method. Thus, the parameter ϵ should be chosen wisely, which potentially requires a few numerical experiments.

Finally, we explore the effect of ξ, introduced in (3.10), on the extent to which (3.8) is satisfied. Recall that ξ was introduced in (3.10), which is necessary for identifying intial grain interiors. In the case of a circular grain (see Fig. 3.3a), the rate of change of radius can be analytically estimated from (3.8), which results in

$$\dot{R}(t) = -\frac{\epsilon^2}{4R(t)}. \tag{3.12}$$

To check if the above equation is satisfied, we ran the thresholding algorithm using the η-solution from the primal-dual algorithm with $\epsilon = 0.01$, and measured $\dot{R}(t)$. Relative % errors in shrinking-rate $\dot{R}$ at different values of ξ are summarized in Tab. 3.1. It is confirmed that for a sufficiently small grid, $\xi = 0.05$ is small enough to achieve an error less than 1%.
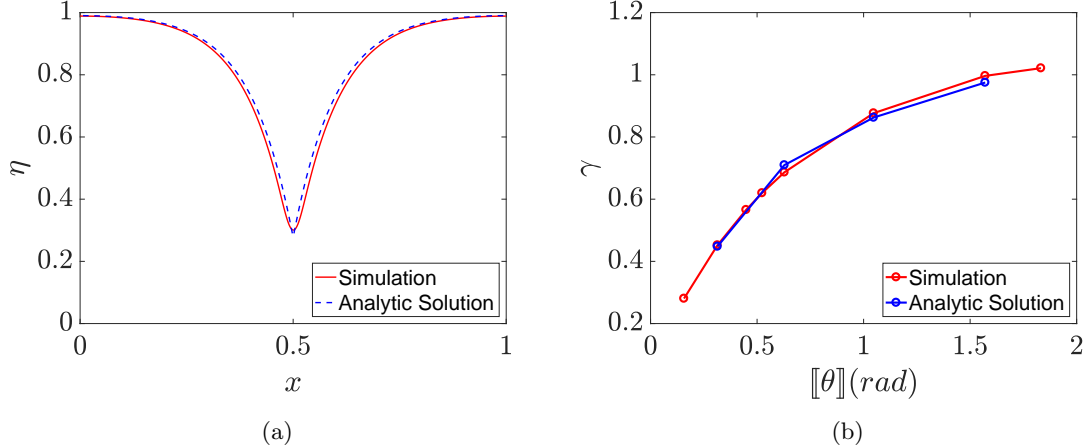
Figure 3.5: A comparison of the numerical solution resulting from the thresholding algorithm, implemented with $\epsilon = 0.1$ on a 512×512 grid, with the analytical solution. Plots of a) the steady-state solution η, and b) grain boundary energy as a function of misorientation.

We summarize our approach in Algorithm 1. Here, the core energy data $\mathcal{J}$ (e.g., Fig. 2.4) is computed separately using the procedure described in Section 2.4, and used as an input to our method. The algorithm alternates between the primal-dual and the fast marching methods resulting in motion by curvature. We also remark that the current approach can also be easily generalized for three-dimensional case as well.

Before we close this section, we comment on the computation of $[\![\theta]\!]$ (and also $\mathcal{J}$) on a discrete grid. Because $[\![\theta]\!]$, calculated at a grid point ij in either x- or y-directions using centered-difference, is shared between two grid points, a factor of $1/2$ appears in the following expression used to compute the total jump:

$$[\![\theta]\!]_{ij} = \frac{1}{2}\sqrt{(\theta_{i+1,j} - \theta_{i-1,j})^2 + (\theta_{i,j-1} - \theta_{i,j+1})^2}. \tag{3.13}$$

The above form conserves total $[\![\theta]\!]$ in a weak sense; it conserves the initial $[\![\theta]\!]$, when integrated across the grain boundary.

3.3 Numerical experiment

In this section, we present several results from numerical experiment that explore various features of grain boundary evolution predicted by our model.

We begin with a simulation of a one-dimensional bicrystal $\Omega = [0, 1]$ with a grain boundary at $x = 0.5$, and $\mathcal{J}([\![\theta]\!]) = [\![\theta]\!]$. The purpose of this simulation is to ensure that the results of the primal-dual algorithm for η-solution are consistent with the analytical model described in Appendix A. A Neumann boundary condition $d\eta/dx = 0$ is enforced at the two ends. In the absence of a curvature, we expect the grain boundary to remain at $x = 0.5$, and η reach its steady state. The tolerance e of the primal dual algorithm (C.8) is set to 10^{-6}. Fig. 3.5a confirms the agreement between η obtained from the primal dual algorithm and the analytical form given in (A.8). In addition, Fig. 3.5b shows that the grain boundary energies predicted by the primal-dual algorithm for various misorientation angles are in agreement with the analytical result derived in (A.10).

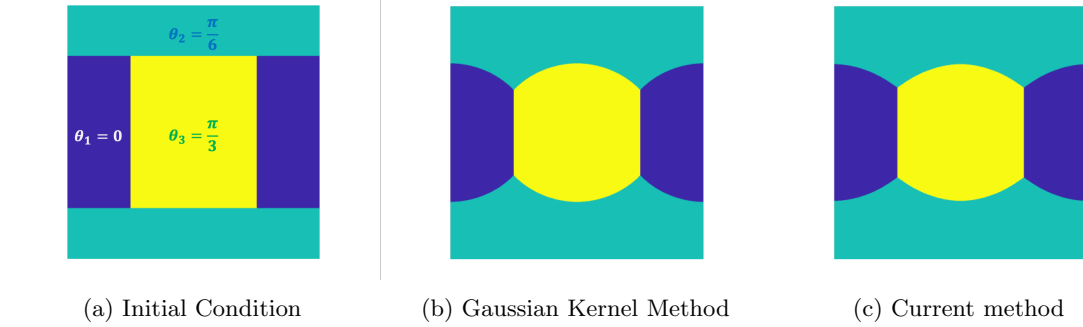| (a) Initial Condition | (b) Gaussian Kernel Method | (c) Current method |

Figure 3.6: A comparison of the evolutions of a tricrystal under periodic boundary conditions obtained using the Gaussian kernel method and the generalized KWC model with $\epsilon = 0.01$, implemented using our method. The dihedral angles predicted by the Gaussian kernel method and our method are $(93°, 133.5°, 133.5°)$ and $(106°, 127°, 127°)$ respectively, while the theoretical values are $(90.89°, 134.56°, 134.56°)$. In Fig. 3.7, we demonstrate that the error in the dihedral angles predicted by the generalized KWC model decreases as $\epsilon \to 0$.

3.3.1 Equilibrium of a triple junction

A triple junction is a line where three grains meet, and it is manifested as a point in two dimensions. The equilibrium of a triple junction is guaranteed if it satisfies the force equilibrium locally around the triple junction. The condition can be written in terms of the dihedral angles Θ_i of three grains, referred to as the Herring relation [72]

$$\frac{\gamma^{12}}{\sin\Theta_3} = \frac{\gamma^{23}}{\sin\Theta_1} = \frac{\gamma^{31}}{\sin\Theta_2}, \tag{3.14}$$

where γ^{ij} is the grain boundary energy density between the grain i and j.

Although the Herring relation is originally derived in the sharp-interface framework, not surprisingly, it is also seen to hold for a triple junction governed by the original KWC model through (2.4) [21]. This is because the KWC model converges to the Mullins model in the sharp-interface limit *and* the evolution in (2.4) is derived from a variational structure, i.e., the gradient descent of the functional in (2.1). However, our approach to evolve the generalized KWC model does not strictly arise from a variational formulation. Therefore, it is necessary to examine the Herring relation using our thresholding algorithm. We will now show that the Herring relation indeed holds provided the parameter ϵ is sufficiently small.

We examine the evolution of a triple junction in a tricrystal with orientations $\theta_1 = 0$, $\theta_2 = \pi/6$, and $\theta_3 = \pi/3$ in $\Omega = [0,1] \times [0,1]$. Using the Read–Shockley core energy $\mathcal{J} = [\![\theta]\!]$, we note from Fig. 3.5b that the energy density of the three grain boundaries are $\gamma^{12} = 0.62$, $\gamma^{23} = 0.62$, and $\gamma^{13} = 0.87$. From the Herring relation in (3.14), it follows that the steady state dihedral angles are $\Theta_1 = 134.56°$, $\Theta_2 = 90.89°$, and $\Theta_3 = 134.56°$ respectively. In order to check the Herring relation, we consider a tricrystal under periodic boundary conditions, with an initial orientation distribution given by

$$\theta(\boldsymbol{x}, t=0) = \begin{cases} \theta_2 & \text{if } x_2 \le 0.25 \text{ or } x_2 > 0.75, \\ \theta_3 & \text{if } 0.25 < x_2 \le 0.75 \text{ and } 0.25 \le x_1 < 0.75, \\ \theta_1 & \text{if } 0.25 < x_2 \le 0.75 \text{ and } x_1 > 0.25 \text{ or } x_1 > 0.75. \end{cases} \tag{3.15}$$

Fig. 3.6a shows a plot of the initial configuration of the tricrystal. Under this setting, we have four triple junctions at $(x_1, x_2) = (0.25, 0.75), (0.75, 0.75), (0.75, 0.25)$, and $(0.25, 0.25)$, of which initial dihedral angles

(a) Initial Condition

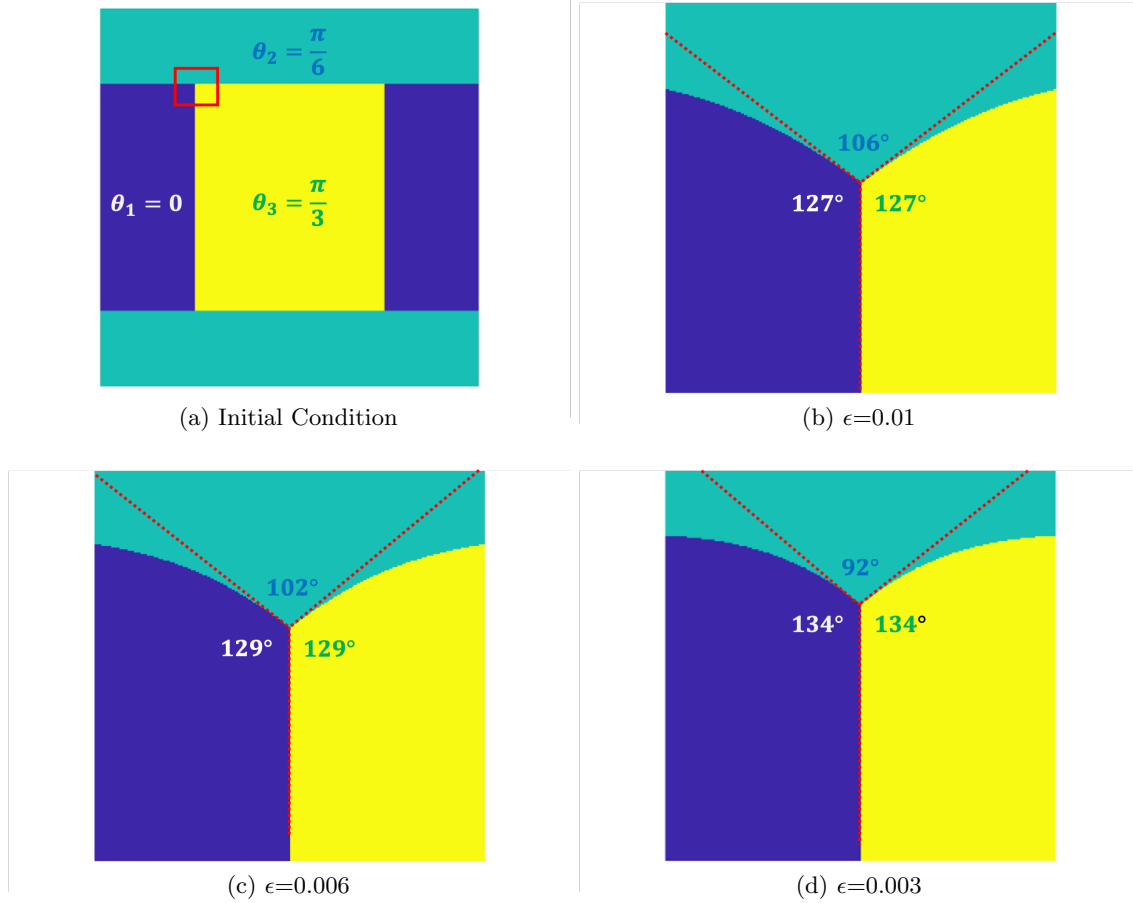(b) $\epsilon = 0.01$

(c) $\epsilon = 0.006$

(d) $\epsilon = 0.003$

Figure 3.7: a) The orientation distribution in an initial tricrystal under periodic boundary conditions with a triple junction at $(x, y) = (0.25, 0.75)$, and dihedral angles $(\Theta_1, \Theta_2, \Theta_3) = (90°, 180°, 90°)$. The polycrystal is evolved using the thresholding algorithm with $\epsilon = 0.01, 0.006$ and 0.003. b)-d) Closeups of an evolving triple junction (red box) clearly show that the dihedral angles converge to $(\Theta_1, \Theta_2, \Theta_3) = (134.56°, 90.89°, 134.56°)$ predicted by the Herring angle condition (3.14), as ϵ converges to zero.

are $90°$, $180°$, and $90°$.

We begin by comparing the evolution of a triple junction predicted by the KWC model implemented using our thresholding scheme with that acquired from the Gaussian kernel method [15]. The grain boundary energies $(\gamma^{12}, \gamma^{23}, \gamma^{13}) = (0.62, 0.62, 87)$, pre-computed using the KWC model, are used as inputs to the Gaussian kernel method. The respective mobilities are set to the inverse of the grain boundary energies. The parameter ϵ of the KWC model is initially taken as 0.01. Both schemes are simulated on a 1024×1024 grid. As shown in Fig. 3.6, the evolution dynamics of both schemes are qualitatively similar. In both methods, the triple junctions adjust at a much faster time scale to satisfy the Herring angle condition compared to the curvature-driven motion of grain boundaries [73]. The motion of triple junctions induces a curvature to the initially flat grain boundaries, resulting in the shrinking of the embedded grains (blue and yellow), while maintaining constant dihedral angles. The equilibrium dihedral angles predicted by the Gaussian kernel method are $(93°, 133.5°, 133.5°)$, while the generalized KWC model with $\epsilon = 0.01$ yields $(106°, 127°, 127°)$.

To further investigate the dependence of the triple junction angles on ϵ, we implement the thresholding algorithm with $\epsilon = 0.01, 0.006$ and 0.003 on a more refined 3000×3000 grid. As shown in Fig. 3.7b to
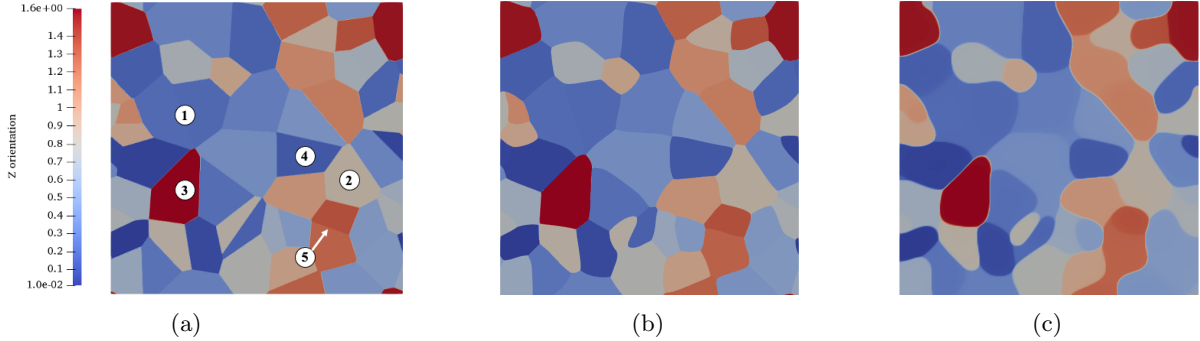
Figure 3.8: An initial polycrystal, shown in (a), is evolved using the thresholding and the finite element methods resulting in polycrystals shown in (b) and (c) respectively. The two methods are consistent in predicting the growth (e.g., ①, ②) and shrinkage (e.g., ③, ④) in various grains. The differences in the evolution is attributed to the mobility function introduced in (3.16) to prevent grain rotation.
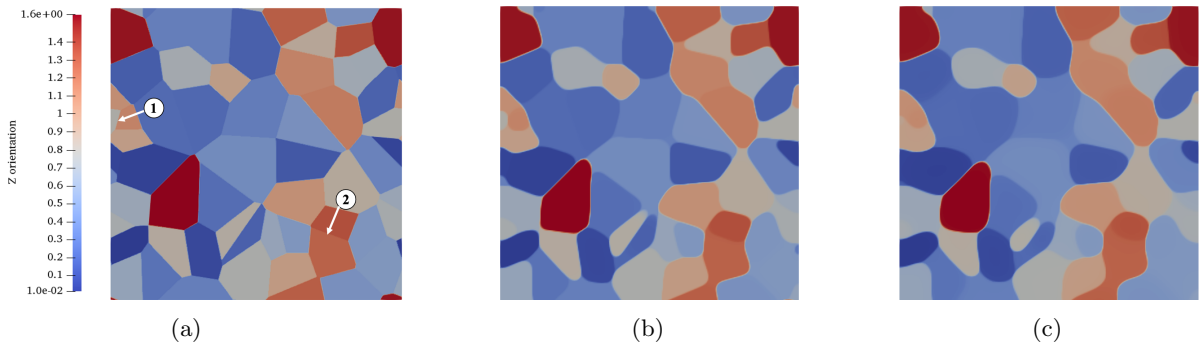

Figure 3.9: An initial polycrystal, shown in (a), is evolved using the finite element method. (b) and (c) show the resulting polycrystals with regularization parameters $\rho_0 = 2 \times 10^{-4}$ and $\rho_0 = 2 \times 10^{-3}$ respectively. When ρ_0 is not sufficiently small, grains with small misorientation (e.g., ①, ②) blend out and grain boundaries easily become rounded. However, the decrease in ρ_0 for simulating sharp interfaces, comes with significant computational cost contrasts to the suggested scheme.

Fig. 3.7d, as ϵ decreases, the stabilized triple junction angles converge to those predicted by the Herring relation. This test shows that the Herring relation is satisfied in the limit $\epsilon \to 0$.

3.3.2 Comparison with the finite element implementation of the KWC model

Next, we compare the evolutions of a polycrystal resulting form our method and a finite element implementation of the KWC model. The latter will be referred to as *FE-KWC* onwards. An initial polycrystal consisting of $\mathcal{N} = 50$ grains, as shown in Fig. 3.8a, is generated using a Voronoi tessellation of uniformly distributed random points. The orientations of the grains are randomly selected from the interval $[0, \pi/2]$. To make a closer comparison with the original KWC model, the core energy of the alternate KWC model is chosen to be of the Read–Shockley-type, i.e.$\mathcal{J} = [\![\theta]\!]$. The thresholding algorithm is implemented on a 1024×1024 grid, with parameters $\epsilon = 0.01$, $\mathbf{e} = 10^{-6}$, and $\xi = 0.05$. A snapshot of an evolving grain microstructure at $t = 5 \times 10^{-3}$, simulated using our thresholding scheme, is shown in Fig. 3.8b.

We note that FE-KWC, using continuous Lagrange finite elements, cannot be used for our new KWC model because the solution for θ is discontinuous. Therefore, we proceed with a finite element implementation

of the regularized KWC model given in (2.4). Second-order quadrilateral Lagrange finite elements are used to interpolate the order parameters. Since the regularized KWC model also allows grain rotation, we prohibit rotation using the following η-dependent mobility for θ

$$b_\theta^{-1}(\eta) = 10^{-5}\epsilon + \left(1 - \eta^3(10 - 15\eta + 6\eta^2)\right)(1 - 10^{-5})\epsilon, \tag{3.16}$$

as suggested by Ref. [67]. On the other hand, $(b_\eta)^{-1} = \epsilon$ is chosen to be constant. To address the singularity due to the $|\nabla\theta|$ term in (2.4b), we use the approximation

$$g(\eta)|\nabla\theta| \approx g(\eta)\sqrt{\rho_0 + |\nabla\theta|^2}, \tag{3.17}$$

where $\rho_0 = 2 \times 10^{-3}$ is a constant. The manifestation of ρ_0 on the solution will be discussed below. `Fenics` [74], an open-source computing platform, is used to perform FE-KWC simulation. We take an implicit time step with $dt = 0.012$. In order to compare the numerical efficiency, we ensure that the number of degrees of freedom is the same in the thresholding and the finite element simulations. The grain microstructure at $t = 1.71$, simulated using FE-KWC, is shown in Fig. 3.8c. Comparing Figs. 3.8b–3.8c, we note that both the methods are consistent in predicting growth (see ①, ②) and shrinkage (see ③, ④) in various grains. It is observed that grain boundaries become rounded in the finite element simulation, because of the diffusive nature of orientation field. In addition, disparities are more clear for small misorientation grain boundaries, e.g. ⑤, which became considerably diffused. This is a manifestation of the regularization parameter ρ_0, which results in a non-zero gradient in θ even in the grain interiors. In Fig. 3.9, we compare two finite element simulations with $\rho_0 = 2 \times 10^{-3}$ and 2×10^{-4}, which shows that for a smaller ρ_0, the grain boundaries maintain their characteristic width.[4] Thus, to simulate sharp grain interfaces comparable to the our scheme, a small enough ρ_0 is required for FE-KWC. However, we note that the smaller ρ_0 results in the more stiff governing equations, which significantly influences the computation time as discussed below.

A study on computational time of the schemes clearly highlights the strength of the thresholding scheme. Performance tasks are executed on a single 1.6 GHz core with 8 GB RAM, and we measured the wall-clock time to complete one-full time step for the two methods. For our method, this includes solving for η using the primal dual algorithm, and executing the fast marching based thresholding algorithm to update θ. In Fig. 3.10, we plot the dependence of the wall-clock time, as a function of the number of degrees of freedom N. The computational complexity of the current scheme is $\mathcal{O}(N \log N)$, with a dominant contribution from *Fast Fourier Transform* necessary for the primal dual algorithm to solve (C.7). On the other hand, the asymptotic computational cost of FE-KWC is estimated to be in between $\mathcal{O}(N)$ and $\mathcal{O}(N^2)$ as shown in Fig. 3.10. The computational bottleneck of FE-KWC is in solving — using a GMRES iterative solver [75] — a linear system of equations formed by an $N \times N$-sized sparse matrix. Although the asymptotic costs of the two schemes are similar in terms of N, we note that the computational cost of FE-KWC also depends on the choice of the regularization parameter ρ_0, which increases the stiffness of the equations in the limit $\rho \to 0$. Therefore, as demonstrated in Fig. 3.10, the current scheme can be orders of magnitude faster than FE-KWC. Both, FE-KWC and the implementation of our method, can easily be parallelized using the current generation of graphics cards, which have the power, programmability and precision to implement FFT and iterative matrix solvers [76, 77] respectively.

---

[4]Recall that the characteristic width of a grain boundary in the regularized KWC model is a function of ϵ.
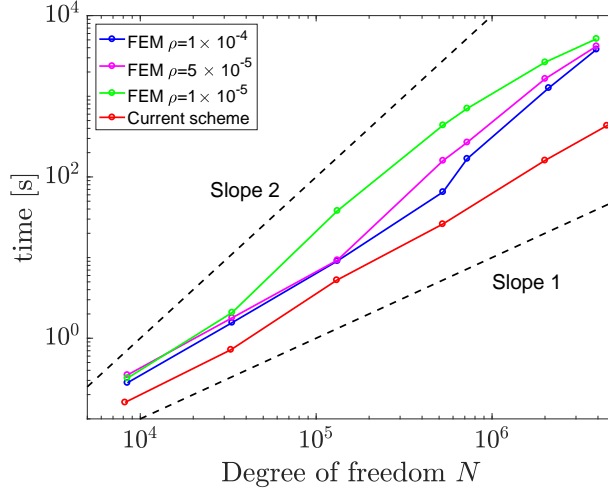
Figure 3.10: A comparison of the complexity of the thresholding and the finite element methods. The dashed lines represent reference slopes in the log-log scale plot. Slope 1 and 2 represent $\mathcal{O}(N)$ and $\mathcal{O}(\log N)$ respectively. While both methods have a complexity of at most $\mathcal{O}(N \log N)$, the cost of the finite element method depends on the choice of the regularization parameter ρ.

3.4   Grain growth in an fcc copper polycrystal

In this section, we examine grain growth in a two-dimensional fcc copper polycrystal with [110]-type grain boundaries simulated using the generalized KWC model,[5] with crystal symmetry-invariant grain boundary energy. We compare the results with the predictions of the original KWC model.

A two-dimensional polycrystal consisting of $\mathcal{N} = 50$ grains, with orientations in the range $[0, 70.6°]$ is generated using a Voronoi tessellation of random points. Fig. 3.12 shows the initial orientation distribution in the polycrystal. The grain boundary energy density is assumed to be independent of inclination. The core energy $\mathcal{J}(\llbracket \theta \rrbracket)$ constructed in Section 2.4 (see Fig. 2.4) is employed. In order to compare the generalized KWC model to the original KWC model, we scale the function g of the original KWC model in (2.1) to $g = -0.93 \ln(1 - \eta)$ such that the mean of the grain boundary energies as functions of misorientation in the range $[0, 70.6°]$ are identical for the two models. Fig. 3.11 shows a comparison of the grain boundary energy densities of the two models.

Figs. 3.12b–3.12c compares the orientation distributions of the polycrystal at the end of 200 time steps for the generalized and the original KWC models. Comparing the resulting polycrystals with the initial polycrystal in Fig. 3.12a, we note that the generalized KWC model predicts a growth for red grains while the original model results in their shrinkage. This is attributed to the difference in the grain boundary energies of the two models, as shown in Fig. 3.13. For example, the grain boundary ①, which has a misorientation of $\approx 70.6°$, has a relatively smaller energy in the generalized model due to crystal symmetry.

On the contrary, we note an opposite trend for light blue grains for which the generalized model predicts shrinkage while the original model results in a growth. This is a result of relatively larger energy of grain boundary ② in the generalized model compared to the original model. The above observations suggest that the generalized model can result in the growth of certain grains with large misorientation, emphasizing the importance of crystallography in grain growth.

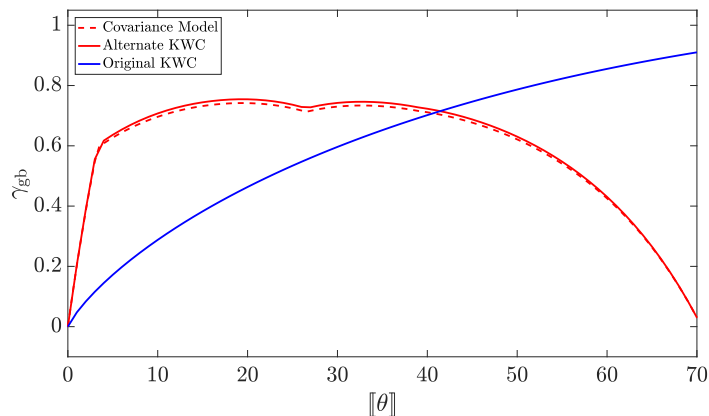[5]The [110] direction of each grain is is aligned with the z-axis (out of the plane).

Figure 3.11: Grain boundary energies used for the polycrystal simulation in Section 3.4. Using a core energy $\mathcal{J}(\llbracket\theta\rrbracket)$ designed in Section 2.4, we obtain a crystal symmetry-invariant KWC model with energy that matches the covariance model. In order to compare the original and the new KWC models, we scale the function g of the original KWC model in (2.1) to $g = -0.93\ln(1 - \eta)$ such that the averages of the grain boundary energies (with respect to misorientation) are identical in the two models. In other words, the areas under the above plots are equal.

3.5 Summary of Part I

We now summarize the first half of the thesis. In Chapter 2, we generalized the two-dimensional KWC model to incorporate misorientation-dependent grain boundary energies that respect bicrystallography. The computational challenge of solving the singular diffusive equation of the KWC model was addressed by developing an $\mathcal{O}(N\log N)$ thresholding algorithm. Below, we list some potential research directions that extend the current approach.

- The present framework will enable us to carry out a statistical study of large scale simulations of various ensembles of polycrystals to characterize grain growth in terms of the grain boundary energy landscape and crystal symmetry.

- While arbitrary grain boundary energies are incorporated into our model, its implementation is restricted to grain boundary mobility equal to the inverse of the energy. An extension of our algorithm to include mobilities independently can also be explored.

- The present algorithm does not allow grain rotation, which is another important phenomenon during recrystallization of polycrystalline materials.[6] To capture this, a step that models grain rotation should be augmented with the current scheme.

- A recent work by Admal *et al.* [64] extended the two-dimensional KWC model to a three-dimensional fully anisotropic (both misorientation and inclination dependent) model, wherein the dependence of grain boundary energy on the misorientation angle was restrictive to a Read–Shockley-type. Due to the

---

[6]We note that grain rotation may sometimes play an important role during the transition from recovery to continuous dynamic recrystallization. Dislocations agglomerate and form cell walls/subgrains at the end of the recovery stage. In a phenomenon, commonly referred to as *subgrain rotation recrystallization*, few subgrains — aided by bulk dislocations – increase their misorientation and transform to grains/nuclei which grow [78]. From this perspective, grain rotation plays an important role during the nucleation of recrystallized grains.
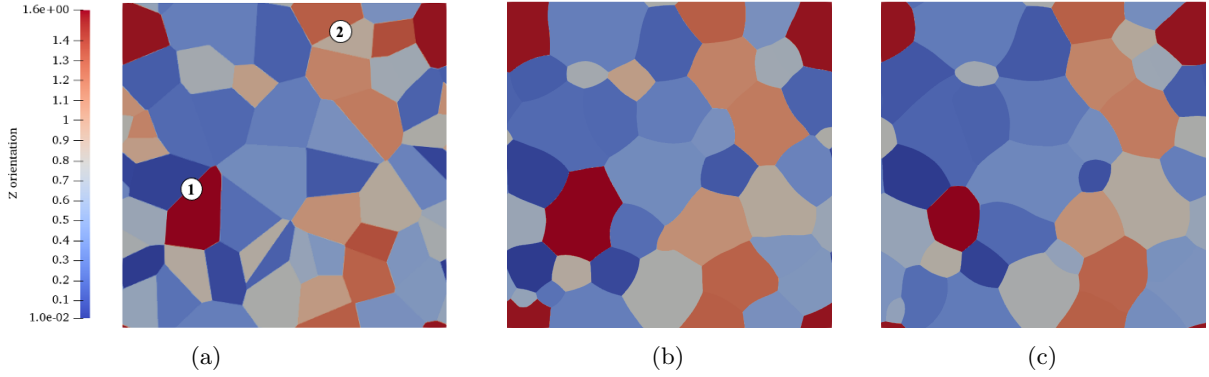
Figure 3.12: (a) A polycrystal with $\mathcal{N} = 50$ grains, and an initial orientation distribution. (b) and (c) show evolved polycrystals using the new and the original KWC models respectively. Grains 1 and 2 show opposite growth/shrinkage trends in the two models due to the deviation of the grain boundary energy from the Read–Shockley-type in the new formulation. The blue and red colors represent the maximum and minimum orientation angles of $0°$ and $70.6°$ respectively.
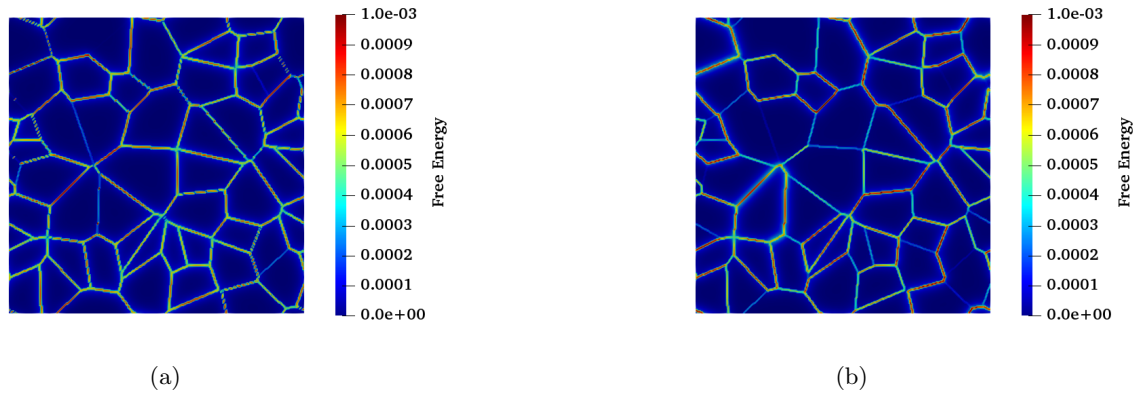

Figure 3.13: Initial distributions of grain boundary energies for the (a) generalized, and (b) the original KWC models. The grain boundary energy in the original KWC model is of the Read–Shockley-type. On the other hand, the grain boundary energy in the generalized KWC model reflects the crystal symmetry of copper.

high computational cost of the finite element method, the implementation of the three-dimensional model was restricted to simple bicrystals. It is envisaged that the efficiency of our thresholding algorithm will enable us to explore large three-dimensional polycrystals with fully anisotropic grain boundary energy.

- Finally, we recall from the introduction that surface tension is not the only dominant driving force on a grain boundary due to grain boundary plasticity. Adapting our thresholding algorithm into existing unified frameworks [79], wherein grain microstructure and deformation evolve contemporaneously, will enable us to quantify the role of grain boundary plasticity, and study phenomena such as dynamic recrystallization, superplasticity and severe plastic deformation [80–82].

In the following chapter, we embark on the first direction among listed above. In particular, our goal is to construct a lightweight model for grain statistics. To construct and validate a reduced order model for grain statistics, we will use simulation results of generalized KWC-model using the thresholding method.

Chapter 4

A stochastic framework for grain statistics

In this second part of the thesis, we will study grain growth from a statistical perspective. Specifically, the main goal of this chapter is to develop *a reduced order model*, a computationally light model that describes the evolution of grain statistics, as opposed to the evolution of a fully resolved microstructure. Here, the reduced order model is a machine learning-based model, which will be trained using the data generated by a higher model, such as the KWC model developed in the Section 2.

4.1   Toward a reduced order model for evolving grain statistics

While phase field models are capable of predicting the evolution of full-field micro structure, including all geometric descriptors of grains (e.g. shape, size, topology, aspect ratio, and perimeter), they are computationally expensive to resolve every grain boundary. However, to establish the process-microstructure–property relationship, it is necessary to consider an ensemble of grain microstructures as opposed to a single microstructure. This is because the space of grain microstructures is enormously large compared to the finite size of the space of process parameters and properties [14]. Moreover, macroscopic properties of a polycrystal are properties of average microstructure features. Unfortunately, it is challenging to embark on a statistical study of ensembles of polycrystals using phase field models because of their excessive computational costs. Here, we are considering a system consisting of more than 10,000 grains, in which statistical studies of grain characteristics are valid. This leads us to envision a sufficiently light-weight model such that it can be repeatedly used during the iterative material design process in Fig. 1.2. If available, such a lightweight model will have immediate impacts in the field of advanced manufacturing [83–87].

We recognize that among various descriptors for polycrystals the one most important descriptor is the grain size distribution, which indicates a characteristic scale of inhomogeneity. For example, a number of empirical models of plastic deformation, diffusion creep, electromigration, effective low-temperature diffusivity take into account the grain size distribution [88–93]. Thus, we aim to develop a reduced order model capable of predicting the size distribution of polycrystals with a marginal computational cost.

In this chapter, we will focus only on two-dimensional *isotropic* grain growth, where both the grain boundary energy γ and mobility m are constant. We already know that during grain growth the average grain area A_{avg} increases, while the number of grains decreases with time. This implies that some grains

grow at the expense of others. Then, how do we know which grains grow and what their growth rates are?

The simplest models for predicting the grain size (or grain area in two dimensions) is the von Neumann–Mullins law [16, 94], which states the rate of change of area A of a grain:[1]

$$\frac{dA}{dt} = \frac{\pi}{3}m\gamma(S - 6).\tag{4.1}$$

The implication of the von Neumann–Mullins rule is that the area change rate of a grain depends exclusively on its topology S, and not on its shape. By topology, we are referring to the number of sides/faces of a grain, which uniquely determines grain topology in two dimensions. The von Neumann–Mullins law (4.1) is significant reduction and serves a powerful deterministic rule for predicting the next size states of individual grains in a polycrystal without using sophisticated models of grain boundary motion. However, despite the availability of von Neumann–Mullins law, grain growth in a polycrystal becomes far more complicated phenomena, as grains also continue to change their topology, resulting in an abrupt change in growth rate. In addition, as noted in Section 2.2, such critical events pose serious challenges to many of grain boundary models. Thus, a model that completely describes a grain microstructure evolution should predict the discrete topology transformations.

One of the most successful approaches for grain topology transformation is again the phase field model [54, 95, 96], which we have also developed our own kind in the earlier chapter. Recall that this class of models evolve phase fields, representing the grains, using the principle of maximum dissipation of a free energy functional. Fortunately, in phase field models, the topology transformations of grains are automatically handled by the same principle without any augmented rule. However, again the downside of phase field models is the high memory and computational costs associated with resolving every thin grain boundary. Moreover, although topology transformations of grains are predicted in the phase field models, the explicit rules governing the transformations, which are critical for developing reduced-order models, are not fully established. [2]

Knowing that the grain topologies are essential in predicting their sizes, our goal becomes more clear; in this chapter, we will develop a new model for grain topology transformations, which will be combined with the von Neumann–Mullins rule and used to predict a time-evolution of the joint distribution for grain size and topology.

4.2   Conventional approaches for grain size statistics

Before we proceed to develop our framework for grain statistics, we review traditional approaches to grains statistics. Interestingly, it has been observed that during nomal grain growth, a grain size distribution evolves towards an asymptotic self-similar state, regardless of initial states [33, 39, 102, 103]. For example, Fig. 4.1 illustrates different asymptotic grain size distributions obtained from experiments, front-tracking simulation, and the mean field theory [39, 97–101, 104], which are characterized by their own asymptotic self-similar states. We note here that the mechanisms governing topology transformations that result in a self-similar asymptotic grain statistics remain unknown. This observation, in addition to the technological relevance of a lightweight model to design advanced manufacturing processes, is the main motivation for this work.

---

[1]Here, we note that the von Neumann–Mullins law only holds for isotropic grain growth.

[2]This is analogous to the observation that while molecular dynamics (MD) can predict the evolution of defects at the atomic scale, it does not describe the mechanics governing the configurational forces between defects at the mesoscale. Defect mechanics models serve this purpose, and play a critical role in analyzing the mechanical response of large systems, which are not accessible by MD simulations.
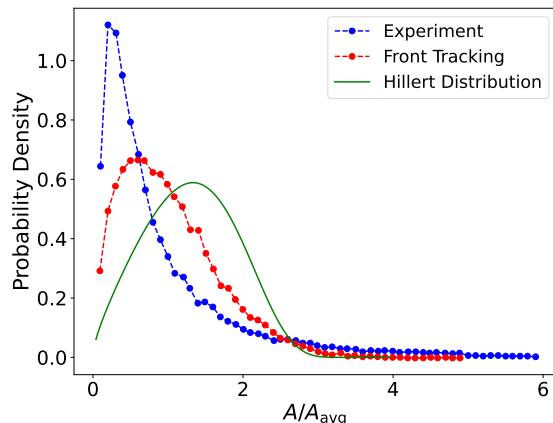
Figure 4.1: The blue, red and green curves show the asymptotic distributions of grain areas observed in experiments on Cu and Al films [97–100], simulations using the front tracking method [101], and the mean field prediction [39] respectively. The experimental data was obtained at different film thicknesses and annealing temperatures. Regardless of these conditions, the grain size distributions attain self-similar states. While the disagreement between experiments and front tracking may be attributable to anisotropic grain growth, the disagreement between the latter two is a consequence of poor coarse-graining of the Hillert model.

Conventional theoretical studies on grain statistics are grounded in a continuum approach that aims to track a grain size distribution $F(R, t)$, where $R = (A/\pi)^{1/2}$ is the equivalent circle radius for a given grain area A, and $F(R, t)$ denotes the fraction of grains having a size between R and $R + dR$ at time t. Assuming the polycrystal is an infinite collection of grains, F is assumed to be smooth and satisfies the following continuity equation [105]:

$$\frac{\partial F(R, t)}{\partial t} + \frac{\partial}{\partial R}\left[F(R, t)\dot{R}\right] = 0. \tag{4.2}$$

The growth rate $\dot{R}$ in (4.2) is assumed to be a function of grain size. For example, Hillert [39] took a mean-field approach and assumed that the net growth rate of a grain in an ensemble could be expressed through the mean difference between the curvature of the grain's boundaries,

$$\frac{dR}{dt} = m\left(\frac{1}{R_c} - \frac{1}{R}\right), \tag{4.3}$$

where $1/R_c$ is the time-dependent critical curvature of the grain ensemble. The expression (4.3) for $\dot{R}$ in reduces the continuity equation (4.2) to a first-order partial differential equation, which is tractable using analytic approaches. Then, the well-known Hillert grain size distribution [39] is obtained as the steady-state solution of (4.2). However, as demonstrated in Fig. 4.1, the Hillert distribution markedly disagrees with experiments and the computer simulations of two-dimensional isotropic grain growth. One of the primary reasons is that Hillert [39] neglected the effect of grain topology on growth rate by assuming all-spherical grains [106, 107]. Then, a question arises, "how do we include the influence of grain topology?". The fact that even a similar sized grains can have different topologies, alternatively motivated stochastic methods for grain growth [105, 108], which combine with the continuum approach (4.2). This results in an additional diffusion term $D(\partial^2 F/\partial R^2)$ in (4.2) arising from random fluctuations of $\dot{R}$. However, the choice of diffusion constant D remains phenomenological.

In our view, a model for grain statistics should both incorporate the topologies of the grain and their connectivity. This is because while the topological state of a grain determines its growth rate $\dot{R}$, the rules for grain topology transformations not only depend on the state of a grain but also its neighbors. For instance, during grain growth some grains vanish at the expense of growing grain. If a grain shrinks out, then all of its neighbors would lose one of their sides/faces at the same time. Subsequently, as grain growth continues, grains will merge and start to interact with others that were initially located at far distances. However, tracking the entire connectivity information in a large ensemble itself is also a non-trivial problem. To address this issue in the following, we suggest a new stochastic framework to efficiently evolve statistics of coarse-grained descriptors of a microstructure.

4.3 A stochastic framework for evolving grain statistics

4.3.1 Overview of the statistical framework

We first give a broad overview of our two-dimensional statistical framework to evolve a joint distribution of coarse-grained descriptors of a grain microstructure. In a 2D polycrystal with isotropic grain boundary energy, a grain microstructure is defined by the complex network of lines that represent the grain boundaries. Under the assumption that the network is *spatially homogeneous*, we begin by determining a coarse-grained description of a grain microstructure.

There are many geometric features of a grain — such as area, number of sides, lengths of its edges, isoperimetric ratio, convex hull ratio, etc. — that serve as potential coarse-grained descriptors. We choose the area A and the number of sides S (also termed "edges") of a grain as its coarse-grained descriptors. If a microstructure consisting of a large number (N_∞) of grains is spatially homogeneous, then it can be statistically represented by a smaller number $N < N_\infty$ of non-interacting grains, which we refer to as *rep grains*. A depiction of coarse-graining using rep grains is shown in Fig. 4.2. Invoking spatial homogeneity once again, we assume that the distribution of neighbors of each rep grain is identical to the distribution of the rep grains. Under this setting, a polycrystal at time $t = 0$ is statistically represented by N identically distributed rep grains with their areas A_i and number of sides S_i ($i = 1, \ldots, N$) sampled from a joint distribution F. We refer to the pair (A_i, S_i) as the *state* of the i-th grain.

The input to the framework is an initial joint distribution $F(A, S, t = 0)$, and the output is the time evolution of the joint distribution. This type of input data can be acquired from electron backscatter diffraction (EBSD) maps [109, 110]. Starting with initial N rep grains, their initial states are sampled from $F(A, S, t = 0)$. At each time step, the areas of the rep grains can be updated based on their present topology using the von Neumann's law (4.1). Next, we also need to update the topologies of rep grains, as grain also undergo topology changes during grain growth.

One of the central goals of this chapter is to develop a probabilistic reduced order model to predict the topology changes of the rep grains using their coarse-grained descriptors (A_i, S_i). We refer to this model as the *topology transformation model* (TTM). The underlying hypothesis behind TTM is that the probability that a rep grain undergoes a topology change can be described as a function of the states of the rep grain and its neighbors. Recall that the neighbors of a rep grain can be sampled from the current distribution of the rep grains. Therefore, TTM expresses the probability of topology change of a rep grain in terms of its current state and the state of its neighbors that are sampled from F.

Using the von Neumann–Mullins law in conjunction with the TTM, we evolve the grain state distribution
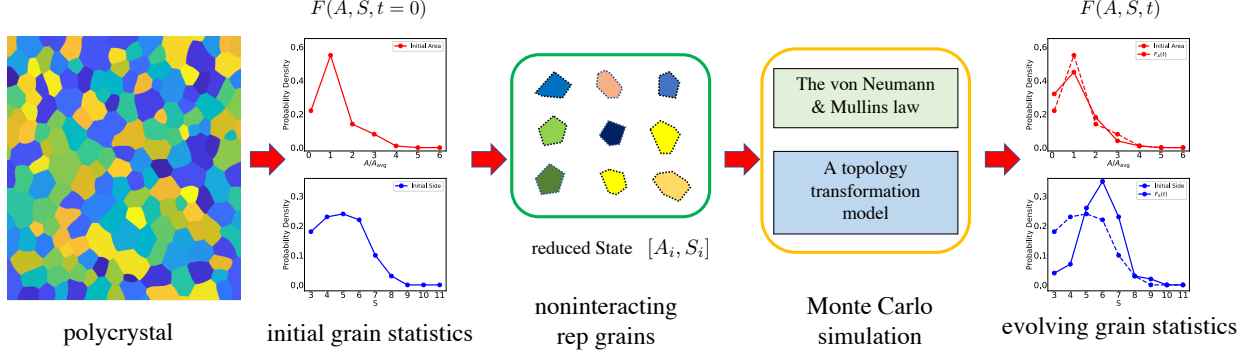
Figure 4.2: A schematic of the stochastic framework. A polycrystal is represented by a collection of coarse-grain descriptors (A_i, S_i) of N non-interacting representative (rep) grains drawn from an initial given joint distribution $F(A, S, t = 0)$. Sampling the grain states from a given initial joint distribution, we evolve the states of rep-grains with the von Neumann–Mullins law and a topology transformation model (TTM). The TTM yields the probability that the topology of a rep grain transforms in terms of its state and the states of its neighbors. The entire framework is implemented under a MC simulation resulting in an evolution of the joint distribution $F(A, S, t)$.
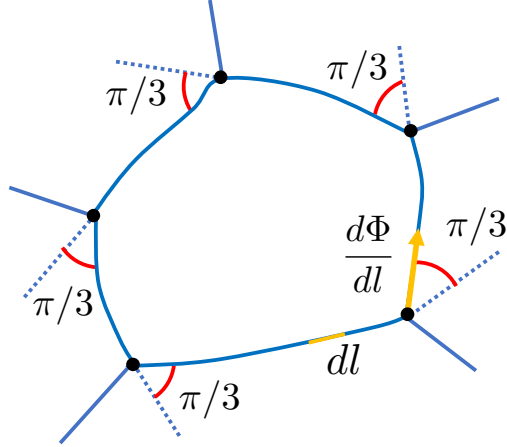

Figure 4.3: An example grain with five sides. Under isotropic grain boundary energy, all the internal angles at vertexes are equal to 120°.

F in a Monte Carlo (MC) simulation. Note that the MC simulation we conceive here is fundamentally different from conventional MC simulations [34–38] for grain microstructure as the latter evolve grain boundaries but not distributions. Fig. 4.2 summarizes the entire stochastic framework.

4.3.2 The von Neumann–Mullins law

The von Neumann–Mullins law (4.1) is the first tool that we will use in the MC simulation to evolve the area descriptors for rep grains. Here, we provide more backgrounds on the von Neumann–Mullins law.

For isotropic grain growth in two dimensions, the von Neumann–Mullins law states that the rate of change of area of a grain is a function of its number of sides S. The theorem can be derived using the Mullins model of motion by curvature (1.1) and the Herring angle condition [72]. Below, we adapt a proof from Ref [16]. For demonstration, consider a typical example of a grain in Fig. 4.3. Under isotropic surface tension the three

dihedral angles of a triple junction are equal to 120°. Then, the rate of change of the grain area A can be

$$\frac{dA}{dt} = \int v \, dl,$$

where v is the grain boundary velocity normal to the surface and dl is an element of the perimeter of grain. Substituting the Mullins' model $v = -m\gamma\kappa$ (1.1) with $\kappa = d\Phi/dl$, where Φ is the tangential angle at any given point of grain boundary, yields

$$\frac{dA}{dt} = -m\gamma \int d\Phi. \tag{4.4}$$

If the grain were surrounded by a smooth surface, then the integral (4.4) would equal 2π. However, for each vertex, the discontinuous angular change $\Delta\Phi = \pi/3$ should be subtracted from the total value 2π. Consequently, this yields the von Neumann–Mullins law (4.1).

On the other hand, rate of change of volume of a grain in higher dimensions is not entirely topological [111], i.e. it depends on the shape of the grain. However,it is expected that a topology-dependent growth rate would hold in 3D in a statistical sense. For example, the average volume change rate for grains with F faces can be estimated as an exclusive function of F [112, 113].

Despite the availability of an analytical expression (4.1) for grain growth rate, an analysis of grain size distribution becomes a challenging task, since the topologies of grains in a polycrystal continue to transform. Since topology transformation of a grain is a complex phenomenon, it cannot be deterministically described in terms of the coarse descriptors (A_i, S_i), which are only observables in the outlined framework. This motivates us to seek a probabilistic model for topology transformations.

4.3.3 Backgrounds on grain topology transformation model

The goal of TTM is to establish the rules governing grain topology transformations during grain growth within a coarse-grained framework, wherein a polycrystal is described statistically by a joint distribution for the area and topology of a collection representative grains. Due to the coarse-grained description of a polycrystal, we may not have a complete set of parameters that deterministically predict grain topology transformations. Therefore, we seek a probabilistic understanding of topology transformation.

Limiting our discussion to two dimensions, we first begin by reviewing the current understanding of grain topology transformation to develop a TTM.
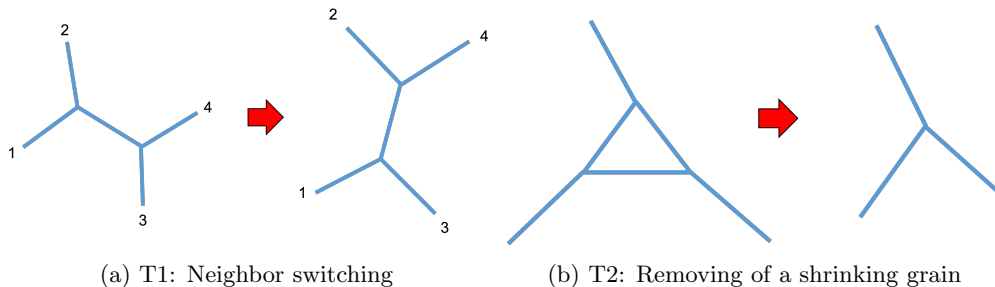

(a) T1: Neighbor switching   (b) T2: Removing of a shrinking grain

Figure 4.4: Two scenarios of topology transformation during 2D grain growth. The schematic is adapted from Ref. [45].

The T1 and T2 topology transformation mechanisms

In two dimensions, the two dominant mechanisms for topology changes are referred to as the T1 and T2 processes [45]. First, T1 is a neighbor-switching process that involves four grains, resulting in a redistribution of the number of sides of the four grains (see Fig. 4.4a). It is initiated by the shrinking of an edge shared by two grains. As the shared edge shrinks, its two triple junction ends converge to one point, transforming to a quadruple junction. Since higher-order (≥ 4) junctions are unstable [114], the quadruple junction splits into two new triple junctions almost instantaneously. The consequence is changes in neighbor relations. In particular, the pair of grains that shared the shrinking edge are no longer neighbors, while their neighbors become neighbors to each other.

The T2 process involves the removal of a shrinking grain. According to the von Neumann–Mullins law (4.1), shrinking grains are either 3,4, or 5-sided. Although it is sometimes conjectured that every shrinking grain becomes three-sided eventually before vanishing, this has not been conclusively established [115]. Rather, the disappearing of four and five-sided grains are often observed both in experiments [116] and simulations [117]. Therefore, we will not confine the T2 process to the removal of triangular grains, but also include the removal of four and five-sided grains as well. When a triangular grain shrinks and disappears, all of its neighbors lose an edge. There is no emergence of a new connection, because all the neighbors were also neighbors to each other. When a quadrilateral or a pentagon-shaped grain shrinks and disappears, some of its neighbors lose an edge, while others preserve their previous topology by building new neighborhood relations between them.

Although the possible scenarios of grain topology transformation described above are simple, such a qualitative description is not sufficient to construct a quantitative model. This leads us to consider a probabilistic model of grain topology transformation.

TTMs in literature

In fact, probabilistic descriptions of grain topology transformations have a long history that dates back to the 1970s [118–124]. Some of the early studies include the works of Blanc and Mocellin [118] and Carnal and Mocellin [119], who investigated the evolution of grain side distribution during isotropic grain growth. Their model simply adopted an equi-probable rule of topology change for all grains regardless of their states. The model included the fraction of triangular grains as a free parameter, which was chosen such that the predicted side distribution matches a target distribution observed in experiments.

The co-evolution of grain area and side descriptors by Fradkov [121] and Fradkov *et al.* [122] is similar to our framework introduced in Section 4.3.1 where both the von Neumann–Mullins law and a TTM are used. The TTM in [121, 122] was inspired by the random collision models of gas dynamics. The connectivity between grains was neglected and the T1 process was interpreted as an exchange of sides during grain "collisions". The model also includes a free parameter that describes the ratio of number of times a side is gained to the number of times a side is lost. Similar to the previously described model, the free parameter is chosen to ensure the predicted side distribution matches a target distribution. The predicted area distribution, however, has an exponential form — $F(R) \approx \exp(-R)$ — as opposed to the one shown in Fig. 4.1.

On the other hand, Flyvbjerg [120] proposed a model that has no free parameters to statistically evolves side and area states of grains. The model assumes that all topology changes are mediated by the T2 process and ignores the T1 process for simplification. The shrinking and vanishing of a grain, governed by the von Neumann–Mullins law, triggers a topology change of a neighbor that is randomly chosen with a probability proportional to the number side S. The rates at which grains gain or lose an edge by the T2 process is

determined dynamically reflecting the grain statistics at current time. The resulting grain area distribution, however, also has an exponential form.

A more realistic grain area and side distributions for isotropic growth was predicted by the model of Beenakker [124], who also ignored the T1 process but instead tracked the actual connectivities between grains. In the event of a grain vanishing, new connections are built between two neighbors randomly chosen with equal probability. Since the algorithm involves the bookkeeping process of tracking the connectivities between grains, its implementation is relatively tedious [124]. Moreover, it is not clear whether the ignoring the T1 process remains reasonable if the model is extended to anisotropic surface energies.

In the following sections, we will construct a TTM model that involves no free parameters. This is accomplished by constructing the probability of a grain topology change as a function of states of the grain and its neighbors. Evidently, the high dimensionality of the probability function enables the model to be parameter-free in the sense that a target distribution is not required to fit the model.

4.3.4   A new model for grain topology transformations

Seeking a reduced-order model for grain topology transformation we postulate that the probability that a grain undergoes a topology change after some fixed time Δt [3] can be characterized as a function of its state and the states of its first nearest neighbors. The effect of second-nearest neighbors and beyond is assumed to be marginal, and therefore, ignored.

Consider an arbitrary rep grain with area $A_i = A$ and number of sides $S_i = S$. It is surrounded by S neighbors. Let a_α and s_α ($\alpha = 1, \ldots, S$) denote the areas and sides of the S neighbors, respectively. Note that we are using lowercase letters to denote the states of the neighbors and uppercase letters to denote those of rep grains. Here, we assume that the neighbors are ordered by descending areas. Recall that within our stochastic framework, the neighbor grains are sampled from the joint distribution of the rep grains. In this section, we assume that a collection of S neighbors are drawn from the distribution F and given to us. Now, the objective of this section is to construct probability functions $\mathcal{F}_S$ ($S = 3, 4 \ldots,$), where each $\mathcal{F}_S$ describes the probability that the topology of a S-sided rep grain, expressed in terms of the state (A, S) and the states $\{(a_\alpha, s_\alpha) : \alpha = 1, \ldots, S\}$ of its neighbors, changes.

In principle, we could begin by seeking a probability $\mathcal{F}_S$ as a function of (A, S) and (a_α, s_α). However, we recognize that a more ideal combination of function arguments exists which is physically meaningful. Note that under appropriate rescaling of spatial and temporal scales, the probability should be scale-invariant. Therefore, we intend the arguments of $\mathcal{F}_S$ to be intensive as opposed to extensive. Since areas are extensive, it is reasonable to normalize them. Therefore, the normalized areas $\{a_\alpha/A : \alpha = 1, \ldots, S\}$ form a subset of the arguments of $\mathcal{F}_S$.

Next, we hypothesize that a topology change not only depends on the current normalized areas but also current rate at which they are evolving. Since the rates are governed by the von Neumann–Mullins law (4.1), we introduce the normalized rates

$$v_\alpha = \frac{\left(s_\alpha \frac{\pi}{3} - 2\pi \right) \Delta t}{a_\alpha}, \quad (\alpha = 1, \ldots, S) \tag{4.5}$$

for each neighbor grain. Similarly, we define a normalized rate V for the rep grain as

$$V = \frac{\left(S \frac{\pi}{3} - 2\pi \right) \Delta t}{A}. \tag{4.6}$$

---

[3]Here, Δt corresponds to the time step size in the stochastic framework.

Introducing the von Neumann–Mullins law into the TTM makes it more physically informed. Furthermore, since v_α and V converge to $-\infty$ as the corresponding grains shrink to a point, we anticipate the rates may serve as indicators for grains that are about to vanish.

In addition to the normalized areas and area described above, an observation that the simultaneous shrinking of two connected neighbors triggers the T1 process (Fig. 4.4a), suggests the connectivity between neighbors is critical for describing topology transformations. Therefore, we include the connectivity between neighboring grains in the set of arguments of $\mathcal{F}_S$. To convey connectivity of neighboring grains, we use an $S \times S$ adjacency matrix $\boldsymbol{C}$ defined as follows. If two neighbor grains α and β are neighbors themselves, then the $\alpha\beta$ element of $\boldsymbol{C}$ is

$$C_{\alpha\beta} = \frac{0.5(a_\alpha + a_\beta)}{A},$$

and $C_{\alpha\beta} = 0$, otherwise. Because neighbors are ordered based on decreasing areas, permutations of the rows and columns of $\boldsymbol{C}$ are disallowed, thereby resulting in a unique $\boldsymbol{C}$. Note that the number of independent non-zero elements of $\boldsymbol{C}$ is only $S(S-1)/2$, because $\boldsymbol{C}$ is a symmetric matrix and the diagonal elements are always zero. Summarizing the above discussion, we express the probability that the topology of a rep grain transforms as a function of $S+1$ normalized areas and rates, and $S(S-1)/2$ entries that describe neighbors adjacency matrix.

As mentioned in the beginning of this section, we assume that during a Δt time step, the topology of a rep grain may (a) remain unchanged $\Delta S = 0$, (b) gain or (c) lose an edge through a T1 process $\Delta S = \pm 1$, or (d) disappear through a T2 process $\Delta S \leq -3$. Here, we assumed that the number of edges of a grain does not increase or decrease by more than one at a time during the T1 process, while the T2 process corresponds to the case where a grain loses more than three edges simultaneously. Therefore, $\mathcal{F}_S$ is expressed as

$$\mathcal{F}_S \left(\frac{a_1}{A}, \frac{a_2}{A}, ..., \frac{a_S}{A}, V, v_1, ...v_S, \boldsymbol{C} \right) = (p_1, p_2, p_3, p_4), \tag{4.7}$$

where

$$p_i = \begin{cases} \Pr(\Delta S = 0) & \text{if } i = 1, \\ \Pr(\Delta S = +1) & \text{if } i = 2, \\ \Pr(\Delta S = -1) & \text{if } i = 3, \\ \Pr(\Delta S \leq -3) & \text{if } i = 4. \end{cases}$$

In the above equation, Pr denotes the probability of an event. Note that the total number of inputs of $\mathcal{F}_S$ is $0.5(S^2 + 3S) + 1$. In the next section, we employ fully-connected neural networks to determine $\mathcal{F}_S$ (4.7) for each $S = 3, \ldots, 9$ using training data collected from the phase field method developed in Chapter 3.

4.4 A data-driven approach to TTM

In this section, we formulate an optimization problem to construct the set of probability functions $\{\mathcal{F}_S : S = 3, 4, \ldots \}$ that constitute the TTM using a deep neural network. Deep learning is a class of machine learning algorithms that uses multiple layers of artificial neural networks to *learn*, or approximate, an unknown function. Recent advances in deep learning algorithms allow us to explore new fields in computational mechanics that could not be tractable without them [125–129]. In this work, we use *supervised learning* techniques to learn a map that is known for a given set of inputs $\boldsymbol{x} = (a_1/A, a_2/A, ..., v, v_1, ..., C_{11}, C_{12}, ...)$ and observed outputs ΔS from a training data structure. In a machine learning context, such a task is
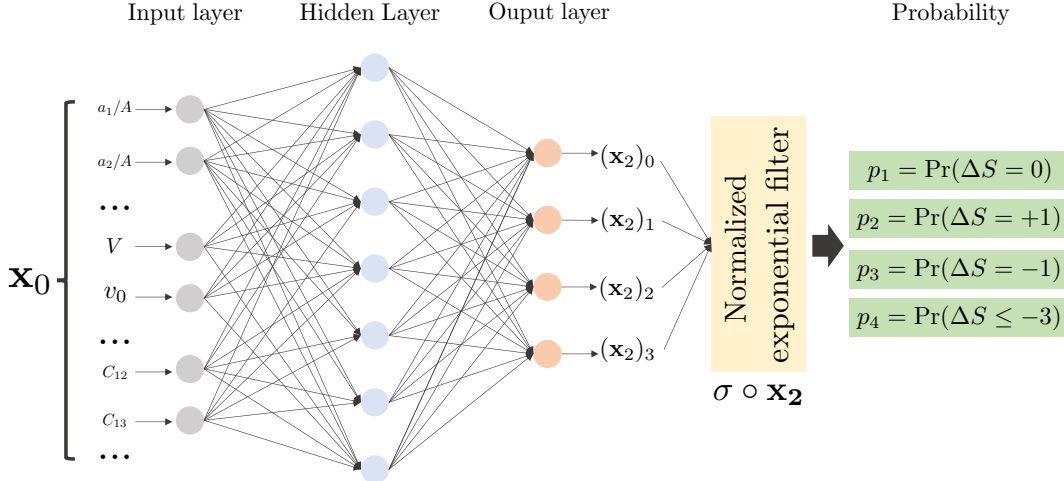
Figure 4.5: An illustration of a neural network with $0.5(S^2 + 3S) + 1$ inputs, one hidden layer, and a $h(= 4)$-dimensional output. Here, the output can be written as $\mathbf{x}_2 = \psi_2(W^2\psi_1(W^1\boldsymbol{x} + \mathbf{b}^1) + \mathbf{b}^2)$, where $\boldsymbol{x} = (a_1/A, a_2/A, ..., v, v_1, \ldots, C_{11}, C_{12}, \ldots) = \mathbf{x}_0$ is the input. W^1 is the matrix weights from the input layer to the hidden layer and W^2 is the matrix from the hidden to the output layer. $\mathbf{b}^1, \mathbf{b}^2$ are biases and ψ_1, ψ_2 are activation functions. The normalized exponential filter (4.9) normalizes $h-$dimensional vectors, resulting in a probability distribution consisting of h probabilities.

categorized as a *classification* problem.

In addition, we note that machine learning techniques [130–132] have recently been developed as more computationally tractable alternatives to phase field models. In such studies, grains are fully resolved and the training data constitute movies of evolving grains with no explicit input on physical laws. From this perspective, our use of machine learning is markedly different since the goal here is to arrive at a coarse-grained model. Moreover, the training of our neural network is facilitated by the von Neumann–Mullins-inspired choice of input variables, described in Section 4.3.4.

4.4.1   A deep learning approach

A deep neural network is a hierarchical model where each layer applies a linear transformation followed by a nonlinearity to the preceding layer [133]. For demonstration, consider a neural network consisting of k-layers, which takes $\mathbf{x}_0 \in \mathbb{R}^n$ as an input and outputs a h-dimensional vector $\mathbf{x}_k$. See Fig. 4.5 for an illustration of a neural network with $k = 2$ layers. We are using upright bold Roman letters to denote the inputs and outputs to the layers of a generic neural network. The zeroth layer is called the input layer, and the last layer is called the output layer. Other layers in between are called hidden layers. The input and output dimensions $d_1, \ldots, d_{k-1}$ of hidden layers are not necessarily monotonously increasing or decreasing. The operations occurring between the $j - 1$ and j-th layers are expressed as

$$\mathbf{x}_j = \psi_j(W^j\mathbf{x}_{j-1} + \mathbf{b}^j), \quad 1 \le j \le k,$$

where $W^j \in \mathbb{R}^{d_j \times d_{j-1}}$ is a linear transformation, $\mathbf{b}_j \in \mathbb{R}^{d_j}$ is a bias, and $\psi_j : \mathbb{R}^{d_j} \to \mathbb{R}^{d_j}$ is an element-wise non-linear activation function acting on each component of $(W^j\mathbf{x}_{j-1} + \mathbf{b}^j)$. The final output $\mathbf{x}_k$ of the neural

network, parametrized by the weights, is given by

$$\mathbf{x}_k(\mathbf{x}_0; \{W^j\}, \{\mathbf{b}^j\}) = \psi_k(W^k \psi_{k-1}(W^{k-1}...\psi_2(W^2 \psi_1(W^1 \mathbf{x}_0 + \mathbf{b}^1) + \mathbf{b}^2)... + \mathbf{b}^{k-1}) + \mathbf{b}^k). \tag{4.8}$$

The map $\mathbf{x}_k(\mathbf{x}_0; \{W^j\}, \{\mathbf{b}^j\})$ constitutes the neural network map.

Recalling the form of $\mathcal{F}_S$ in (4.7), we will now interpolate $\mathcal{F}_S$ using a deep neural network map with $n = 0.5(S^2 + 3S) + 1$, $h = 4$ and $\mathbf{x}_0 = \boldsymbol{x}$. To ensure that for each $\boldsymbol{x}$, $\mathcal{F}_s(\boldsymbol{x})$ is a probability distribution, we compose the neural network map $\mathbf{x}_k(\boldsymbol{x}; \{W^j\})$ with a normalized exponential filter $\boldsymbol{\sigma} : \mathbb{R}^4 \to [0,1]^4$, defined as

$$\sigma_i(\boldsymbol{z}) = \frac{e^{z_i}}{\sum_{j=1}^4 e^{z_j}}, \quad (i = 1, \ldots, 4) \tag{4.9}$$

and express $\mathcal{F}_S$ as a function parametrized by the weights:

$$\mathcal{F}_S(\boldsymbol{x}; \{W^j\}, \{\mathbf{b}^j\}) = \boldsymbol{\sigma} \circ \mathbf{x}_k. \tag{4.10}$$

$\mathcal{F}_S$ is now completely described by the weights and biases, which will be obtained by fitting $\mathcal{F}_S$ to training data collected from phase field simulations. In particular, as grains in a phase field simulation evolve, their coarse grain descriptors $\overline{\boldsymbol{x}}_i \in \mathbb{R}^n$ and corresponding topology changes $\overline{\boldsymbol{p}}_i \in [0,1]^4$ are recorded. We are using an overline to emphasize that the pair $(\overline{\boldsymbol{x}}_i, \overline{\boldsymbol{p}}_i)$ are training data. Due to the deterministic nature of the phase field simulation, $\overline{\boldsymbol{p}}_i$ has the form of a one-hot vector, which depends on the type of the event as follows:

$$\overline{\boldsymbol{p}}_i = \begin{cases} (1,0,0,0) & \text{if topology does not change,} \\ (0,1,0,0) & \text{if the number of edges increases by one,} \\ (0,0,1,0) & \text{if the number of edges decreases by one,} \\ (0,0,0,1) & \text{if the grain vanishes.} \end{cases} \tag{4.11}$$

Given m training data points $\{(\overline{\boldsymbol{x}}_i, \overline{\boldsymbol{p}}_i) : i = 1, \ldots, m\}$, we optimize the weights W^j and biases $\mathbf{b}^j$ by defining a negative log-likelihood loss function L as

$$L(W^1, \ldots, W^k, \mathbf{b}^1, \ldots, \mathbf{b}^k) = -\sum_{i=1}^m \text{diag}(w_1, \ldots, w_4)\overline{\boldsymbol{p}}_i \cdot \log \boldsymbol{p}_i, \tag{4.12}$$

where $\text{diag}(w_1, \ldots, w_4)$ is a 4×4 diagonal matrix formed by appropriate weights, and $\boldsymbol{p}_i = \mathcal{F}_S(\overline{\boldsymbol{x}}_i; \{W^j\}, \{\mathbf{b}^j\})$. The $\log \boldsymbol{p}_i$ in (4.12) is in $\mathbb{R}^4$, and it is defined component-wise as $(\log(\boldsymbol{p}_i))_l := \log((\boldsymbol{p}_i)_l)$,

The problem of learning network weights is then formulated by the following optimization problem:

$$\{W_1, \ldots, W_k, \mathbf{b}_1, \ldots, \mathbf{b}^k\} = \operatorname{argmin} L(\{W^j\}, \{\mathbf{b}^j\}) \tag{4.13}$$

A variety of computational techniques, including stochastic gradient decent and back-propagation [134–137], are available to solve (4.13). The main challenge here is that (4.13) is usually not a convex function of $\{W^j\}$ due to the product of the W^j variables and the nonlinearities ψ_k in (4.8). Furthermore, it is hard to justify whether the converging solution to (4.13) is the *global minima*. Therefore, we will need an appropriate procedure to validate the solution of the optimization problem.

(a) Initial condition
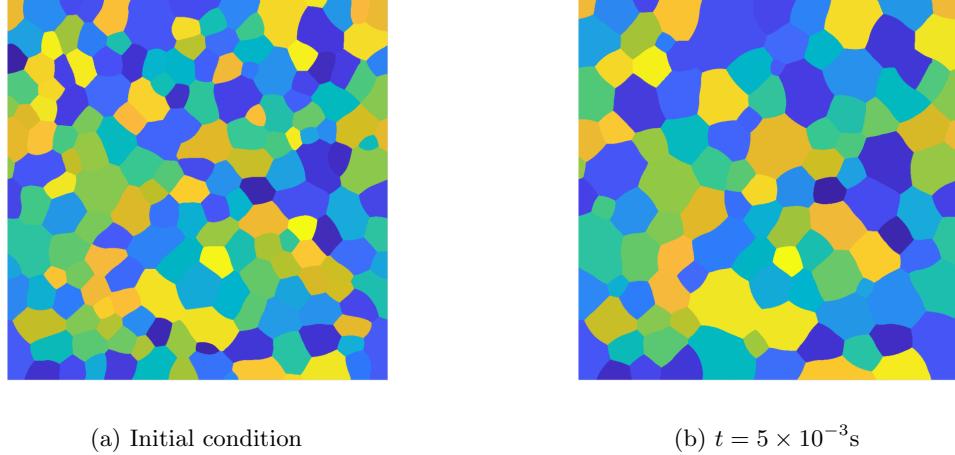
(b) $t = 5 \times 10^{-3}$s

Figure 4.6: Snapshots of isotropic grain growth using the KWC phase field simulation. Number of grains decreases and the average grain size increases.

4.4.2 Training data

To train parameters $\{W^j, \mathbf{b}^j\}$ of the neural network, we collected training data from the phase field grain growth simulations. In particular, we employed the generalized Kobayashi–Warren–Carter (KWC) model (2.7) developed in Chapter 2. The isotropic grain boundary energy is enabled by selecting a constant core energy function $\mathcal{J}(\llbracket \theta \rrbracket) = 0.5$. Note that this is disallowed in the original KWC model [20, 21], which is limited to Read–Shockley-type grain boundary energy.

To generate a training data set, we constructed 100 polycrystals, obtained as Voronoi tessellations of uniformly distributed random points, occupying the region $\Omega = [0, 1]^2$. The grain microstructure is described on a 2500×2500 regular grid. Each polycrystal consists of 200 grains, and a configuration is shown in Fig. 4.6a as an example. The thresholding algorithm developed in Chapter 3 is used to generate motion by curvature. The grain boundary length scale parameter ϵ is set to $\epsilon_1 = 0.006$. The form (3.8) results in a time-step $\Delta t_1 = 0.25\epsilon^2 = 9.0 \times 10^{-6}$t, while the reduced mobility $m\gamma = 1\mu m^2/s$ and the unit conversion factor $\mathsf{t} = 1s/\mu m^2$. We remind here that the length scale parameter ϵ also determines the minimum size of grains that can be resolved by the phase field method. If a grain shrinks to a size close to $O(\epsilon)$, it automatically vanishes at the end of the thresholding step.

A snapshot of an evolving microstructure in Fig. 4.6 shows that the average grain size increase while the number of grains in the system decreases. Fig. 4.7, which shows the rate of change of grain areas of different topologies and their standard deviations during the time interval $[2.5 \times 10^{-4}\mathsf{t}, 5.0 \times 10^{-4}\mathsf{t}]$, confirms that the von Neumann–Mullins law is statistically satisfied. The variance in Fig. 4.7 originates from the transient perturbations from $120°$ that some vertex angles experience when topology changes occur in the neighboring grains [105].

The raw data from a phase field simulation is in the form of a time-series of grain labels (or grain indices) defined on the discrete grid. To train the neural network, it is required to post-process the simulation data to obtain the coarse-grained descriptors — area, side and the indices of the neighbors of each grain. The post-processing is done as follows. First, the area of each grain is estimated by counting the number of the grid point occupied by each grain. Second, the topological state of a grain is evaluated by counting the
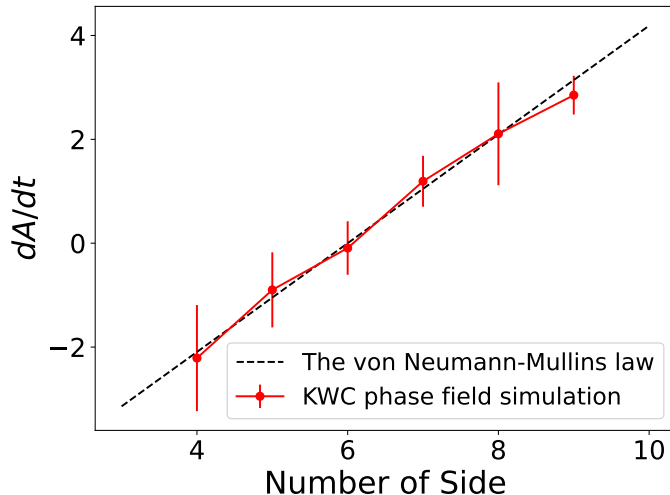
Figure 4.7: Confirmation of the von Neumann–Mullins law during isotropic grain growth simulation of the KWC model (2.7) using the thresholding method.

number of distinct neighbors.[4] Third, the neighborhood of a grain is conveyed using an adjacency matrix $\boldsymbol{M}$ of size 200×200, where 200 is the initial number of grains. The number of sides of i-th grain is identified as the sum of the non-zero elements in the i-th row of $\boldsymbol{M}$. The indices of the neighboring grains are the column indices of the non-zero elements of the i-th row $\boldsymbol{M}$. Finally, the resulting coarse-grain descriptors are further processed and collected as an array $\overline{\boldsymbol{x}}(t) = (a_1/A, a_2/A, ..., V, v_1, ..., C_{11}, C_{12}, ...)$, where all variables appearing on the right are time-dependent. In addition, topology changes are recorded in a time-dependent one-hot vector $\overline{\boldsymbol{p}}$ described in (4.11). The data preprocessing is summarized graphically in Fig. 4.8.

Each phase field simulation proceeded 200-time steps from the initial configuration, and yielded approximately 150 critical events. Fig. 4.9 shows the evolution of the topologies of three grains and their normalized areas. The red plot in Fig. 4.9a shows an initially five-sided grain lose a side at the 25th timestep, and disappear at the 77th timestep. The blue plot shows the variation of the normalized area. Fig. 4.9b shows an initially seven-sided grain continuously growing as its topology changes from seven- to eight-sided and back to seven-sided. On the other hand, Fig. 4.9c shows the area of an initially growing grain stabilizing after it transforms to a hexagon. Since the grain growth rate is discontinuous at instances when topologies change, the slopes of the blue plots are expectedly discontinuous. However, although the variation of area has to be continuous, we record discontinuities as seen in Fig. 4.9. This is a consequence of the limited resolution of shrinking grains when their size is below a critical size that is determined by ϵ. In intervals around the discontinuities, either the central grain or one of its neighbor is shrinking. Since the instances when they vanish cannot be precisely identified, discontinuities appear in the blue plots. Moreover, when the central grain is shrinking, the discontinuity is more pronounced (75th timestep in Fig. 4.9a) compared to when a neighboring grain is shrinking. While decreasing ϵ will attenuate the discontinuities of Fig. 4.9, they cannot be completely removed since the growth rate converges to $-\infty$ as the grain size tends to zero.

It is important to note that critical events are rare. For example, Fig. 4.9a shows that there are only two critical events corresponding to one-hot vectors $(0, 0, 1, 0)$ and $(0, 0, 0, 1)$. In all other time instances, the

---

[4]This may not be true in some exceptional cases, wherein a pair of neighboring grains share multiple edges. However, such cases are rare in our simulations.
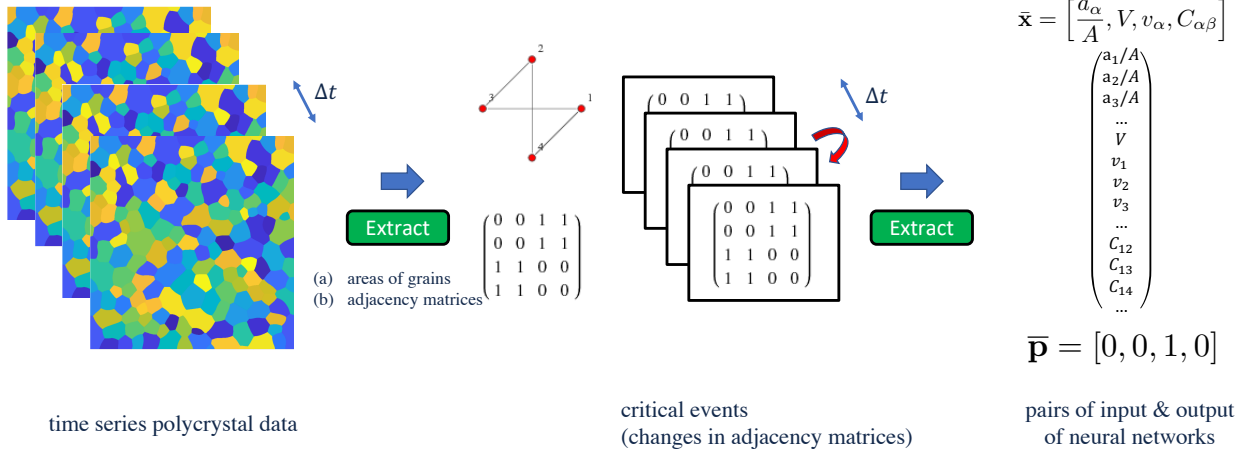
Figure 4.8: A schematic representation of raw data processing for collecting training data for the TTM.
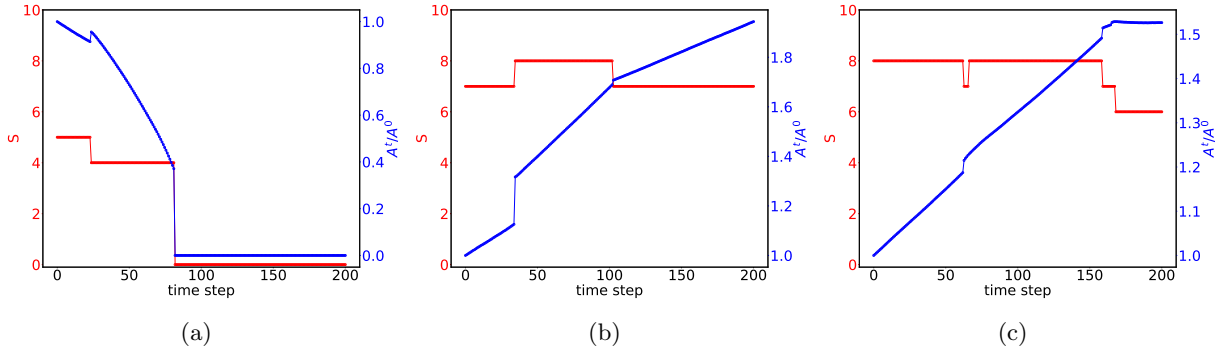

Figure 4.9: Time histories of areas and topologies of three grains showing topology transformations.

topology does not change resulting in $\overline{\boldsymbol{p}} = (1, 0, 0, 0)$. Therefore, the one-hot vectors collected as training data are highly *imbalanced*. Such an imbalance in data may cause severe challenges to training algorithms for solving (4.13) [138]. To address this, we randomly under-sampled data corresponding to the case when there is no topology change $\overline{\boldsymbol{p}} = (1, 0, 0, 0)$, and ensured that the ratio of its occurrence relative to the other three cases is 4:1.

4.4.3   Training of neural network functions

We implemented a standard deep learning framework to solve the optimization problem (4.13) using the Pytorch library [139], a python-based open source machine learning framework. Recall that we would like to construct $\mathcal{F}_S$, and the number of inputs, $n = 0.5(S^2 + 3S) + 1$, depends on the grain topology S. Thus, we built seven separate neural networks, one for each grain topology, ranging from 3- to 9-sided grains. Since grains with two sides and more than nine sides are rarely observed during isotropic grain growth ($< 0.05\%$), we assume that their effect on the overall grain statistics is negligible. We selected fully-connected networks (4.8) as the neural network architecture. A rectified linear unit, or ReLU [140]

$$\psi(x) = \max\{0, x\}$$

41

Topology S	Number of inputs n	Number of data m	Number of neural network parameters	Number of layers k	Training accuracy (%)
3	10	948	428	5	91.0
4	15	9738	2000	5	94.7
5	21	16854	6500	4	91.1
6	28	30620	4713	5	91.2
7	36	23800	4023	4	91.8
8	45	10560	4425	4	90.8
9	55	2270	1423	5	94.1

Table 4.1: A summary of neural networks and their training accuracy.

is used for all the nonlinear activation functions ψ_j. The weight of each event $\{w_j\}$ in the loss function L (4.12) is set to the inverse of the total number of events in the collected training data.

Adams optimization with AMSGrad [141, 142] is implemented to solve (4.13). The convergence rate of the training process can be affected by several algorithmic parameters, typically including batch size, epochs, and shuffle. Batch-size controls the number of samples from a dataset used to evaluate one gradient update; a batch size of 1 is associated with a full stochastic gradient descent optimization. One epoch is one round of training on a dataset. It is common to re-shuffle a dataset many times and perform the back-propagation updates because data shuffling for each epoch would result in an updated parameter set $\{W^j\}, \{\mathbf{b}^j\}$. We set the batch size as 1,500, and each neural network model is trained using 17,000 epochs. Decreasing loss curves (4.12) as a function of the epoch during the training of the networks corresponding to five-, six-, and seven-sided grain are shown in Fig. 4.10. At the end of training process, oscillations in loss function at each epoch is more prominent, while the improvement in loss function is marginal.

After the completion of the training process, we can use the expression for $\mathcal{F}_S$ in (4.10) to evaluate the probability of topology transformation of a grain based on its state and the states of its neighbors, described by its input $\boldsymbol{x}$. The input may or may not be in the training data set. The probability $\boldsymbol{p}$ outputted by the TTM is typically not a one-hot vector unlike those in the training data set. The realization of an event is determined by first thresholding the output $\boldsymbol{p}$ to a one-hot vector as

$$p_i = \begin{cases} 1 & \text{if } p_i = \max(p_1, \ldots, p_4) \\ 0 & \text{otherwise,} \end{cases} \tag{4.14}$$

and choosing the event corresponding to it from (4.11).

We can evaluate the training accuracy, or *fitting accuracy*, by comparing the realization predicted by the TTM with the training data. We evaluate the training accuracy in terms of realizations. The accuracy measured by the ratio of the number of correct answers to the total data is summarized in Table 4.1. The training accuracies of the neural networks are over 90 %. The *validation accuracy* of a neural network can also be evaluated using a validation dataset that was not used for training. Such a validation study is important to assess the transferability of the network. However, since the TTM is a coarse-scale model that outputs probabilities, such a validation study should involve a statistical comparison. Therefore, we proceed to MC simulation, where we evolve grain statistics using the probabilities outputted by the TTM. This will enable statistical validation of our model.
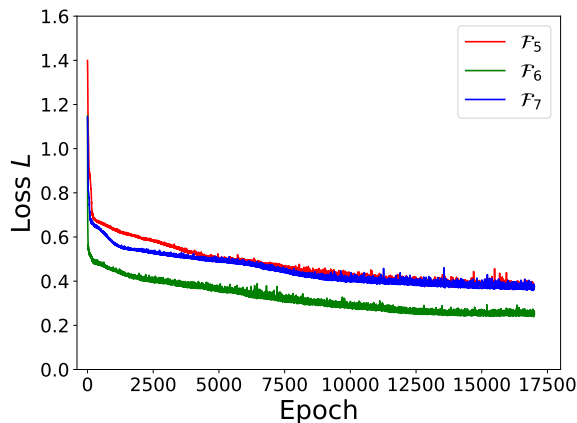
Figure 4.10: Examples of loss curves (4.12) as a function of the number of epochs for the 5-, 6- and 7-sided grain neural networks.

4.5 The Monte Carlo (MC) simulation for evolving grain statistics

In this section, we present a MC implementation of the stochastic framework described in Section 4.3.1, wherein we use trained neural networks (from Section 4.4) to statistically evolve the side and area distributions during grain growth and validate the framework. We remind that the input to the framework is a joint probability distribution $F(A, S, t = 0)$ of grain area and number of sides, and the output is its time evolution $F(A, S, t)$. The outline of the MC simulation, which is initially introduced in Section 4.3.1, is re-briefed using a schematic in Fig. 4.11.

4.5.1 Algorithm

The MC algorithm begins with initializing states (A_i, S_i) of N rep grains sampled from the initial distribution $F(A, S, t = 0)$. The states of all the rep grains are stored in two N-sized one-dimensional arrays $\boldsymbol{A}$ and $\boldsymbol{S}$. The strategy of the MC simulation is to evolve the states $(A_i(t), S_i(t))$ using the von Neumann–Mullins law and the TTM to deduce $F(A, S, t)$.

We will now describe the steps to evolve the states of the rep grains. First, we construct the neighbors of each rep grain by drawing them from the current distribution of the rep grains.[5] We store the neighbors of the rep grains in an *adjacency list* $\boldsymbol{D}$, a $N \times 9$ sized matrix, where 9 is the possible maximum number of neighbors in the framework.

The first S_i entries in the i-th row $\boldsymbol{d}_i$ of $\boldsymbol{D}$ are the labels of the neighbors of the i-th grain. Moreover, the order of the entries in a row conveys the connectivity between the neighbors — the neighbor grain $(\boldsymbol{d}_i)_1$ is connected to the neighbor $(\boldsymbol{d}_i)_2$, which is also connected to $(\boldsymbol{d}_i)_3$, and so on. The last neighbor $(\boldsymbol{d}_i)_{S_i}$ is connected to $(\boldsymbol{d}_i)_1$. At $t = 0$, the adjacency list is populated by drawing the neighbors of the rep grains from $F(A, S, 0)$. Here, we emphasize that although neighbors are drawn from the distribution of the rep grains, they are *not* rep grains. This implies that even if j-th grain is in the neighborhood of an i-th rep grain, the i-th grain is not necessarily in the neighborhood of the j-th rep grain. We can form the inputs $\boldsymbol{x}_i = (a_1/A_i, \ldots, a_{S_i}/A_i, V_i, v_1, \ldots, v_{S_i}, C)$ to the TTM at any time using the matrices $\boldsymbol{A}, \boldsymbol{S}$ and $\boldsymbol{D}$.

---

[5]From Section 4.3.1, recall that our system is assumed to be spatially homogeneous, which enables us to introduce the notion of representative grains and their distribution, and use the same distribution for the neighbors of each rep grain.
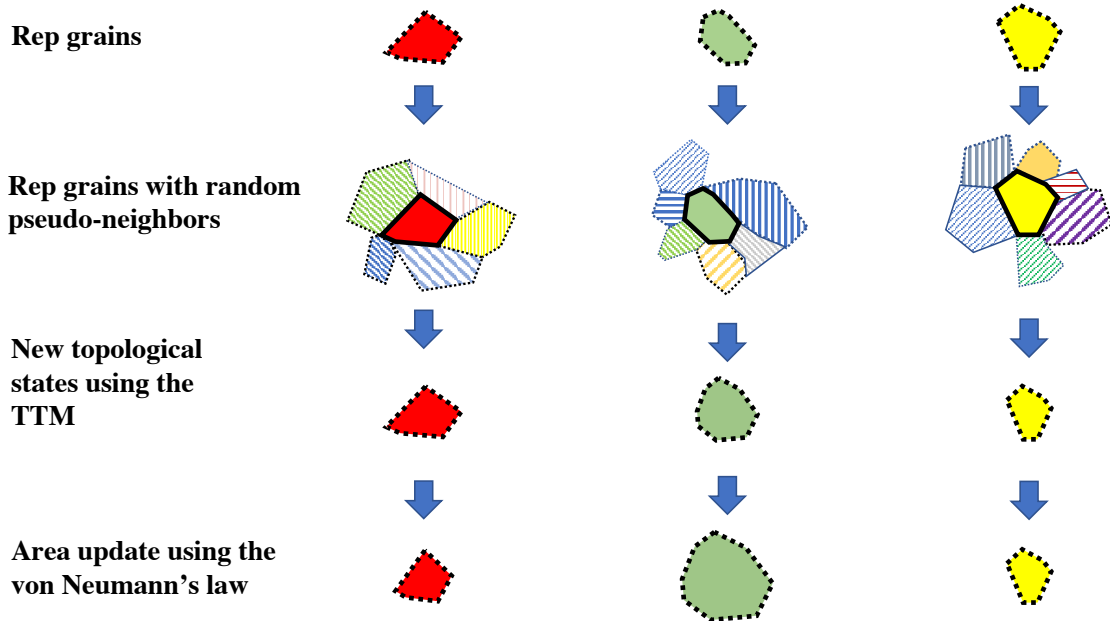
43

Figure 4.11: A schematic description of the Monte Carlo simulation using rep grains, introduced in Section 4.3.1.

For a given time step size Δt, the topologies of rep grains are updated using the TTM by thresholding the probabilities $\mathcal{F}_{S_i}(\boldsymbol{x}_i)$ using (4.14).[6] Since we assumed that the influence of grains with sides less than three and greater than nine is negligible, the probabilities of losing an edge in $\mathcal{F}_{S_3}$ and gaining an edge in $\mathcal{F}_{S_9}$ are set to zero. If i-th rep grain gains a side, we add a new random grain to $\boldsymbol{d}_i$ by sampling the current distribution. If the rep grain loses a side, we delete the neighbor which has the lowest v_α from $\boldsymbol{d}_i$. This is because the negative v_α with the largest magnitude indicates a vanishing grain, which is also most likely to lose a side. On the other hand, if the rep grain disappears, we delete it and all the entries of $\boldsymbol{d}_i$. Clearly, the number of rep grains would decrease if we do not compensate for their loss. Since rep grains constitute a statistical representation of the grain microstructure, we would like to conserve their number. Therefore, when a rep grain disappears, we add a new random grain that is sampled from the current distribution. Using the updated topologies $S_i(\Delta t)$, we update the areas of the rep grains using the von Neumann–Mullins law (4.1) to obtain $A_i(\Delta t)$. Grains may also disappear if their areas turn negative. [7] In this manner, the states of the rep grains are evolved until a desired time.

The algorithm to evolve grain statistics is summarized in Algorithm 2.

4.5.2   Results

The goal of this section is to 1) examine the asymptotic grain state distribution predicted by our stochastic framework, 2) assess the stability of the asymptotic distribution with respect to the initial conditions, and 3) validate the stochastic framework by comparing to phase field simulations.

---

[6]The probabilities outputted by $\mathcal{F}_{S_i}$ may be used as is within our MC implementation. Instead, we opted to threshold them as this choice resulted in the correct asymptotic side distribution.

[7]A majority of grain vanishing events are attributed to the TTM. This is because, as soon as the grain size becomes smaller than the smallest size that can be resolved by the phase field model, the TTM marks the grain to vanish. Then, we process $\boldsymbol{d}_i$ as previously stated. Because area and side states of a virtual neighbor grain are synchronized with the rep grain that shares the same index, the states of virtual neighbors are also updated when the TTM is invoked on all the rep grains.

Algorithm 2 OpenGBStat: An algorithm to evolve a joint distribution of grain areas and topologies

1: Input: a) Initial grain statistics $F(A, S, t = 0)$; b) trained TTMs $\mathcal{F}_1, \ldots, \mathcal{F}_9$ for topology transformation probabilities; c) time step size Δt; d) final time T; and e) number of rep grains N.
2: Initialize the random states (A_i, S_i) $(i = 1, \ldots, N)$ of N rep grains using $F(A, S, t = 0)$
3: **for** $(i = 0$ to N$)$ **do**
4:     Construct the states $\{(a_{\alpha i}, s_{\alpha i}) : \alpha = 1, \ldots, S_i\}$ of the neighbors of grain i using the initial distribution $F(A, S, 0)$
5:     Form the adjacency list $\boldsymbol{D}$.   ▷ Initialize neighbor information.
6: **end for**
7: t=0
8: **while** (t $\leq$ T) **do**
9:     $i = 1$
10:    **while** $(i \leq N)$ **do**
11:        Let $A = A_i$, $S = S_i$, and $\alpha = 1, \ldots, S_i$
12:        Form the adjacency matrix $\boldsymbol{C}$ from the i-th row of $\boldsymbol{D}$
13:        Calculate v_α and V using (4.5) and (4.6), respectively
14:        Let $\boldsymbol{x} = (a_1/A, \ldots, a_S/A, V, v_1, \ldots, v_S, \boldsymbol{C})$
15:        $\boldsymbol{p} = \mathcal{F}_S(\boldsymbol{x})$
16:        **if** $S_i = 3$ **then**   ▷ to guarantee the possible range for side numbers from 3 to 9.
17:            $p(\Delta S = -1) = 0$
18:        **else if** $(S_i = 9)$ **then**
19:            $p(\Delta S = +1) = 0$
20:        **end if**
21:        Threshold $\boldsymbol{p}$ according to (4.14) to obtain the topology change ΔS
22:        **if** $(\Delta S = 0)$ **then**
23:            continue
24:        **else if** $(\Delta S = 1)$ **then**
25:            Add a new random labels to $\boldsymbol{d}_i$
26:        **else if** $(\Delta S = -1)$ **then**
27:            Delete one neighbor grain from $\boldsymbol{d}_i$ that has minimum v_α
28:        **else if** $(\Delta S \leq -3)$ **then**
29:            Delete the i-th rep grain and $\boldsymbol{d}_i$. Generate a new random rep grain using $F(A, S, t)$.
30:            Construct the random neighbors to $\boldsymbol{d}_i$.
31:        **end if**
32:        $S_i \leftarrow S_i + \Delta S$
33:        $A_i \leftarrow A_i + (\pi/3)(S_i - 6)\Delta t$
34:        **if** $(A_i \leq 0)$ **then**
35:            Delete the i-th rep grain and $\boldsymbol{d}_i$. Generate a new random rep grain using $F(A, S, t)$.
36:            Construct the random neighbors to $\boldsymbol{d}_i$.
37:        **end if**
38:        $i \leftarrow i + 1$
39:    **end while**
40:    $t \leftarrow t + \Delta t$
41:    Calculate $F(A, S, t)$ from the current rep grain states $\{(A_i, S_i) : i = 1, \ldots, N\}$
42: **end while**
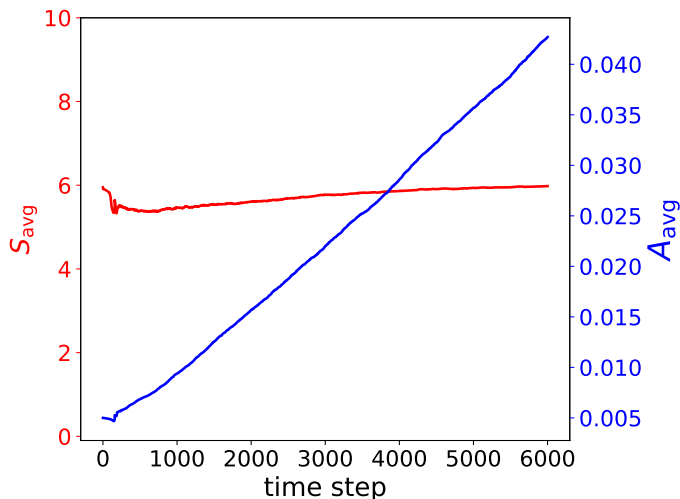43: Output: $\{F(A, S, t) : 0 \leq t \leq T\}$

Figure 4.12: Evolution of the average grain side and area during the MC simulation.

For our first goal, we considered an initial distribution $F(A, S, 0)$ of rep grains that is "far" from the asymptotic distributions of isotropic grain growth commonly reported in the literature [101, 104, 147]. The dependence of initial F on S was assumed to be a uniformly distributed from 3 to 9 sides. On the other hand, its dependence on A was assumed to be a Dirac delta distribution centered at $A = A_{\mathrm{avg}}$, where $A_{\mathrm{avg}} = 0.005$ is the initial average grain area in the training data obtained from a phase field simulation of 200 grains in the domain $\Omega = [0, 1]^2$. In other words, the initial areas of all rep grains are all equal to 0.005. We note here that such an initial distribution is *unrealistic*. In general, the grain side distribution is highly constrained due to the condition that a grain configuration must fill the entire space without any hole. Such a geometric constraint is satisfied in phase field simulations as the grain microstructures are fully resolved. However, these constraints do not arise in our stochastic framework as it does not require constructing grain microstructures.

In the MC simulation, we start with $N = 5{,}000$ rep grains and use a timestep size $\Delta t_M = 9 \times 10^{-6} \mathsf{t}$, which is equal to the value used in the thresholding algorithm to obtain the training data. Fig. 4.12 shows the histories of the averages of the number of sides and areas of the rep grains. From the plot it is clear that the average area grows linearly, while the average number of sides converges to 6. Fig. 4.13 shows the evolution of the side and area distributions recorded in the MC simulation. The plots demonstrate that the distributions reach an asymptotic state at around 5,500 timesteps, when the statistics of the two state descriptors do not change with time. The simulation time to attain asymptotic statistics using a single-core machine was 2 hours. Moreover, one of the fundamental assumptions of the current framework, that rep grains do not interact with each other, guarantees straightforward parallelization of Algorithm 2, allowing more room for further speed up.

Moving to our next goal, we explore the sensitivity of the asymptotic distributions to the choice of initial side distributions. Again, these initial distributions are only possible because the MC simulation do not construct actual microstructure. Fig. 4.14 shows that four distinct initial distributions evolve to almost identical late stage self similar distributions. The results confirm that the asymptotic grain statistics are robust and largely independent of initial conditions.

In our third goal we validate the results of the MC simulation by comparing to statistics observed in a

46

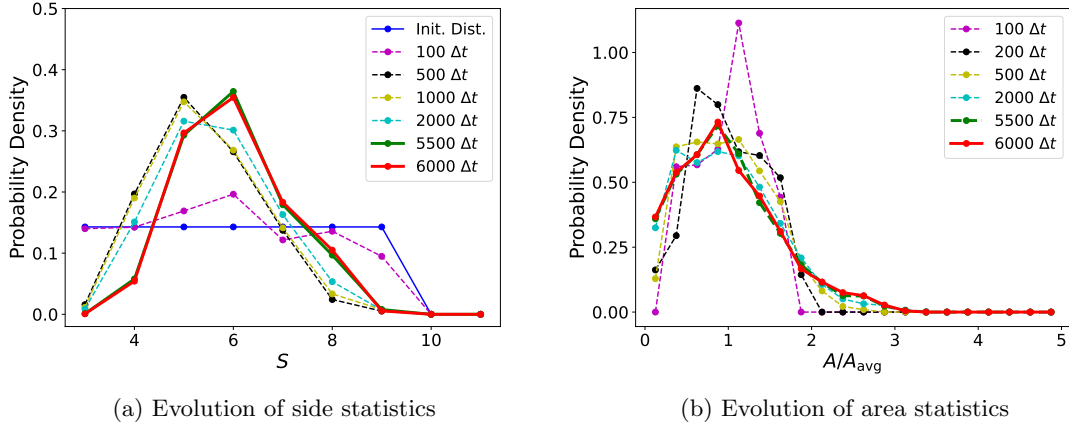(a) Evolution of side statistics   (b) Evolution of area statistics

Figure 4.13: The evolution of grain statistics predicted by the MC simulation. At approximately 5,500 time steps, the distributions for grain sides and areas arrive at an asymptotic state.

Dist. Curve	Expectation	Standard Dev.	Skewness
Current Work	5.992	1.091	0.276
Phase Field I.C.	5.995	1.316	0.353
Phase Field Later	5.992	1.088	0.465
Ref. [143]	5.993	1.276	0.476

Table 4.2: Quantitative comparisons of the asymptotic side distributions from different methods

Dist. Curve	Expectation	Standard Dev.	Skewness
Current Work	0.238	0.466	3.231
Phase Field	0.239	0.448	3.087
Ref. [143]	0.388	0.510	2.518

Table 4.3: Quantitative comparisons of the asymptotic area distributions from different methods

KWC phase field simulation of $3,000$ initial grains. The grain microstructure is described using a 9999×9999 grid. We fix the grain boundary length scale parameter $\epsilon_2 = 0.0012$ in the KWC energy density, defined in (2.7). The resulting time-step size of the large scale phase field simulation is $\Delta t_2 = 3.6 \times 10^{-7}$t [22]. The initial configuration of the KWC phase field simulation was generated using a Voronoi tessellation of uniformly distributed random seeds. The side distribution corresponding to the initial configuration is shown as a blue dashed line in Fig. 4.15a. The initial side distribution peaks at $S = 6$, which is a known property of a Voronoi tessellation [148]. The phase field simulation was run until half of the initial grains remain. The computational bottleneck of the KWC phase field numerical solver is the Fast Fourier Transform (FFT) on the discrete grid [22]. Despite the parallelization of the FFT on 20 cores, it took approximately 72 hours to obtain the self-similar asymptotic grain statistics from the KWC phase field simulation.

Fig. 4.15 compares the asymptotic side and area distributions observed in the KWC phase field simulation with those predicted by the Monte Carlo simulation, and demonstrates that they are in good agreement. Results from other simulation methods [101, 104, 147] are also plotted for reference. Learning from the KWC phase field simulation training data, the asymptotic statistics of the MC simulation is closer to the result of phase field simulation than the results from the other simulations. Grain statistics are also quantitatively
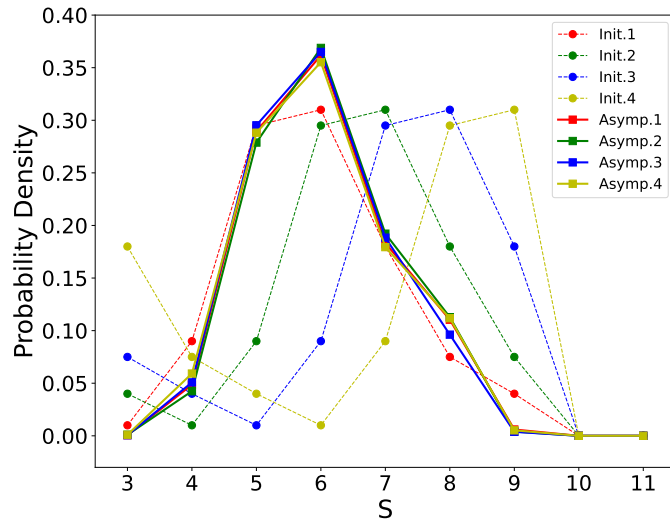
Figure 4.14: Asymptotic distributions for number of sides resulting from the MC simulation with different initial distributions of rep grains. The asymptotic distributions converge suggesting that they are independent of the choice of the initial distribution.
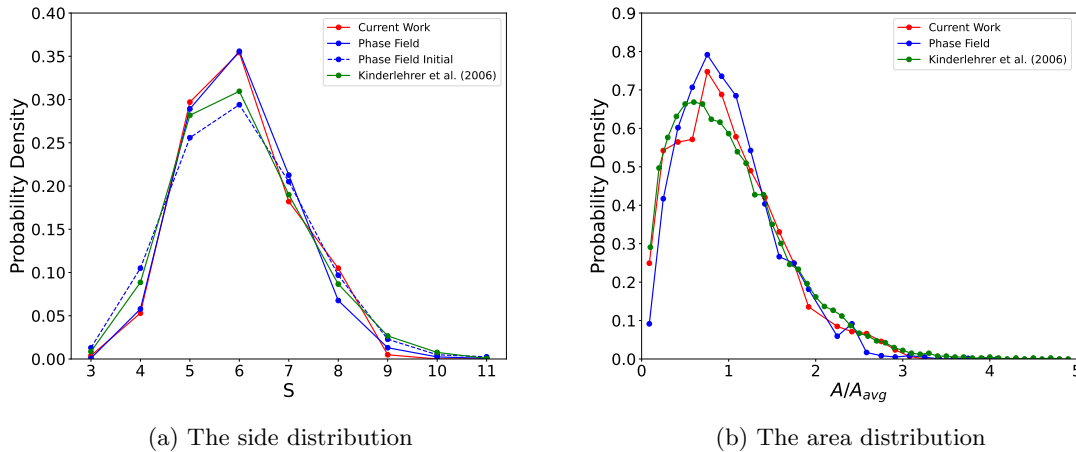

(a) The side distribution

(b) The area distribution

Figure 4.15: Comparisons of the asymptotic distributions for number of sides and areas of grains from different methods [22, 143]. The results from the current stochastic framework are in good agreement with the phase field simulation.
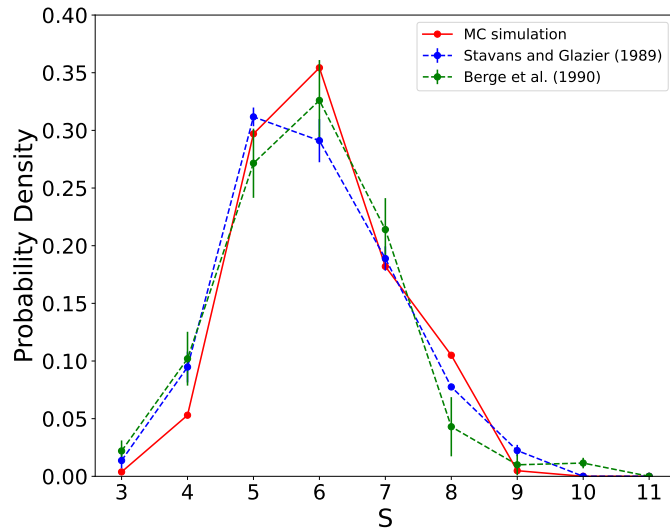
Figure 4.16: Comparison of asymptotic side distribution to experimental results [144, 145] of gas bubbles and soap froths. Little disagreements between experiments and simulation are attributed to the finite size of experimental samples [146].

(a) Monte Carlo simulation

(b) Phase field simulation
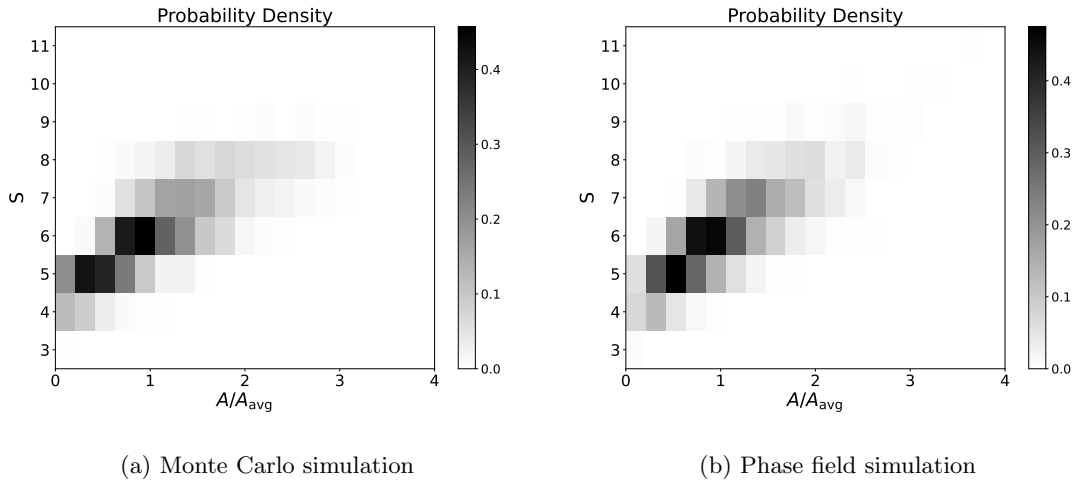
Figure 4.17: The joint probability density function of the number of sides and areas at asymptotic states confirms positive correlation between the two descriptors.
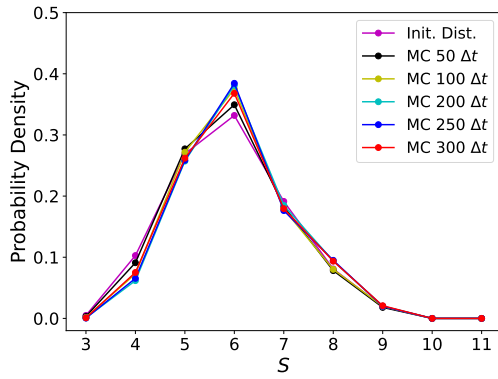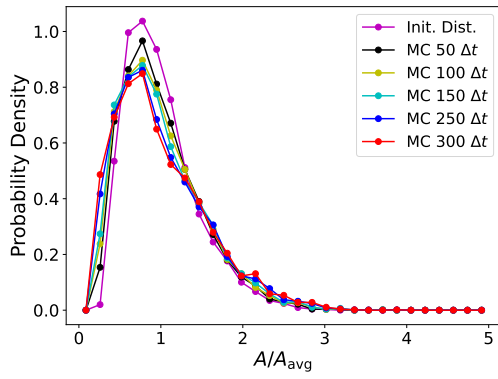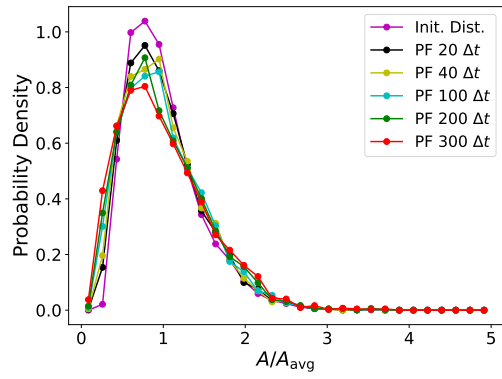
(a) Transient side distribution in MC simulation
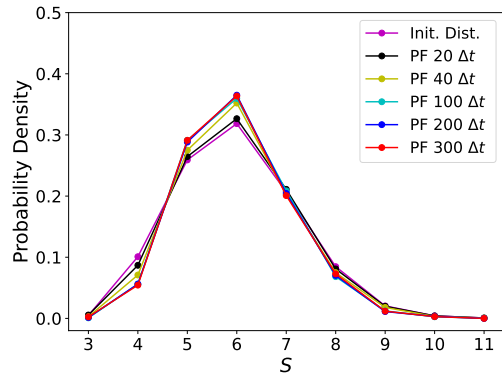
(b) Transient side distribution in PF simulation

(c) Transient area distribution in MC simulation

(d) Transient area distribution in PF simulation

Figure 4.18: A comparison of transient grain statistics obtained in the MC and phase field simulations.

compared in Table 4.2 and 4.3 using several characteristic metrics of distributions: expectation, standard deviation, and skewness. The expectations $\langle S \rangle$ of grain topology from all methods, are close to 6. The value is related to the Euler's characteristic equation, which is an essential geometric condition for polygons filing the space [45]. The standard deviation of the asymptotic side distribution from the MC simulation is also close to that of the late-stage phase field simulation. All curves have positive skew values, suggesting longer tails on the right side from the average value, i.e., $S > 6$. The quantitative comparisons of area distributions confirm the similarity between distributions of the MC simulation and the late-stage phase field simulation.

In Fig. 4.16, the asymptotic grain side distribution from the MC simulation is also compared with experimental data marked with uncertainties in the measurement. Here, the experimental results are obtained from observations of gas bubbles and soap froths [144, 145]. Note that in these systems, the assumption of isotropic surface tension and mobility is more valid than actual grain growth which entails anisotropic nature of surfaces. While the result from the MC simulation matches the overall shape of experimental results, there still exists a minute discrepancy as well. In particular, the observation from Glazier *et al.* [145] shows a peak value of S at 5 not in 6. This is attributed to the finite size of samples [146].

In Fig. 4.17, we plot the joint distribution (Fig. 4.17) of A and S from the MC and phase field simulation, which are also in good agreement. The results demonstrate a positive correlation between the number of sides and areas, a feature that is not shared by the chosen initial distributions in the MC simulation. This confirms the Lewis' empirical law [149, 150], which states that the average grain area and the average number of grain sides are proportional in two-dimensional cellular structures.

Lastly, we compare the transient grain statistics from two simulations in Fig. 4.18. In this test, the initial grain statistics of the MC simulation is set to that of the initial configuration used in the large-scale phase field simulation. The time step size of the MC simulation $\Delta t_M = 3.6 \times 10^{-7}$ is also set to that of the large-scale phase field simulation Δt_2, which is 25 times smaller than the value $\Delta t_1 (= 9.10 \times 10^{-6} \mathrm{t})$ used for generating training dataset for the neural network functions of the TTM. This enables us to check the scale-invariance of the TTM as we intended in the model construction in the form (4.5) and (4.6). In both methods, as the side distributions evolve, the fraction of 6-sided grains increases mostly at the expense of the fraction of 4-sided grains (see Fig. 4.18a and Fig. 4.18b). However, there exists some mismatch between two methods as well. The result from the MC simulation shows an overshoot in the fraction of 6-sided grains, before it arrives at an asymptotic state. The mismatch is attributed to the lack of geometrical constraints in the MC simulation. However, the overall transient area distributions in both schemes also remain similar. The area distributions evolve to decrease the level of size homogeneity (see Fig. 4.18c and Fig. 4.18d).

From the above results, we conclude that the MC simulation is able to predict the transient and the asymptotic grain statistics of the two coarse descriptors with a significantly reduced computational time. Of course, this does not mean that the current stochastic framework can be regarded as a complete replacement of phase field models. As a higher-order model, phase field simulations can also readily predict richer physics: microstructure evolution beyond isotropic grain growth as well as statistics of other grain state descriptors. In general, the value of a lower model depends on the quantity of interest. If fast predictions on grain statistics of side and areas are only primary interest, the current framework outperforms the phase field approach.

4.6 Discussion and future work

In this section, we highlight an important feature of the suggested framework in more detail and discuss potential research directions for future work.
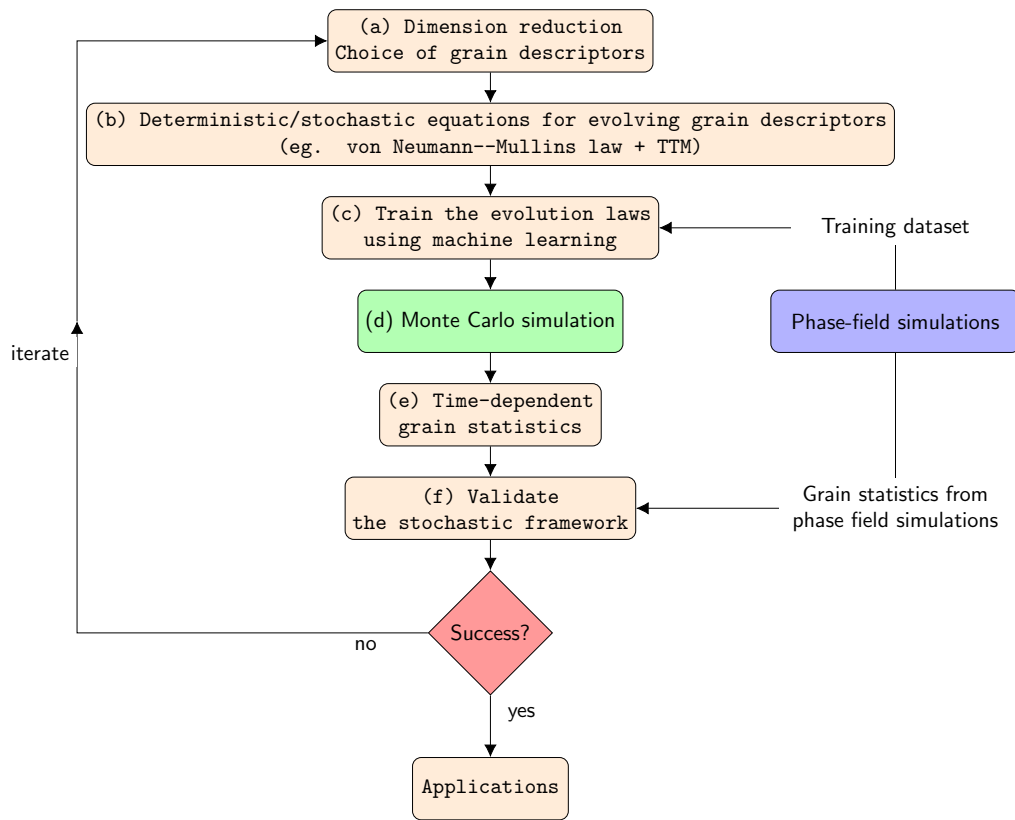
Figure 4.19: A generalized workflow of ML-informed paradigm to develop a stochastic framework.

We note a distinguishing feature of the suggested framework is that the areas and topologies are not subject to any geometrical constraints that ensure the space is always filled, as opposed to conventional simulation methods that fully resolve the grain microstructure. It is generally known that geometric constraints are also important constraints of grain growth as well as thermodynamics, because grains must completely fill space [151–153]. In phase field models, the space-filling constraint manifests in the form of restrictions on the joint distributions of areas and number of sides. However, the TTM is a local model that considers local connectivity as opposed to global connectivity, and the stochastic framework does not require the rep-grains to fill space. Nevertheless, it is interesting that the current stochastic framework arrives at asymptotic distributions of A and S that are similar to those observed in phase field simulations. This observation implies that despite the coarse-graining, geometric constraints are baked in to the TTM to an extent that their effect on the asymptotic distributions is preserved.

Concluding this chapter, we summarize the workflow of our machine-learning (ML) informed modeling paradigm in Fig. 4.19. It involves the following key steps — a) dimension reduction, b) a deterministic and/or probabilistic evolution laws, and c) Monte Carlo simulation. A reduced description of the grain microstructure using areas and topologies constituted step (a). The von Neumann–Mullins law and the TTM were introduced in step (b) to evolve the grain descriptors. The computational efficiency of our stochastic framework in predicting grain microstructure evolution motivates us to generalize the framework to anisotropic grain growth and three dimensions. In particular, we identify the following research directions for future work.

- We anticipate that our framework can be immediately extended to 3D isotropic grain growth. While the rate of change of volume of a 3D grain is not entirely a topological property according the 3D von Neumann–Mullins law [111], we may alternately employ a statistical von Neumann–Mullins law [112, 113] to obtain an expression in terms of the number of faces of a grain.

- For grain growth under anisotropic energies, the grain area and topology are not sufficient descriptors to develop a coarse-graining framework. This is because the von Neumann–Mullins law needs to be modified as the sum of all the internal angles at the vertexes of each grain, which are no longer $120°$. In this case, the orientation of each grain should be considered as an additional state descriptor. Using the force equilibrium at triple junctions, we can determine the internal angels of grain vertexes. Then, we may consider the above generalized von Neumanns' law, to evolve the area states.

- Finally, we also envision an automated process of identifying the key descriptors for a coarse-graining framework for three-dimensional anisotropic grain growth. For instance, from the above example, it is not clear whether only the grain areas, topologies, and orientations are sufficient descriptors for constructing a statistical model for general microstructure evolution. It is plausible that we may also need to consider descriptors such as grain perimeters and aspect ratios. Consequently, an interesting question arises — how do we know which are the significant grain state-descriptors that determine its evolution? We expect that a number of tools from data analytics offer promising routes to explore the above question.

Overall, the generalized workflow of ML-informed microstructure evolution paradigm rely on appropriate choices for dimension reduction and stochastic modeling for evolution equations. While an immediate benefit from such a coarse-grained framework is in their capability of accelerating predictive computations in support of material design, we can certainly find additional values in our approach beyond a practical engineering perspective.

First, we believe that ideas employed here can impact wider areas that share some common features. For illustration, while mean curvature flow was originally proposed as a model for the formation of grain boundaries in the annealing of pure metal, remarkably similar rules are found in various physical phenomena, in evolution of soap films, growth of some biological tissues [154], and engineering process of digital images [155]. On the other hand, we have also seen that how the models of Fradkov [121] utilizes the analogy of random collision in gas dynamics to establish the rule of grain topology transformations. Likewise, these fields learn new ideas from the other and develop further by adapting them in their own contexts.

Moreover, our approach suggests an alternative way to take advantage of the emerging machine-learning techniques to impact classical mechanics. While machine-learning algorithms have been applied to facilitate and automate the dimension reduction of a physical system, a blind use of these black box algorithms may get rid of opportunity to discover important insights and universal laws that could have been found in physics-based reduced-order models. However, recall that our approach requires a dimension reduction based on a reasonable hypothesis (e.g., the von Neumann–Mullins law of its neighbors), which would be tested through following validation processes. If the framework fails the task, one needs to iterate and construct a new hypothesis. All of these processes certainly belong to *the general scientific method*.

Chapter 5

Thesis summary

Recent additive manufacturing technology can strategically transform material microstructures, even at lab scales, using sophisticatedly-controlled thermo-mechanical loads. However, exploring the enormous process-microstructure space via experiments alone is expensive and time-consuming. Advanced manufacturing techniques may benefit from a faster computational infrastructure, which can rapidly simulate the relevant thermo-mechanical treatments. In this regard, the aim of this thesis was to develop an efficient model and computational framework for predicting the microstructure evolution during two-dimensional grain growth.

In Part I, including Chapter 2 and 3, we developed a computationally efficient mesoscale model to describe grain growth under misorientation-dependent grain boundary energies. This was achieved by generalizing the KWC model for grain boundaries. While the modified form allowed incorporating a crystal symmetry-invariant grain boundary energies in the dual-field KWC model, it resulted in zero mobility for the grain boundaries and grain boundaries cease to move. To address this flaw, we designed a new computational algorithm that evolves grain boundaries by their curvature. The algorithm, which utilizes a primal-dual and the fast marching methods, has a $\mathcal{O}(N \log N)$ computational complexity. The computational speed is also shown to be orders of magnitude faster than the finite-element implementation of the original KWC model. We validated our implementation by predicting the Herring angle relation, and simulated a two-dimensional polycrystal consisting of [110] tilt grain boundaries.

In Part II (Chapter 4), restricting our attention to isotropic grain growth, we turned our focus on developing a lightweight coarse-grained stochastic framework for tracking grain statistics. Under the assumption of spatial homogeneity, we employed areas and topologies (number of sides) as the coarse-grained descriptors of the lightweight model. Starting with an initial joint distribution of areas and the number of sides of grains, the framework seeks to evolve the joint distribution by evolving the areas and topologies of a representative collection of grains, or *rep grains*. The areas of the rep grains were evolved deterministically using the von Neumann–Mullins law. On the other hand, since the topology transformation of a grain is a complex phenomenon, we developed a stochastic *topology transformation model* (TTM). The TTM postulates that the probability that a grain's topology changes can be expressed as a function of the states of the grain and its neighbors. Then, we introduced a data-driven approach to map the probability of the TTM using a fully-connected deep neural network. The parameters of neural network models are trained using data collected from phase field simulations. The evolution of the joint distribution is implemented using a Monte Carlo simulation with transition probabilities obtained from the TTM. We demonstrated that the stochastic framework is able to predict both the transient and asymptotic grain size and topology distributions observed

in phase field simulations. The framework is confirmed to be robust in that the asymptotic distributions are not sensitive to the choice of the initial distribution. Finally, key ideas to extend the machine-learning-informed paradigm were noted.

Appendix A

Results on the 1D KWC model

In this section, we collect results on the one-dimensional KWC model which describes an infinite bicrystal with a grain boundary at the origin. In particular, we present the derivation of the steady-state analytical solution under Dirichlet boundary conditions, and the resulting grain boundary energy as a function of misorientation.

Consider the following KWC energy functional without the $|\nabla\theta|^2$ regularizing term

$$\mathcal{W}[\eta, \theta] = \int_{-\infty}^{\infty} \left[\frac{\epsilon}{2} |\nabla\eta|^2 + \frac{(1-\eta)^2}{2\epsilon} + g(\eta)|\nabla\theta| \right] dV. \tag{A.1}$$

The Euler–Lagrange equation associated with the above functional is

$$\epsilon \triangle \eta - \frac{\eta - 1}{\epsilon} - g_{,\eta} |\nabla\theta| = 0, \tag{A.2}$$

where $g_{,\eta}$ is used to denote $\partial g / \partial \eta$. In what follows, we derive a steady-state solution of (A.2) under Dirichlet boundary conditions

$$\eta(\pm\infty) = 1, \quad \theta(\infty) = -\theta(-\infty) = \theta/2. \tag{A.3}$$

We begin with the ansatz that $\theta(x)$ is a step function satisfying (A.3) with a discontinuity at the origin. Multiplying (A.2) by η', and integrating with respect to x in a region away from the origin, we obtain

$$\frac{\epsilon}{2}\eta_{,x}^2 - \frac{(1-\eta)^2}{2\epsilon} = 0, \implies \eta_{,x} = \pm\frac{(1-\eta)}{\epsilon}, \tag{A.4}$$

On the other hand, multiplying (A.2) with η', and integrating over an arbitrarily small neighborhood of 0 results in the jump condition

$$\epsilon [\![\eta_{,x}]\!] = g_{,\eta}(\bar{\eta}) [\![\theta]\!], \tag{A.5}$$

where $\bar{\eta} := \eta(0)$ is the value of η at the grain boundary. From (A.4) and (A.5), it follows that

$$\epsilon \eta_{,x} = \begin{cases} 1 - \eta & \text{if } x > 0, \\ -(1-\eta) & \text{otherwise,} \end{cases} \tag{A.6}$$

and

$$g_{,\eta}(\bar{\eta}) [\![\theta]\!] = 2(1 - \eta), \tag{A.7}$$

which relates $\bar{\eta}$ to $[\![\theta]\!]$. The analytical solution for η can be obtained by integrating (A.4). With our choice of $g = -\ln(1 - \eta)$, the result can be explicitly written as a function of misorientation $[\![\theta]\!]$:

$$\int_{\bar{\eta}}^{\eta} \frac{\epsilon}{1 - \eta} d\eta = x, \implies \eta(x) = 1 - \sqrt{\frac{[\![\theta]\!]}{2}} \exp\left(-\frac{|x|}{\epsilon}\right). \tag{A.8}$$

The grain boundary energy γ as a function of misorientation is calculated by evaluating $\mathcal{W}[\eta, \theta]$ using the steady state solution for η derived above. From (A.4), we have

$$\begin{aligned}
\gamma([\![\theta]\!]) = \mathcal{W}[\eta, \theta] &= \int_{-\infty}^{\infty} \left[\frac{\epsilon}{2}\eta_{,x}^2 + \frac{(1 - \eta)^2}{2\epsilon}\right] dx + g(\bar{\eta})[\![\theta]\!] \\
&= 2\int_{0}^{\infty} \frac{(1 - \eta)^2}{\epsilon} dx + g(\bar{\eta})[\![\theta]\!] \\
&= 2\int_{\bar{\eta}}^{1} (1 - \eta) d\eta + g(\bar{\eta})[\![\theta]\!] = (1 - \bar{\eta})^2 + g(\bar{\eta})[\![\theta]\!].
\end{aligned} \tag{A.9}$$

Note that the grain boundary energy γ and $\bar{\eta}$ are independent of ϵ, which reinforces that the model converges to its sharp interface as $\epsilon \to 0$ while the energy remains unchanged. Again specializing the analytical expression γ with the choice of the logarithmic g, we obtain

$$\begin{aligned}
\gamma([\![\theta]\!]) &= (1 - \bar{\eta})^2 - [\![\theta]\!]\ln(1 - \bar{\eta}) \\
&= \frac{[\![\theta]\!]}{2} - [\![\theta]\!]\ln\left(\sqrt{\frac{[\![\theta]\!]}{2}}\right).
\end{aligned} \tag{A.10}$$

Appendix B

The covariance model of grain boundary energy

The covariance model for grain boundary energy, developed by Runnels *et al.* [26, 27], estimates grain boundary energy using the covariance of atomic densities of the two lattices adjoining a grain boundary.

In the covariance model, a lattice density measure $\bar{\rho}$ for a given lattice[1] $\mathcal{L}$, defined as an infinite sum of Dirac measures with support at the lattice points points of $\mathcal{L}$:

$$\bar{\rho}(\boldsymbol{x}) = \sum_{\boldsymbol{d} \in \mathcal{L}} \delta(\boldsymbol{x} - \boldsymbol{d}). \tag{B.2}$$

A lattice density field ρ is introduced as the convolution of $\bar{\rho}$ with a thermalization function ξ, i.e.

$$\rho(\boldsymbol{x}) = \overline{\rho}(\boldsymbol{x}) * \xi(\boldsymbol{x}), \tag{B.3}$$

where

$$\xi(\boldsymbol{x}) = \frac{1}{\sigma^3 \pi^{3/2}} e^{-\|\boldsymbol{x}\|^2 / \sigma^2}, \tag{B.4}$$

with σ^2 as the dimensionless temperature. The planar covariance of two thermalized lattices $\mathcal{L}_A$ and $\mathcal{L}_B$ with their respective density fields ρ_A and ρ_B, measured on $\mathbb{R}^2$, is defined as

$$c[\rho_A, \rho_B] = \int_{\boldsymbol{y} \in \mathbb{R}^2} \rho_A(P^T \boldsymbol{y}) \rho_B(P^T \boldsymbol{y}) \lambda(\boldsymbol{y}) \, dA, \tag{B.5}$$

where $\lambda(\boldsymbol{x})$ is an appropriately chosen window function (see (B.8), $P : \mathbb{R}^3 \to \mathbb{R}^2$ is the projection

$$P = \begin{pmatrix} 1 & 0 & 0 \\ 0 & 1 & 0 \end{pmatrix} \tag{B.6}$$

---

[1]A lattice $\mathcal{L}$ is defined using three lattice vectors $\boldsymbol{l}_1$, $\boldsymbol{l}_2$, and $\boldsymbol{l}_3$ as
$$\mathcal{L} = \{n_1 \boldsymbol{l}_1 + n_2 \boldsymbol{l}_2 + n_3 \boldsymbol{l}_3 \, n_i \in \mathbb{Z}\}. \tag{B.1}$$
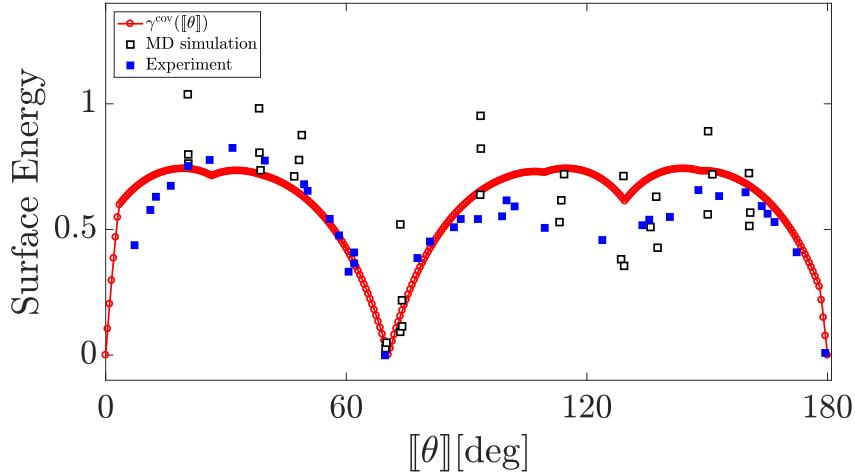
Figure B.1: A plot of the normalized grain boundary energy versus the misorientation angle predicted by the covariance model for a [110] symmetric-tilt grain boundary in fcc copper, computed using the relaxation algorithm of [26, 27]. For comparison, grain boundary energies obtained from experiment [156], and MD simulations [28] are shown in blue and square points respectively.

on to the plane $\mathbb{R}^2$. Expressing the functions ρ_A and ρ_B in Fourier series, the integral in (B.5) simplifies as

$$c[\rho_A, \rho_B] = \frac{1}{\hat{\lambda}(\mathbf{0})} \sum_{\mathbf{k}_A \in \mathcal{L}'_A} \sum_{\mathbf{k}_B \in \mathcal{L}'_B} \widehat{\rho}(\mathbf{k}_A) \widehat{\rho}^*(\mathbf{k}_B) \hat{\lambda} \left(P(\mathbf{k}_B - \mathbf{k}_A) \right), \tag{B.7}$$

where $\mathbf{k}_A$ and $\mathbf{k}_B$ are lattice vectors of the dual lattices $\mathcal{L}'_A$ and $\mathcal{L}'_B$, and the window function is defined in terms of its Fourier transform as

$$\hat{\lambda}(\mathbf{k}) = e^{-\|\mathbf{k}\|/\omega}, \tag{B.8}$$

with an adjustable parameter ω. The grain boundary energy in the covariance model is defined as

$$\gamma^{\text{cov}} = E_0 \left(1 - \frac{c[\rho^{\mathcal{A}}, \rho^{\mathcal{B}}]}{c_{\text{gs}}} \right), \tag{B.9}$$

where c_{gs} is the ground state covariance defined as the supremum, over all planes, of $c[\rho_A, \rho_A]$. For example, in fcc, c_{gs} corresponds to covariance measured with respect to the [111] plane. Finally, we note that the covariance model has three adjustable parameters $\{E_0, \sigma, \omega\}$ that can be used to fit γ^{cov} to data from experiments or molecular dynamics simulations. It is known that while (B.9) is a good indicator of grain boundary energy, it over-predicts the energy for low angle grain boundaries as the above model does not account for facet formation. [26, 27] have shown that a further relaxation of the grain boundary energy, which signifies the formation of facets, yields necessary corrections to the energy predicted by the model.

Appendix C

The primal-dual method

Primal-dual methods is a class of first-order algorithms[1] that have a long history in the context of optimization problems [157–159]. As the name suggests, primal-dual methods proceed by concurrently solving a primal problem and a dual problem. The main benefit of primal-dual splitting is that it replaces an original hard problem with a set of two easy sub-problems (primal- and dual-). Because of this advantage, the method has been widely used in diverse fields including compressed sensing, image processing, signal processing, and machine learning [160–162].

The motivation to use a primal-dual algorithm to solve the minimization problem in (3.1) for η arises due to the presence of a highly nonlinear term $g(\eta)\mathcal{J}(\llbracket\theta\rrbracket)$ along with $|\nabla\eta|^2$. Therefore, we adopt a primal-dual method by introducing an auxiliary dual variable which enables us to cast (3.1) as an equivalent optimization problem. The choice of the dual variable is based on the observation that

$$\frac{\epsilon}{2}\|\nabla\eta\|_{L^2(\Omega)}^2 = \epsilon\|\nabla\eta\|_{L^2(\Omega)}^2 - \frac{\epsilon}{2}\|\nabla\eta\|_{L^2(\Omega)}^2$$
$$= -\epsilon\int_\Omega \eta\triangle\eta\,dV - \int_\Omega \frac{\epsilon}{2}\nabla\eta\cdot\nabla\eta\,dV, \tag{C.1}$$

where we have used the divergence theorem, and the Neumann boundary condition $\nabla\eta\cdot\boldsymbol{n} = \boldsymbol{0}$. Introducing an auxiliary variable ψ, and identifying it with $-\epsilon\triangle\eta$, we have

$$\frac{\epsilon}{2}\|\nabla\eta\|^2 = \sup_{\psi\in(\dot{H}^1(\Omega))^*}\left[\int_\Omega \eta(x)\psi(x)\,dV - \frac{1}{2\epsilon}\|\Delta^{-1}\nabla\psi\|_{L^2(\Omega)}^2\right]$$
$$= \sup_{\psi\in(\dot{H}^1(\Omega))^*}\left[\int_\Omega \eta(x)\psi(x)\,dV - \frac{1}{2\epsilon}\|\psi\|_{(\dot{H}^1(\Omega))^*}^2\right], \tag{C.2}$$

where $\dot{H}^1(\Omega)$ denotes the set of all functions in $H^1(\Omega)$ with zero average, and $(\dot{H}^1(\Omega))^*$ is its dual. Substituting (C.2) into the KWC functional $\mathcal{W}^\mathrm{G}$, the minimization problem in (3.1) transforms to the following saddle point problem:

$$\inf_{\eta\in L^2(\Omega)}\sup_{\psi\in(\dot{H}^1(\Omega))^*}\Phi[\eta,\psi], \tag{C.3}$$

where

$$\Phi[\eta,\psi] = -\frac{1}{2\epsilon}\|\psi\|_{(\dot{H}^1(\Omega))^*}^2 + \int_\Omega (\eta\psi + f(\eta))\,dV + \int_\mathcal{S} g(\eta)\mathcal{J}(\llbracket\theta\rrbracket)\,dS. \tag{C.4}$$

---

[1]An algorithm that only requires the calculation of the gradient of a functional.

The problems of minimizing Φ with respect to η, and maximizing it with respect to ψ are referred to as η and ψ sub-problems respectively. The advantage of using a primal-dual algorithm is evident from the observation that Ψ *does not* depend on the gradients of η, which renders the η sub-problem local, and the nonlinearity in $g(\eta)$ is no longer a concern. The existence and uniqueness of solutions to the sub-problems follows from standard convex analysis.

We solve for the saddle point of Φ using the following primal-dual update scheme (Algorithm 2 in [161]):

$$\eta_{n+1} = \underset{\eta \in L^2(\Omega)}{\arg\min} \left[\Phi(\eta, \psi_n) + \frac{1}{2\tau_n} \|\eta - \eta_n\|^2_{L^2(\Omega)} \right], \tag{C.5a}$$

$$\psi_{n+1} = \underset{\psi \in (\dot{H}^1(\Omega))^*}{\arg\max} \left[\Phi(\tilde{\eta}_{n+1}, \psi) - \frac{1}{2\sigma_n} \|\psi - \psi_n\|^2_{L^2(\Omega)} \right], \tag{C.5b}$$

where

$$\tilde{\eta}_{n+1} = (1 + \mu_n)\eta_{n+1} - \mu_n \eta_n$$

with

$$\mu_n = 1/\sqrt{1 + 2\tau_n/\epsilon}, \quad \tau_{n+1} = \mu_n \tau_n, \quad \sigma_{n+1} = \sigma_n/\mu_n.$$

The scalars τ_n and σ_n are the step sizes of the η- and ψ-update respectively. The stability [68, 161] of the update scheme in (C.5) is guaranteed if $\tau_n \sigma_n \leq 1$. We select $\tau_0 = \epsilon, \sigma_0 = 1/\epsilon$. The solution to (C.5) is obtained by solving the following Euler–Lagrange equations corresponding to gradient flows of the two functionals in (C.5) [2]

$$\left(\frac{1}{\epsilon} + \frac{1}{\tau_n}\right)\eta^2(x) + \left(\psi_n(x) - \frac{2}{\epsilon} - (1 + \eta_n)\frac{1}{\tau_n}\right)\eta(x) - \mathcal{J}^\star([\![\theta]\!]) + \frac{1}{\epsilon} - \psi_n + \frac{1}{\tau_n}\eta_n = 0, \tag{C.6}$$

$$(1/\epsilon - \Delta/\sigma_{n+1})\psi_{n+1} = -\Delta(\bar{\eta}_{n+1} + \psi_n/\sigma_{n+1}), \tag{C.7}$$

where the surface measure $\mathcal{J}([\![\theta]\!])\,dS$ has been replaced by a volume measure $\mathcal{J}^\star\,dV = \mathcal{J}([\![\theta]\!])\exp(-x^2/2\epsilon^4)\,dV$ that depends on the distance x from the grain boundary. From (C.6), we note that the primal dual algorithm along with the choice $g(\eta) = -\log(1 - \eta)$ not only renders the η sub-problem local but also analytically solvable.

We solve (C.6) and (C.7) on a uniform grid of size $N = N_x \times N_y$. Since (C.6) is solved analytically at each grid point, its cost remains $\mathcal{O}(N)$. We solve for ψ_{n+1} in (C.7) using the fast Fourier transform (FFT), resulting in an $\mathcal{O}(N \log N)$ complexity for the primal dual algorithm. We use the following stopping criterion for the update scheme in (C.5),

$$\|\eta_{n+1} - \eta_n\|_\infty = \max_{1 \leq j \leq N} |(\eta_{n+1})_j - (\eta_n)_j| \leq \mathsf{e}, \tag{C.8}$$

where e is the tolerance of the iterative scheme. Finally, we note that the use of FFT to solve (C.7) necessitates periodic boundary conditions on η. On the other hand, for Neumann boundary conditions, we use the discrete cosine transform given by

$$\hat{\psi}_{pq} = \lambda_p \lambda_q \sum_{i=0}^{N_x-1} \sum_{j=0}^{N_y-1} \psi\left(\frac{i}{N_x}, \frac{j}{N_y}\right) \cos\left(\frac{\pi(2i+1)p}{2N_x}\right) \cos\left(\frac{\pi(2j+1)q}{2N_y}\right), \quad \begin{array}{l} 0 \leq p \leq N_x - 1 \\ 0 \leq q \leq N_y - 1, \end{array} \tag{C.9}$$

---

[2] In order to obtain (C.7), we note that the constrained gradient in $(\dot{H}^1(\Omega))^*$ of $\int_\Omega \tilde{\eta}_{n+1}\psi\,dV$ with respect to ψ is $-\triangle\tilde{\eta}_{n+1}$.

with

$$\lambda_p = \begin{cases} 1/\sqrt{N_x}, & p = 0, \\ \sqrt{2/N_x}, & 1 \le p \le N_x - 1, \end{cases} \quad \text{and} \quad \lambda_q = \begin{cases} 1/\sqrt{N_y}, & q = 0, \\ \sqrt{2/N_y}, & 1 \le q \le N_y - 1. \end{cases} \tag{C.10}$$

Appendix D

Note on the derivations of thresholding scheme

In this section, we describe the steps to obtain (3.8) from (3.7). We begin by separating the domain of integration in (3.7) as

$$\int_{-\infty}^{l_0} (1 - u(l/\epsilon))^2 \, dl = \int_{l_0}^{0} (1 - u(l/\epsilon))^2 \, dl + \int_{0}^{+\infty} (1 - u(l/\epsilon))^2 \, dl. \tag{D.1}$$

Substituting the solution in (3.6) into (D.1), we have

$$\frac{(u(0) - 1)^2}{\left(\frac{2}{\epsilon} - \kappa\right)} \exp\left[\left(\frac{2}{\epsilon} - \kappa\right) l_0\right] = \frac{(u(0) - 1)^2}{\left(\frac{2}{\epsilon} - \kappa\right)} \left(1 - \exp\left[\left(\frac{2}{\epsilon} - \kappa\right) l_0\right]\right) + \frac{(u(0) - 1)^2}{\left(\frac{2}{\epsilon} + \kappa\right)}. \tag{D.2}$$

Dividing both sides by $(u(0) - 1)^2$ and collecting the l_0 terms, we obtain

$$\frac{2 \exp\left[\left(\frac{2}{\epsilon} - \kappa\right) l_0\right]}{\left(\frac{2}{\epsilon} - \kappa\right)} = \frac{1}{\left(\frac{2}{\epsilon} - \kappa\right)} + \frac{1}{\left(\frac{2}{\epsilon} + \kappa\right)} = \frac{\frac{4}{\epsilon}}{\left(\frac{4}{\epsilon^2} - \kappa^2\right)}. \tag{D.3}$$

Taking a logarithm, we have

$$\left(\frac{2}{\epsilon} - \kappa\right) l_0 = \log\left(\frac{2/\epsilon}{2/\epsilon + \kappa}\right) = \log\left(\frac{1}{1 + (\epsilon\kappa)/2}\right). \tag{D.4}$$

A Taylor expansion of the right-hand-side of (D.4) with respect to $\epsilon\kappa/2$ results in

$$\left(\frac{2}{\epsilon} - \kappa\right) l_0 = -\frac{\epsilon\kappa}{2} + \frac{\epsilon^2\kappa^2}{4} - \frac{\epsilon^3\kappa^3}{8} + O(\epsilon^4\kappa^4). \tag{D.5}$$

Multiplying by ϵ on both sides, we have

$$(2 - \kappa\epsilon) l_0 = -\frac{\epsilon^2\kappa}{2} + \frac{\epsilon^3\kappa^2}{4} + \frac{\epsilon^4\kappa^3}{8} + O(\epsilon^4\kappa^4). \tag{D.6}$$

Finally, using the approximation $2 - \kappa\epsilon \approx 2$, we get (3.8).

As mentioned in Section 3.2, in practice, the infinite bounds of the integral in (D.1) are replaced by finite

bounds of magnitude $l_{\rm b}$. Under this change, (D.6) modifies as

$$\left(\frac{2}{\epsilon} - \kappa\right) l_0 = \log\left(\frac{\frac{2}{\epsilon}}{\frac{2}{\epsilon} + \kappa} + \boxed{\frac{1}{2}\exp\left(-\left(\frac{2}{\epsilon} - \kappa\right) l_b\right) - \frac{\left(\frac{2}{\epsilon} - \kappa\right)}{2\left(\frac{2}{\epsilon} + \kappa\right)}\exp\left(-\left(\frac{2}{\epsilon} + \kappa\right) l_b\right)}\right). \tag{D.7}$$

It can be easily shown that the boxed terms resulting from a finite value of d_b decay exponentially as $\epsilon \to 0$, which leaves (3.8) unchanged.

Appendix E

Fast marching method

The fast marching method (FMM), developed by Ref. [71] is used to evolve a surface in the outward unit normal direction with a speed $V(\boldsymbol{x}) > 0$. The fast marching method reformulates a time-dependent initial value problem describing the evolution of a surface into an equivalent boundary value formulation. In this section, we summarize the FMM algorithm as described in [163]. For illustration, let $\boldsymbol{s}(t)$ describe a surface evolving with speed $\mathcal{V}$ from a given initial surface $\boldsymbol{s}(0) = \Gamma$. Instead of solving a time-dependent problem for $\boldsymbol{s}(t)$, the fast marching method solves for a function $\zeta(\boldsymbol{x})$ which represents the time it takes for the surface to reach $\boldsymbol{x}$. By the definition of ζ, we have

$$\zeta(\boldsymbol{s}(t)) = t, \tag{E.1}$$

with $\zeta = 0$ on Γ. Differentiating (E.1) with respect to t, and noting that $\nabla\zeta$ is normal to the surface, we arrive at the following boundary value problem

$$|\nabla\zeta|V = 1, \quad \zeta = 0 \text{ on } \Gamma, \tag{E.2}$$

commonly referred to as the Eikonal equation.

Next, we describe the algorithm to solve (E.2) on a two-dimensional grid. In order to compute $|\nabla\zeta|$, an operator D_{ij}^{-x}, representing the standard backward finite difference operation on the grid point ij, is defined as

$$D_{ij}^{-x}\zeta = \frac{\zeta_{ij} - \zeta_{(i-1)j}}{\Delta x}. \tag{E.3}$$

Similarly, D^{+x}, D^{-y}, and D^{+y} denote forward in x, backward and forward in y finite difference operators respectively. To guarantee a unique viscosity solution[1] of the evolving surface, one should consider an upwind finite difference scheme to compute the gradient, which is conveniently written as

$$
\begin{aligned}
|\nabla\zeta| &\approx \left[(\max(D_{ij}^{-x}\zeta, 0)^2 + \min(D^{+x}\zeta_{ij}, 0)^2 + (\max(D_{ij}^{-y}\zeta, 0)^2 + \min(D^{+y}\zeta_{ij}, 0)^2 \right]^{1/2} \\
&= \left[(\max(D_{ij}^{-x}\zeta, 0)^2 + \max(-D^{+x}\zeta_{ij}, 0)^2 + (\max(D_{ij}^{-y}\zeta, 0)^2 + \max(-D^{+y}\zeta_{ij}, 0)^2 \right]^{1/2}.
\end{aligned}
\tag{E.4}
$$

Using (E.4), we rewrite (E.2) in an algebraic form

$$\left[(\max(D_{ij}^{-x}\zeta, D^{+x}\zeta_{ij}, 0)^2 + (\max(D_{ij}^{-y}\zeta, -D^{+y}\zeta_{ij}, 0)^2 \right]^{1/2} = \frac{1}{V(x,y)}. \tag{E.5}$$

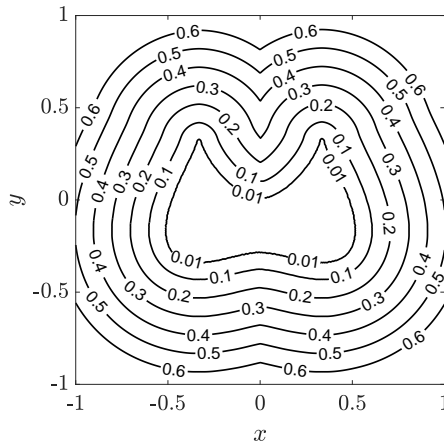[1]See Ref.[163] on the reason behind seeking a viscosity solution.

Figure E.1: The level sets of the solution to the Eikonal equation (E.2), computed using the fast marching method, describe a surface evolving with outward normal velocity $V(x, y) = 1$.

Note that if the neighboring values of ζ_{ij} are known, then (E.5) is a quadratic equation for ζ_{ij} that can be solved analytically.

The fast marching method begins with the following initialization step

1. Assign $\zeta(x) = 0$ for grid points in the area enclosed by the initial surface, and tag them as *accepted*.

2. Assign $\zeta(x) = +\infty$ for the remaining grid points, and tag them as *far*.

3. Among the *accepted* points, identify the points that are in the neighborhood of points tagged as *far*, and tag them as *considered*.

The key step in the fast marching method is to update ζ with a trial value using (E.5) for grid points tagged as *considered* , but only accept the update with the smallest value. In order to identify the smallest value efficiently, the grid points tagged as *considered* are stored in a min-heap[2] structure [164] borrowed from discrete network algorithms. The fast marching method then proceeds as follows.

1. Construct a min-heap structure for the *considered* points.

2. Access the root (minimum value) of the heap.

3. Find a trial solution $\tilde{\zeta}$ on the neighbors of the root using (E.5). If the trial solution is smaller than the present values, then update $\zeta(x) = \tilde{\zeta}$.

4. If a point, previously tagged as *far*, is updated using a trial value, relabel it as *considered*, and add it to the heap structure.

5. Tag the root of the heap as *accepted*, and delete it from the heap.

6. Repeat steps 2 to 5, until every grid point is tagged as *accepted*.

---

[2]A min-heap structure is a complete binary tree with a property that the value at any given node is less than or equal to the values at its children.

Fig. E.1 demonstrates the fast marching method used to track an initial surface

$$(9x^2 - 1)^2 - (3y + 1)(1 - 3y)^3 = 0, \tag{E.6}$$

growing with a uniform outward normal velocity $V(x) = 1$.

References

[1] E. O. Hall, "The deformation and ageing of mild steel: III discussion of results," *Proceedings of the Physical Society. Section B*, vol. 64, pp. 747–753, 1951. DOI: https://doi.org/10.1088/0370-1301/64/9/303.

[2] N. J. Petch, "The cleavage strength of polycrystals," *Journal of the Iron and Steel Institute*, vol. 173, pp. 25–28, 1953.

[3] D. C. Crawford and G. S. Was, "The role of grain boundary misorientation in intergranular cracking of Ni-16Cr-9Fe in 360 °c argon and high-purity water," *Metallurgical Transactions A*, vol. 23, pp. 1195–1206, 1992.

[4] P. Lin, G. Palumbo, U. Erb, and K. T. Aust, "Influence of grain boundary character distribution on sensitization and intergranular corrosion of alloy 600," *Scripta Metallurgica et Materialia*, vol. 33, pp. 1387–1392, 1995. DOI: https://doi.org/10.1016/0956-716X(95)00420-Z.

[5] E. M. Lehockey, G. Palumbo, P. Lin, and A. M. Brennenstuhl, "On the relationship between grain boundary character distribution and intergranular corrosion," *Scripta Materialia*, vol. 36, pp. 1211–1218, 1997. DOI: https://doi.org/10.1016/S1359-6462(97)00018-3.

[6] E. M. Lehockey and G. Palumbo, "On the creep behaviour of grain boundary engineered nickel 1," *Materials Science and Engineering: A*, vol. 237, pp. 168–172, 1997. DOI: https://doi.org/10.1016/S1359-6462(97)00018-3.

[7] T. Watanabe and S. Tsurekawa, "The control of brittleness and development of desirable mechanical properties in polycrystalline systems by grain boundary engineering," *Acta Materialia*, vol. 47, pp. 4171–4185, 1999. DOI: https://doi.org/10.1016/S1359-6454(99)00275-X.

[8] B. Alexandreanu, B. Capell, and G. S. Was, "Combined effect of special grain boundaries and grain boundary carbides on igscc of Ni–16Cr–9Fe–xC alloys," *Materials Science and Engineering: A*, vol. 300, pp. 94–104, 2001. DOI: https://doi.org/10.1016/S0921-5093(00)01705-6.

[9] M. Shimada, H. Kowaka, Z. J. Wang, Y. S. Sato, and I. Karibe, "Optimization of grain boundary character distribution for intergranular corrosion resistant 304 stainless steel by twin-induced grain boundary engineering," *Acta Materialia*, vol. 50, pp. 2331–2341, 2002. DOI: https://doi.org/10.1016/S1359-6454(02)00064-2.

[10] S. Kobayashi, T. Yoshimura, S. Tsurekawa, T. Watanabe, and J. Cui, "Grain boundary microstructure-controlled superplasticity in Al-Li-Cu-Mg-Zr alloy," *Materials Transactions*, vol. 44, pp. 1469–1479, 2003. DOI: https://doi.org/10.2320/matertrans.44.1469.

[11] H. Kokawa, "Weld decay-resistant austenitic stainless steel by grain boundary engineering," *Journal of Materials Science*, vol. 40, pp. 927–932, 2005. DOI: https://doi.org/10.1007/s10853-005-6511-6.

[12] S. Terashima *et al.*, "Improvement of thermal fatigue properties of Sn-Ag-Cu lead-free solder interconnects on Casio's wafer-level packages based on morphology and grain boundary character," *Journal of Electronic Materials*, vol. 38, pp. 33–38, 2009. DOI: https://doi.org/10.1016/j.jcp.2009.09.041.

[13] T. Watanabe, "Grain boundary engineering: Historical perspective and future prospects," *Journal of Material Science*, vol. 46, pp. 4095–4115, 2011. DOI: 10.1007/s10853-011-5393-z.

[14] S. R. Kalidindi, *Hierarchical materials informatics: novel analytics for materials data.* Elsevier, 2015.

[15] S. Esedoḡlu and F. Otto, "Threshold dynamics for networks with arbitrary surface tensions," *Communications on Pure and Applied Mathematics*, vol. 68, pp. 808–864, 2015.

[16] W. W. Mullins, "Two-dimensional motion of idealized grain boundaries," *Journal of Applied Physics*, vol. 27, pp. 900–904, 1956. DOI: 10.1063/1.1722511.

[17] S. L. Thomas, K. Chen, J. Han, P. K. Purohit, and D. J. Srolovitz, "Reconciling grain growth and shear-coupled grain boundary migration," *Nature Communications*, vol. 8, p. 1764, 2017. DOI: https://doi.org/10.1038/s41467-017-01889-3.

[18] J. W. Cahn, Y. Mishin, and A. Suzuki, "Coupling grain boundary motion to shear deformation," *Acta Materialia*, vol. 54, pp. 4953–4975, 2006. DOI: https://doi.org/10.1016/j.actamat.2006.08.004.

[19] R. Kobayashi, J. A. Warren, and W. C. Carter, "Vector-valued phase field model for crystallization and grain boundary formation," *Physica D: Nonlinear Phenomena*, vol. 119, pp. 415–423, 1998. DOI: 10.1016/S0167-2789(98)00026-8.

[20] R. Kobayashi, J. A. Warren, and W. C. Carter, "A continuum model of grain boundaries," *Physica D: Nonlinear Phenomena*, vol. 140, pp. 141–150, 2000. DOI: 10.1016/S0167-2789(00)00023-3.

[21] J. A. Warren, R. Kobayashi, A. E. Lobkovsky, and W. C. Carter, "Extending phase field models of solidification to polycrystalline materials," *Acta Materialla*, vol. 51, pp. 6035–6058, 2003. DOI: 10.1016/S1359-6454(03)00388-4.

[22] J. Kim, M. Jacobs, S. Osher, and N. C. Admal, "A crystal symmetry-invariant Kobayashi–Warren–Carter grain boundary model and its implementation using a thresholding algorithm," *Computational Materials Science*, vol. 199, p. 110 575, 2021. DOI: https://doi.org/10.1016/j.commatsci.2021.110575.

[23] J. Kim and N. C. Admal, "A stochastic framework for evolving grain statistics using a neural network model for grain topology transformations," *Computational Materials Science*, vol. 199, p. 111 812, 2023. DOI: https://doi.org/10.1016/j.commatsci.2022.111812.

[24] E. A. Holm, D. L. Olmsted, and S. M. Foiles, "Comparing grain boundary energies in face-centered cubic metals: Al, Au, Cu and Ni," *Scripta Materialia*, vol. 63, pp. 905–908, 2010. DOI: 10.1016/j.scriptamat.2010.06.040.

[25] V. V. Bulatov, B. W. Reed, and M. Kumar, "Grain boundary energy function for fcc metals," *Acta Materialla*, vol. 65, pp. 161–175, 2014. DOI: 10.1016/j.actamat.2013.10.057.

[26] B. Runnels, I. J. Beyerlein, S. Conti, and M. Ortiz, "An analytical model of interfacial energy based on a lattice-matching interatomic energy," *Journal of Mechanics and Physics of Solids*, vol. 89, pp. 174–193, 2016. DOI: 10.1016/j.jmps.2016.01.008.

[27] B. Runnels, I. J. Beyerlein, S. Conti, and M. Ortiz, "A relaxation method for the energy and morphology of grain boundaries and interfaces," *Journal of Mechanics and Physics of Solids*, vol. 94, pp. 388–408, 2016. DOI: `10.1016/j.jmps.2015.11.007`.

[28] D. Wolf, "Structure-energy correlation for grain boundaries in fcc metals—III. Symmetrical tilt boundaries," *Acta Metallugica et Materialia*, vol. 38, pp. 781–790, 1990. DOI: `10.1016/0956-7151(90) 90030-K`.

[29] J. K. Mason and S. Patala, "Basis functions on the grain boundary space: Theory," *arXiv preprint arXiv:1909.11838*, 2019.

[30] V. V. Bulatov, B. W. Reed, and M. Kumar, "Anisotropy of interfacial energy in five dimensions," *arXiv: Material Science*, 2013. DOI: `https://arxiv.org/abs/1305.1282`.

[31] D. L. Olmsted, S. M. Foiles, and E. A. Holm, "Survey of computed grain boundary properties in face-centered cubic metals: I. grain boundary energy," *Acta Materialla*, vol. 57, no. 13, pp. 3694–3703, 2009. DOI: `10.1016/j.actamat.2009.04.007`.

[32] H.-K. Kim, S. G. Kim, W. Dong, I. Steinbach, and B.-J. Lee, "Phase-field modeling for 3D grain growth based on a grain boundary energy database," *Modelling and Simulation in Materials Science and Engineering*, vol. 22, no. 3, p. 034 004, 2014. DOI: `https://doi.org/10.1088/0965-0393/22/3/ 034004`.

[33] K. Barmak *et al.*, "Grain growth and the puzzle of its stagnation in thin films: The curious tale of a tail and an ear," *Progress in Materials Science*, pp. 987–1055, 2013. DOI: `https://doi.org/10.1016/ j.pmatsci.2013.03.004`.

[34] M. P. Anderson, D. J. Srolovitz, G. S. Grest, and P. S. Sahni, "Computer simulation of grain growth I," *Acta Metallurgica*, vol. 32, pp. 783–791, 1958. DOI: `10.1016/0001-6160(84)90151-2`.

[35] M. P. Anderson, G. S. Grest, and D. J. Srolovitz, "Computer simulation of grain growth in three dimensions," *Philosophical Magazine B*, vol. 59, pp. 293–329, 1989. DOI: `10.1080/13642818908220181`.

[36] M. I. Mendelev and D. J. Srolovitz, "Co-segregation effects on boundary migration," *Interface Science*, vol. 10, pp. 191–199, 2002. DOI: `10.1023/A:1015880314987`.

[37] M. Upmanyu *et al.*, "Boundary mobility and energy anisotropy effects on microstructural evolution during grain growth," *Interface Science*, vol. 10, pp. 201–216, 2002. DOI: `10.1023/A:1015832431826`.

[38] Z. Yang, S. Sista, J. W. Elmer, and T. DebRoy, "Three dimensional Monte carlo simulation of grain growth during GTA welding of titanium," *Acta Materialla*, vol. 48, pp. 4813–4825, 2000. DOI: `10.1016/S1359-6454(00)00279-2`.

[39] M. Hillert, "On the theory of normal and abnormal grain growh," *Acta Metallurgica*, vol. 13, pp. 227–238, 1965.

[40] S. M. Allen and J. W. Cahn, "A microscopic theory for antiphase boundary motion and its application to antiphase domain coarsening," *Acta Metallurgica*, vol. 27, pp. 1085–1095, 1979. DOI: `10.1016/0001-6160(79)90196-2`.

[41] H. J. Frost, C. V. Thompson, and D. T. Walton, "Simulation of thin film grain structures—I. grain growth stagnation," *Acta Metallugica et Materialia*, vol. 38, pp. 1455–1462, 1990. DOI: `10.1016/0956-7151(90)90114-V`.

[42] H. J. Frost, C. V. Thompson, C. L. Howe, and J. Whang, "A two dimensional computer simulation of capillarity-driven grain growth: Preliminary results," *Scripta Metallurgica*, vol. 22, pp. 65–70, 1988. DOI: 10.1016/S0036-9748(88)80307-7.

[43] D. Kinderlehrer, J. H. Lee, I. Livshits, A. D. Rollett, and S. Ta'asan, "Mesoscale simulation of grain growth," *Materials Science Forum*, vol. 467–470, no. 1057–1062, 2004. DOI: 10.4028/www.scientific.net/msf.467-470.1057.

[44] D. Kinderlehrer, I. Livshits, and S. Ta'asan, "A variational approach to modeling and simulation of grain growth," *SIAM Journal on Scientific Computing*, vol. 28, pp. 1694–1715, 2006. DOI: 10.1137/030601971.

[45] D. Weaire and N. River, "Soap, cells and statistics—random patterns in two dimensions," *Contemporary Physics*, vol. 25, pp. 55–59, 1984. DOI: https://doi.org/10.1080/00107518408210979.

[46] L. Maire *et al.*, "Modeling of dynamic and post-dynamic recrystallization by coupling a full field approach to phenomenological laws," *Materials & Design*, vol. 133, pp. 498–519, 2017, ISSN: 0264-1275. DOI: https://doi.org/10.1016/j.matdes.2017.08.015.

[47] J. Fausty, N. Bozzolo, D. P. Munoz, and M. Bernacki, "A novel level-set finite element formulation for grain growth with heterogeneous grain boundary energies," *Materials & Design*, vol. 160, pp. 578–590, 2018. DOI: https://doi.org/10.1016/j.matdes.2018.09.050.

[48] B. Merriman, J. K. Bence, and S. J. Osher, "Diffusion generated motion by mean curvature," *Proceedings of the Computational Crystal Growers Workshop*, pp. 72–83, 1992.

[49] M. Elsey, S. Esedoḡlu, and P. Smereka, "Diffusion generated motion for grain growth in two and three dimensions," *Journal of Computational Physics*, vol. 228, pp. 8015–8033, 2009. DOI: 10.1016/j.jcp.2009.07.020.

[50] M. Elsey, S. Esedoḡlu, and P. Smereka, "Large scale simulations and parameter study for a simple recrystallization model," *Philosophical Magazine*, vol. 91, pp. 1607–1642, 2011. DOI: 10.1080/14786435.2010.546377.

[51] A. Basak and A. Gupta, "A two-dimensional study of coupled grain boundary motion using the level set method," *Modelling and Simulation in Materials Science and Engineering*, vol. 22, 2014. DOI: 10.1088/0965-0393/22/5/055022.

[52] H. Hallberg and V. V. Bulatov, "Modeling of grain growth under fully anisotropic grain boundary energy," *Modelling and Simulation in Materials Science and Engineering*, vol. 27, p. 045 002, 2019. DOI: 10.1088/1361-651X/ab0c6c.

[53] T. Joshi, R. Arora, A. Basak, and A. Gupta, "Equilibrium shape of misfitting precipitates with anisotropic elasticity and anisotropic interfacial energy," *Modelling and Simulation in Materials Science and Engineering*, vol. 28, 2020. DOI: 10.1088/1361-651X/abae12.

[54] A. M. Jokisaari, P. W. Voorhees, J. E. Guyer, J. Warren, and O. G. Heinonen, "Benchmark problems for numerical implementations of phase field models," *Computational Materials Science*, vol. 126, pp. 139–151, 2017. DOI: 10.1016/j.commatsci.2016.09.022.

[55] L.-Q. Chen, "Phase-field models for microstructure evolution," *Annual Review of Materials Research*, vol. 32, pp. 113–140, 2002. DOI: doi.org/10.1146/annurev.matsci.32.112001.132041.

[56] T. Hirouchi, T. Tsuru, and Y. Shibutani, "Grain growth prediction with inclination dependence of [110] tilt grain boundary using multi-phase-field model with penalty for multiple junctions," *Computational Materials Science*, vol. 53, pp. 474–482, 2012. DOI: https://doi.org/10.1016/j.commatsci.2011.08.030.

[57] I. Steinbach, "Phase-field models in materials science," *Modelling and Simulation in Materials Science and Engineering*, vol. 17, p. 073 001, 2009. DOI: https://doi.org/10.1088/0965-0393/17/7/073001.

[58] J. G. Ribot, V. Agrawal, and B. Runnels, "A new approach for phase field modeling of grain boundaries with strongly nonconvex energy," *Modelling and Simulation in Materials Science and Engineering*, vol. 27, 2019. DOI: https://doi.org/10.1088/1361-651x/ab47a0.

[59] N. Moelans, B. Blanpain, and P. Wollants, "Quantitative phase-field approach for simulating grain growth in anisotropic systems with arbitrary inclination and misorientation dependence," *Physical Review Letters*, vol. 101, p. 025 502, 2008. DOI: 10.1103/PhysRevLett.101.025502.

[60] H.-K. Kim, S. G. Kim, W. Dong, I. Steinbach, and B.-J. Lee, "Phase-field modeling for 3d grain growth based on a grain boundary energy database," *Modelling and Simulation in Materials Science and Engineering*, vol. 22, p. 034 004, 2014. DOI: 10.1088/0965-0393/22/3/034004.

[61] D. Fan, S. P. Chen, L.-Q. Chen, and P. W. Voorhees, "Phase-field simulation of 2-D ostwald ripening in the highvolume fraction regime," *Acta Materialla*, vol. 50, 2002. DOI: 10.1016/S1359-6454(01)00393-7.

[62] C. J. Permann, M. R. Tonks, B. Fromm, and D. R. Gaston, "Order parameter re-mapping algorithm for 3D phase field model of grain growth using fem," *Computational Materials Science*, vol. 115, 2016. DOI: 10.1016/j.commatsci.2015.12.042.

[63] W. T. Read and W. Shockley, "Dislocation models of crystal grain boundaries," *Physical Review*, vol. 78, p. 275, 1950. DOI: 10.1103/PhysRev.78.275.

[64] N. C. Admal, J. Segurado, and J. Marian, "A three-dimensional misorientation axis- and inclination-dependent Kobayashi–Warren–Carter grain boundary model," *Journal of the Mechanics and Physics of Solids*, vol. 128, pp. 32–53, 2019. DOI: 10.1016/j.jmps.2019.03.020.

[65] R. Alicandro, A. Braides, and J. M. Shah, "Free-discontinuity problems via functionals involving the L1-norm of the gradient and their approximations," *Interface and Free Boundaries*, vol. 1, pp. 17–37, 1999. DOI: 10.4171/IFB/2.

[66] A. E. Lobkovsky and J. A. Warren, "Sharp interface limit of a phase-field model of crystal grains," *Physical Review E*, vol. 63, p. 051 605, 2001. DOI: 10.1103/PhysRevE.63.051605.

[67] M. R. Dorr, J.-L. Fattebert, M. E. Wickett, J. F. Belak, and P. E. A. Turchi, "A numerical algorithm for the solution of a phase-field model of polycrystalline materials," *Journal of Computational Physics*, vol. 229, pp. 626–641, 2010. DOI: 10.1016/j.jcp.2009.09.041.

[68] M. Jacobs, F. Leger, W. Li, and S. Osher, "Solving large-scale optimization problems with a convergence rate independent of grid size," *SIAM Journal on Numerical Analysis*, vol. 57, pp. 1100–1123, 2019. DOI: 10.1137/18M118640X.

[69] T. Salvador and S. Esedoḡlu, "The role of surface tension and mobility model in simulations of grain growth," *arXiv:1907.11574*, 2019. DOI: https://doi.org/10.1002/cpa.2152.

[70] G. Martine La Boissonière, R. Choksi, K. Barmak, and S. Esedoḡlu, "Statistics of grain growth: Experiment versus the phase-field-crystal and mullins models," *Materialia*, vol. 6, p. 100 280, 2019. DOI: https://doi.org/10.1016/j.mtla.2019.100280.

[71] J. N. Tsitsiklis, "Efficient algorithms for globally optimal trajectories," *IEEE Transactions on Automatic Control*, vol. 40, no. 9, pp. 1528–1538, 1995. DOI: https://doi.org/10.1109/9.412624.

[72] C. Herring, *Surface Tension as a Motivation for Sintering*. McGraw Hill, 1951, pp. 143–179.

[73] S. Esedoḡlu, S. Ruuth, and R. Tsai, "Diffusion generated motion using signed distance functions," *Journal of Computational Physics*, vol. 229, pp. 1017–1042, 2010. DOI: 10.1016/j.jcp.2009.10.002.

[74] M. S. Alnaes *et al.*, "The FEniCS Project Version 1.5," *Archive of Numerical Software*, vol. 3, 2015. DOI: 10.11588/ans.2015.100.20553.

[75] Y. Saad and M. H. Schultz, "GMRES: A generalized minimal residual algorithm for solving non-symmetric linear systems," *SIAM Journal on Scientific Computing*, vol. 7, pp. 856–869, 1986. DOI: 10.1137/0907058.

[76] R. Li and Y. Saad, "GPU-accelerated preconditioned iterative linear solvers," *The Journal of Supercomputing*, vol. 63, pp. 443–466, 2013. DOI: 10.1007/s11227-012-0825-3.

[77] N. K. Govindaraju, B. . Lloyd, Y. Dotsenko, B. Smith, and J. Manferdelli, "High performance discrete fourier transforms on graphics processors," *Proceedings of the 2008 ACM/IEEE Conference on Supercomputing*, 2008. DOI: 10.1109/SC.2008.5213922.

[78] J. C. Li, "Possibility of subgrain rotation during recrystallization," *Journal of Applied Physics*, vol. 33, no. 10, pp. 2958–2965, 1962. DOI: https://doi.org/10.1063/1.1728543.

[79] N. C. Admal, G. Po, and J. Marian, "A unified framework for polycrystal plasticity with grain boundary evolution," *International Journal of Plasticity*, vol. 106, pp. 1–30, 2018. DOI: https://doi.org/10.1016/j.ijplas.2018.01.014.

[80] S. Thomas, K. Chen, J. Han, P. K. Purohit, and D. J. Srolovitz, "Reconciling grain growth and shear-coupled grain boundary migration," *Nature communications*, vol. 8, pp. 1–12, 2017. DOI: 10.1038/s41467-017-01889-3.

[81] C. Wei, L. Zhang, J. Han, D. J. Srolovitz, and Y. Xiang, "Grain boundary triple junction dynamics: A continuum disconnection model," *SIAM Journal on Applied Mathematics*, vol. 80, pp. 1101–1122, 2020. DOI: 10.1137/19M1277722.

[82] B. Runnels and V. Agrawal, "Phase field disconnections: A continuum method for disconnection-mediated grain boundary motion," *Scripta Materialia*, vol. 186, pp. 6–10, 2020. DOI: https://doi.org/10.1016/j.scriptamat.2020.04.042.

[83] X. Zhang, C. J. Yocom, B. Mao, and Y. Liao, "Microstructure evolution during selective laser melting of metallic materials: A review," *Journal of Laser Applications*, vol. 31, p. 031 201, 2019. DOI: https://doi.org/10.2351/1.5085206.

[84] C. J. Todaro *et al.*, "Grain structure control during metal 3D printing by high-intensity ultrasound," *Nature Communications*, vol. 11, p. 142, 2020. DOI: https://doi.org/10.1038/s41467-019-13874-z.

[85] S. M. Hashemi *et al.*, "Computational modelling of process–structure–property–performance relationships in metal additive manufacturing: A review," *International Materials Reviews*, vol. 67, pp. 1–46, 2022. DOI: https://doi.org/10.1080/09506608.2020.1868889.

[86] A. F. Chadwick and P. W. Voorhees, "The development of grain structure during additive manufacturing," *Acta Materialia*, vol. 211, p. 116 862, 2021. DOI: https://doi.org/10.1016/j.actamat.2021.116862.

[87] W. Yan *et al.*, "An integrated process–structure–property modeling framework for additive manufacturing," *Computer Methods in Applied Mechanics and Engineering*, vol. 339, pp. 184–204, 2018. DOI: https://doi.org/10.1016/j.cma.2018.05.004.

[88] T. H. Fang, W. L. Li, N. R. Tao, and K. Lu, "Revealing extraordinary intrinsic tensile plasticity in gradient nano-grained copper," *Science*, vol. 331, pp. 1587–1590, 2011. DOI: https://doi.org/10.1126/science.1200177.

[89] Y. Lin, J. Pan, H. F. Zhou, H. J. Gao, and Y. Li, "Mechanical properties and optimal grain size distribution profile of gradient grained nickel," *Acta Materialia*, vol. 153, pp. 279–289, 2018. DOI: https://doi.org/10.1016/j.actamat.2018.04.065.

[90] X. Wu, P. Jiang, L. Chen, and Y. T. Zhu, "Extraordinary strain hardening by gradient structure," *Proceedings of the National Academy of Sciences*, vol. 111, pp. 1587–1590, 2014. DOI: https://doi.org/10.1073/pnas.1324069111.

[91] K. Lu, "Making strong nanomaterials ductile with gradients," *Science*, vol. 345, pp. 1455–1456, 2014. DOI: https://doi.org/10.1126/science.1255940.

[92] Y. J. Wei *et al.*, "Evading the strength-ductility trade-off dilemma in steel through gradient hierarchical nanotwins," *Nature Commnications*, vol. 5, p. 3580, 2014. DOI: https://doi.org/10.1038/ncomms4580.

[93] S. Berbenni, V. Favier, and M. Berveiller, "Impact of the grain size distribution on the yield stress of heterogeneous materials," *International Journal of Plasticity*, vol. 23, pp. 114–142, 2007. DOI: https://doi.org/10.1016/j.ijplas.2006.03.004.

[94] J. von Neumann, *Metal Interfaces*, C. Herring, Ed. Cleveland: American Society for Metals, 1952.

[95] B. Korbuly, T. Pusztai, G. I. Tóth, H. Henry, M. Plapp, and L. Gránásy, "Orientation-field models for polycrystalline solidification: Grain coarsening and complex growth forms," *Journal of Crystal Growth*, vol. 457, pp. 32–37, 2017. DOI: https://doi.org/10.1016/j.jcrysgro.2016.06.040.

[96] H. Ravash, L. Vanherpe, J. Vleugels, and N. Moelans, "Three-dimensional phase-field study of grain coarsening and grain shape accommodation in the final stage of liquid-phase sintering," *Journal of the European Ceramic Society*, vol. 37, pp. 2265–2275, 2017. DOI: https://doi.org/10.1016/j.jeurceramsoc.2017.01.001.

[97] K. Barmak *et al.*, "Grain boundary energy and grain growth in Al films: Comparison of experiments and simulations," *Scripta Materialia*, vol. 54, pp. 1059–1063, 2006. DOI: https://doi.org/10.1016/j.scriptamat.2005.11.060.

[98] K. Barmak, W. E. Archibald, A. D. Rollett, S. Ta'asan, and D. Kinderlehrer, "Grain boundary properties and grain growth: Al foils, Al films," *Material Research Symposium Proceedings*, vol. 819, no. 66, 2004.

[99] D. T. Carpenter, J. M. Rickman, and K. Barmak, "A methodology for automated quantitative microstructural analysis of transmission electron micrographs," *Journal of Applied Physics*, vol. 84, no. 5843, 1998.

[100] T. Sun *et al.*, "Surface and grain-boundary scattering in nanometric Cu films," *Physical Review B*, vol. 81, p. 155 454, 2010.

[101] W. Fayad, C. V. Thompson, and H. J. Frost, "Steady-state grain-size distributions resulting from grain growth in two dimensions," *Scripta Materialia*, vol. 40, pp. 1199–1204, 1999. DOI: `https://doi.org/10.1016/S1359-6462(99)00034-2`.

[102] E. A. Lazar, J. K. Mason, R. D. MacPherson, and D. J. Srolovitz, "Distribution of topological types in grain-grwoth microstructures," *Physical Review Letters*, vol. 2020, p. 015 501, 2020. DOI: `10.1103/PhysRevLett.125.015501`.

[103] P. Feltham, "Grain growth in metals," *Acta Metallurgica*, vol. 5, pp. 97–105, 1957. DOI: `https://doi.org/10.1016/0001-6160(57)90136-0`.

[104] S. P. Riege, C. V. Thompson, and H. J. Frost, "Simulation of the influence of particles on grain structure evolution in two-dimensional systems and thin films," *Acta Materialia*, vol. 47, pp. 1879–1887, 1999. DOI: `https://doi.org/10.1016/S1359-6454(99)00039-7`.

[105] C. S. Pande, R. A. Masumura, and S. P. Marsh, "Stochastic analysis of two-dimensional grain growth," *Philosophical Magazine A*, vol. 81, pp. 1229–1239, 2001. DOI: `https://doi.org/10.1080/01418610108214438`.

[106] C. S. Pande, "On a stochastic theory of grain growth," *Acta Metallurgica*, vol. 35, pp. 2671–2687, 1987. DOI: `https://doi.org/10.1016/0001-6160(87)90266-5`.

[107] P. R. Rios and K. Lucke, "Comparison of statistical analytical theories of grain growth," *Scripta Materialia*, vol. 44, pp. 2471–2475, 2001. DOI: `https://doi.org/10.1016/S1359-6462(01)00923-X`.

[108] N. P. Louat, "On the theory of normal grain growth," *Acta Metallurgicagica*, vol. 22, pp. 721–724, 1974. DOI: `https://doi.org/10.1016/0001-6160(74)90081-9`.

[109] P. J. Hurley and F. J. Humphreys, "The application of EBSD to the study of substructural development in a cold rolled single-phase aluminium alloy," *Acta Materialia*, vol. 51, pp. 1087–1102, 2003. DOI: `https://doi.org/10.1016/S1359-6454(02)00513-X`.

[110] F. Bachmann, R. Hielscher, and H. Schaeben, "Grain detection from 2d and 3d EBSD data—specification of the MTEX algorithm," *Ultramicroscopy*, vol. 111, pp. 1720–1733, 2011. DOI: `https://doi.org/10.1016/j.ultramic.2011.08.002`.

[111] R. D. MacPherson and D. J. Srolovitz, "The von Neumann relation generalized to coarsening of three-dimensional microstructures," *Nature*, vol. 446, pp. 1053–1055, 2007. DOI: `https://doi.org/10.1038/nature05745`.

[112] S. Hilgenfeldt, A. M. Kraynik, S. A. Koehler, and H. A. Stone, "An accurate von Neumann's law for three-dimensional foams," *Physical Review Letters*, vol. 86, p. 2685, 2001. DOI: `https://doi.org/10.1103/PhysRevLett.86.2685`.

[113] W. W. Mullins, "Estimation of the geometrical rate constant in idealized three dimensional grain growth," *Acta Metallurgica*, vol. 37, pp. 2979–2984, 1989. DOI: `https://doi.org/10.1016/0001-6160(89)90333-7`.

[114] H. V. Atkinson, "Overview no. 65: Theories of normal grain growth in pure single phase systems," *Acta Metallurgica*, vol. 36, pp. 469–491, 1988. DOI: https://doi.org/10.1016/0001-6160(88)90079-X.

[115] E. A. Lazar, "The evolution of cellular structures via curvature flow," Ph.D. dissertation, Princeton University, 2011.

[116] M. Palmer, K. Rajan, M. Glicksman, V. Fradkov, and J. Nordberg, "Two-dimensional grain growth in rapidly solidified succinonitrile films," *Metallurgical and Materials Transactions A*, vol. 26, pp. 1061–1066, 1995. DOI: https://doi.org/10.1007/BF02670601.

[117] V. E. Fradkov and D. Udler, "Two-dimensional normal grain growth: Topological aspects," *Advances in Physics*, vol. 43, pp. 739–789, 1994. DOI: https://doi.org/10.1080/00018739400101559.

[118] M. Blanc and A. Mocellin, "Grain coordination in plane sections of polycrystals," *Acta Metallurgica*, vol. 27, pp. 1231–1237, 1979. DOI: https://doi.org/10.1016/0001-6160(79)90139-1.

[119] E. Carnal and A. Mocellin, "A topological model for plane sections of polycrystals," *Acta Metallurgica*, vol. 29, pp. 135–143, 1981. DOI: https://doi.org/10.1016/0001-6160(81)90094-8.

[120] H. Flyvbjerg, "Model for coarsening froths and foams," *Physical Review E*, vol. 47, p. 4037, 1993. DOI: https://doi.org/10.1080/09500838808214765.

[121] V. E. Fradkov, "A theoretical investigation of two-dimensional grain growth in the 'gas' approximation," *Philosophical Magazine Letters*, vol. 58, pp. 271–275, 1988. DOI: https://doi.org/10.1080/09500838808214764.

[122] V. E. Fradkov, D. G. Udler, and R. E. Kris, "Computer simulation of two-dimensional normal grain growth (the 'gas' approximation)," *Philosophical Magazine Letters*, vol. 58, pp. 277–283, 1988. DOI: https://doi.org/10.1080/09500838808214765.

[123] M. Marder, "Soap-bubble growth," *Physical Review A*, vol. 36, p. 438, 1987. DOI: https://doi.org/10.1103/PhysRevA.36.438.

[124] C. W. J. Beenakker, "Numerical simulation of a coarsening two-dimenional network," *Physical Review A*, vol. 37, p. 1697, 1988. DOI: https://doi.org/10.1103/PhysRevA.37.1697.

[125] M. Raissi and G. E. Karniadakis, "Hidden physics models: Machine learning of nonlinear partial differential equations," *Journal of Computational Physics*, vol. 357, pp. 125–141, 2018.

[126] T. Qu, S. Di, Y. T. Feng, M. Wang, and T. Zhao, "Towards data-driven constitutive modelling for granular materials via micromechanics-informed deep learning," *International Journal of Plasticity*, vol. 144, p. 103 046, 2021. DOI: https://doi.org/10.1063/1.1722511.

[127] Z. Liu and C. T. Wu, "Exploring the 3D architectures of deep material network in data-driven multiscale mechanics," *Journal of the Mechanics and Physics of Solids*, vol. 127, pp. 20–46, 2019. DOI: https://doi.org/10.1063/1.1722511.

[128] U. Ali, W. Muhammad, A. Brahme, O. Skiba, and K. Inal, "Application of artificial neural networks in micromechanics for polycrystalline metals," *International Journal of Plasticity*, vol. 120, pp. 205–219, 2019. DOI: 10.1016/j.ijplas.2019.05.001.

[129] K. Karapiperis, L. Stainer, M. Ortiz, and J. E. Andrade, "Data-driven multiscale modeling in mechanics," *Journal of the Mechanics and Physics of Solids*, vol. 147, p. 104 239, 2021. DOI: https://doi.org/10.1063/1.1722511.

[130] W. Yan *et al.*, "Predicting 2d normal grain growth using a physics-regularized interpretable machine learning model," *arXiv:2203.03735*, 2022. DOI: https://doi.org/10.48550/arXiv.2203.03735.

[131] K. Yang *et al.*, "Self-supervised learning and prediction of microstructure evolution with convolutional recurrent neural networks," *Patterns*, vol. 2, p. 100 243, 2021. DOI: https://doi.org/10.1016/j.patter.2021.100243.

[132] D. M. de O. Zapiain, J. A. Stewart, and R. Dingreville, "Accelerating phase-field-based microstructure evolution predictions via surrogate models trained by machine learning methods," *npj Computational Materials*, vol. 7, p. 3, 2021. DOI: https://doi.org/10.1038/s41524-020-00471-8.

[133] R. Vidal, J. Bruna, R. Giryes, and S. Soatto, "Mathematics of deep learning," *arXiv:1712.04741v1*, 2017.

[134] J. Mairal, J. Ponce, and G. Sapiro, "Online learning for matrix factorization and sparse coding," *Journal of Machine Learning Research*, vol. 11, pp. 19–60, 2010.

[135] D. E. Rumelhart, G. E. Hinton, and R. J. Williams, "Learning representations by back-propagating errors," *Nature*, vol. 323, pp. 533–536, 1986.

[136] S. J. Wright and J. Nocedal, *Numerical Optimization*. Springer New York, 1999, vol. 2.

[137] Y. Xu and W. Yin, "A block coordinate descent method for regularized multiconvex optimization with applications to nonnegative tensor factorization and completion," *SIAM Journal on Imaging Sciences*, vol. 6, pp. 1758–1789, 2013. [Online]. Available: https://epubs.siam.org/doi/10.1137/120887795.

[138] J. L. Leevy, T. M. Khoshgoftaar, R. A. Bauder, and N. Seliya, "A survey on addressing high-class imbalance in big data," *Journal of Big Data*, vol. 5, p. 42, 2018. DOI: https://doi.org/10.1186/s4053701801516.

[139] A. Paszke *et al.*, "Pytorch: An imperative style, high-performance deep learning library," in *Advances in Neural Information Processing Systems 32*, H. Wallach, H. Larochelle, A. Beygelzimer, F. d'Alché-Buc, E. Fox, and R. Garnett, Eds., Curran Associates, Inc., 2019, pp. 8024–8035.

[140] A. F. Agarap, "Deep learning using rectified linear units ReLU," *arXiv preprint*, 2018. DOI: https://doi.org/10.48550/arXiv.1803.08375.

[141] D. P. Kingma and J. L. Ba, "Adam: A method for stochastic optimization," *arXiv:1412.6980*, 2014.

[142] S. J. Reddi, S. Kale, and S. Kumar, "On the convergence of adam and beyond," in *International Conference on Learning Representations*, 2018. [Online]. Available: https://openreview.net/forum?id=ryQu7f-RZ.

[143] D. Kinderlehrer, I. Livshits, and S. Ta'san, "A variational approach to modeling and simulation of grain growth," *Siam Journal of Sicentific Computing*, vol. 28, pp. 1694–1715, 2006. DOI: https://doi.org/10.1137/030601971.

[144] B. Berge, A. J. Simon, and A. Libchaber, "Dynamics of gas bubbles in monolayers," *Physical Review A*, vol. 41, p. 6893, 1990. DOI: https://doi.org/10.1103/PhysRevA.41.6893.

[145] J. A. Glazier, S. P. Gross, and J. Stavans, "Dynamics of two-dimensional soap froths," *Physical Review A*, vol. 36, p. 306, 1987. DOI: https://doi.org/10.1103/PhysRevA.36.306.

[146] A. T. Chieco, J. P. Sethna, and D. J. Durian, "Average evolution and size-topology relations for coarsening 2d dry foams," *Frontiers in Soft Matter*, vol. 2, p. 941 811, 1. DOI: https://doi.org/10.3389/frsfm.2022.941811.

[147] E. A. Lazar, R. D. MachPherson, and D. J. Srolovitz, "A more accurate two-dimensional grain growth algorithm," *Acta Materialia*, vol. 58, pp. 364–372, 2010. DOI: https://doi.org/10.1016/j.actamat.2009.09.008.

[148] H. X. Zhu, S. M. Thorpe, and A. H. Windle, "The geometrical properties of irregular two- dimensional voronoi tessellations," *Philosophical Magazine A*, vol. 81, pp. 2765–2783, 2001. DOI: https://doi.org/10.1080/01418610010032364.

[149] F. T. Lewis, "The correlation between cell division and the shapes and sizes of prismatic cells in the epidermis of cucumis," *The Anatomical Record*, vol. 38, pp. 341–376, 1928. DOI: https://doi.org/10.1002/ar.1090380305.

[150] F. T. Lewis, "A comparison between the mosaic ofpolygons in a film of artificial emulsion and in cucumber epidermis and human amnion," *The Anatomical Record*, vol. 50, pp. 235–265, 1931.

[151] C. S. Smith, "Grains, phases and interfaces—an interpretation of microstructure," *American Institute of Mining and Metallurgical Engineers*, vol. 175, pp. 15–51, 1948.

[152] C. S. Smith, "Grain shapes and other metallurgical applications of topology," *Metallography, Microstructure, and Analysis*, vol. 4, pp. 543–567, 2015. DOI: https://doi.org/10.1007/s13632-015-0241-1.

[153] D. Kinderlehrer, "Added dimensions to grain growth," *Nature*, vol. 446, pp. 995–996, 2001. DOI: https://doi.org/10.1080/01418610010032364.

[154] M. A. Alias and P. R. Buenzli, "Modeling the effect of curvature on the collective behavior of cells growing new tissue," *Biophysical Journal*, vol. 112, pp. 193–204, 2017. DOI: https://doi.org/10.1016/j.bpj.2016.11.3203.

[155] R. Malladi and J. A. Sethian, "Image processing: Flows under min/max curvature and mean curvature," *Graphical Models and Image Processing*, vol. 58, pp. 127–141, 1996. DOI: https://doi.org/10.1006/gmip.1996.0011.

[156] H. Miura, M. Kato, and T. Mori, "Temperature dependence of the energy of Cu [110] symmetrical tilt grain boundaries," *Journal of Material Science Letters*, vol. 13, pp. 46–48, 1994. DOI: 10.1007/BF02352916.

[157] M. J. D. Powell, "Algorithms for nonlinear constraints that use lagrangian functions," *Mathematical Programming*, vol. 14, pp. 224–248, 1978. DOI: 10.1007/BF01588967.

[158] H. W. Kuhn, "The hungarian method for the assignment problem," *Naval Research Logistics Quarterly*, vol. 2, pp. 83–97, 1955. DOI: doi.org/10.1002/nav.3800020109.

[159] N. Komodakis and J. Pesquet, "Playing with duality: An overview of recent Primal-dual approaches for solving large-scale optimization problems," *IEEE Signal Processing Magazine*, vol. 32, pp. 31–54, 2015. DOI: 10.1109/MSP.2014.2377273.

[160] D. L. Donoho, "Compressed sensing," *IEEE Transactions on Information Theory*, vol. 52, pp. 1289–1306, 2006. DOI: 10.1109/TIT.2006.871582.

[161] A. Chambolle and T. Pock, "A first-order primal-dual algorithm for convex problems with applications to imaging," *Journal of Mathematical Imaging and Vision*, vol. 40, pp. 120–145, 2011. DOI: 10.1007/s10851-010-0251-1.

[162] S. Shalev-Shwartz and Y. Singer, "A primal-dual perspective of online learning algorithms," *Machine Learning*, vol. 69, pp. 115–142, 2007. DOI: 10.1007/s10994-007-5014-x.

[163] J. Sethian, "A fast marching level set method for monotonically advancing fronts," *Proceedings of the National Academy of Sciences of the United States of America*, vol. 93, pp. 1591–1595, 1996. DOI: 10.1073/pnas.93.4.1591.

[164] R. Sedgewick and K. Wayne, *Algorithms*. Addison-Wesley, 2008.